DYNAMICS AND CONTROLS OF FLUIDIC PRESSURE-FED MECHANISM

(FPFM) OF NANOPOSITIONING SYSTEM

A Thesis

by

HEEBUM CHUN

Submitted to the Office of Graduate and Professional Studies of
Texas A&M University
in partial fulfillment of the requirements for the degree of

MASTER OF SCIENCE

Chair of Committee,	ChaBum Lee
Committee Members,	Li-Jung Tai
	Mathew Kuttolamadom
Head of Department,	Bryan Rasmussen

December 2020

Major Subject: Mechanical Engineering

ABSTRACT

Flexure or compliant mechanisms are employed in many precisions engineered devices due to their compactness, linearity, resolution, etc. Yet, critical issues remain in motion errors, thermal instability, limited bandwidth, and vibration of dynamic systems. Those issues cannot be negligible to maintain high precision and accuracy for precision engineering applications. In this thesis, a novel fluidic pressure-fed mechanism (FPFM) is proposed and investigated. The proposed method is designing internal fluidic channels inside the spring structure of the flexure mechanism using the additive manufacturing (AM) process to overcome addressed challenges. By applying pneumatic/hydraulic pressure and filling media into fluidic channels, dynamic characteristics of each spring structure of the flexure mechanism can be altered or adjusted to correct motion errors, increase operating speed, and suppress vibration. Additionally, FPFM can enhance thermal stability by flowing fluids without affecting the motion quality of the dynamic system. Lastly, the motion of the nanopositioning system driven by FPFM can provide sub-nanometer resolution motion, and this enables the nanopositioning system to have two linear motion in a monolithic structure. The main objective of this thesis is to propose and validate the feasibility of FPFM that can ultimately be used for a monolithic FPFM dual-mode stage for providing high positioning performance without motion errors while reducing vibration and increasing thermal stability and bandwidth.

DEDICATION

This thesis is dedicated to my family, who always support and pray for my success.

And most of all,

to the Almighty God, my source of wisdom, strength, and courage.

Without whom none of my works would be possible.

ACKNOWLEDGEMENTS

CONTRIBUTORS AND FUNDING SOURCES

Contributors

Funding Source

TABLE OF CONTENTS

LIST OF FIGURES

LIST OF TABLES

1. INTRODUCTION

Flexure or compliant mechanisms are utilized in many precisions engineered devices due to their compactness, linearity, resolution, and bandwidth. However, technological gaps for improvements exist, such as motion errors arising from stage-actuator alignment error or manufacturing tolerance, thermal instability, which may cause thermal displacement errors, limited bandwidth, and vibration of dynamic systems. Those issues need to be enhanced and resolved to achieve high precision and accuracy motion quality. Taking advantage of the additive manufacturing (AM) process that enables the realization in the complex shaped design of the structure, the flexure mechanism that has internal fluidic internal channels was additively manufactured to address current limitations and challenges in precision-engineered devices. The FPFM with internal fluidic channels can be operated by applying pneumatic/hydraulic pressure and flowing and filling media such as air, water, or oil, as shown in Figure 1.1.
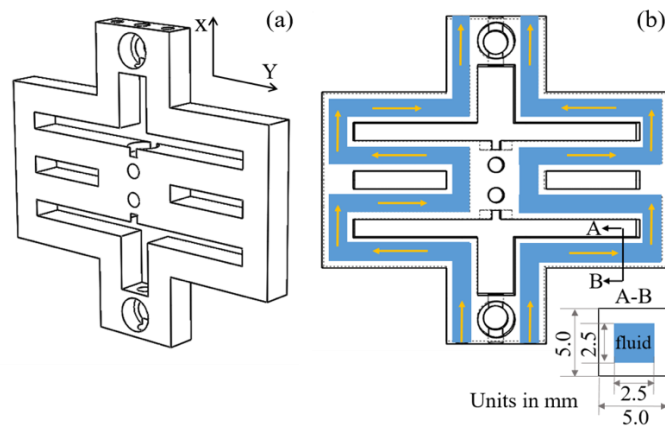
Figure 1.1. Design of flexure based FPFM: (a) 3D CAD model and (b) cross-section view.

The proposed FPFM method has the following capabilities: 1) it can correct angular motion errors occurred from manufacturing tolerance or stage-actuator alignment by applying pressure into internal channels, which change the dynamic characteristics of spring structures of the flexure mechanism, 2) by flowing fluids with a certain pressure level or flowrate, the increased temperature of flexure mechanism which caused by motors, sensors, or environment can be significantly lowered to reduce the thermal displacement errors and to provide thermal stability, 3) FPFM driven by the pneumatic/hydraulic pressure can suppress the vibration beget from resonance frequency and alter the damping parameters to improve the positioning performance and control bandwidth, 4) Finally, the FPFM based nanopositioning system can provide two linear motion in a monolithic structure, which can be utilized for a dual-mode stage with FPFM for a fine motion and piezoelectric (PZT) actuator for a coarse motion. The monolithic FPFM based nanopositioning system has the ability to provide sub-nanometer motion without motion errors induced from the separation of two axes or manufacturing tolerance, together with increasing the system performance and bandwidth with vibration reduction and providing high thermal stability. As a result, the FPFM nanopositioning system fabricated by the AM process can be applied in a high-performance precision-engineered mechanical system.

1.1. Thesis Outline

This thesis divided into multiple chapters, with each detailed preface in sub-section, and the first three chapters include three papers that have already been published

2

in journals. The information of published journals is delineated at the beginning of each chapter.

Chapter two provides an extensive review of the AM process, including the limitation, process, capabilities, and materials of AM technology, and its current utilization and application on the flexure mechanism for the nanopositioning system as well as future applications.

Chapter three details the capability of the designed pressure-fed mechanism on compliant structures to compensate for motion errors by adjusting pressure levels and direction inside internal channels. The result of correcting motion errors driven by FPFM and a preliminary study on the effects of FPFM on the dynamic characteristics will be discussed.

Chapter four focuses on a novel thermal management method on the nanopositioning system by using FPFM to preclude thermal displacement errors. The increased temperature of the dynamic system with heater and motors could be significantly lowered by flowing fluids to achieve high precision motion quality.

Chapter five mainly illustrates the damping characterization of FPFM. The presence of media and pressure can modify the dynamic system identification leading to improved positioning performance, bandwidth, and the stability of the nanopositioning system. The effects of the presence of media and pressure in fluidic channels on the damping of the nanopositioning system were experimentally characterized and discussed.

Chapter six presents the feasibility of a new actuation method driven by FPFM for a fine motion that can provide sub-nanometer resolution. This novel actuation mechanism

will ultimately enable a precision monolithic dual-mode stage application with a PZT actuator as of a coarse motion.

Finally, chapter seven includes a brief summary of the main results and discussion as well as future works.

2. A REVIEW: ADDITIVE MANUFACTURING OF FLEXURE MECHANISM FOR NANOPOSITIONING SYSTEM[*]

2.1. Overview

A comprehensive review relevant to the design and fabrication of nanopositioning stages based on additive manufacturing (AM) technology has been for the first time introduced in the academic society. With the development of AM technology, AM has been applied in many engineering design areas such as aerospace, automotive, consumer electronics, and so on. Due to current limitations of AM tolerance (surface quality, form error), process obscurity (melting pool, layer adhesion) and cost (especially for metals or composites), there are only a small number of AM-applied devices that are currently available either in the market or in many industry sectors above. The flexure mechanisms that are typically employed in nanopositioning applications can provide a sub-nanometer resolution motion; however, their current manufacturing methods (milling, electric discharge machining, water jet machining) not only limit complicated flexure mechanisms in 3D geometries but also prevent designers from challenging novel topology optimizations. AM can overcome those limitations of fabrication and material distribution. Furthermore, it can allow new design approaches to topology optimizations. This review presents current and future AM-based precision motion device applications. Here, both

design and fabrication of flexure mechanisms applied with current AM technology and the potential of further developments were discussed.

2.2. Preface

2.2.1. Additive manufacturing

The development of additive manufacturing (AM) technologies was driven by industry, looking for ways to produce rapid prototypes at low cost without the need for dedicated toolings such as injection molding. AM has offered solutions to shorten the production development cycles and product lead time.

Since the 1980s, a number of rapid prototype (RP) technologies have been developed. This technology builds 3-dimensional objects by adding materials layer by layer from digital information. The transition of these technologies into the manufacturing industry has been termed rapid manufacturing (RM) and the growth of this industry has also been fed by the expiration of some of the early patents held on the fused deposition modeling (FDM) process by Stratasys. Rapid manufacturing led to the expansions of the open-source 3D printers, including the MakerBot, RepRap, and Solidoodle that can now be easily purchased or built for under $1,000. The AM processes will have an enormous impact on the manufacturing and design of components in the 21st century. Especially, the metal AM industry is expected to grow 21% to $1.25 billion according to Wohlers Associates [1]. This review addresses the use of AM to create precision-engineered devices that cannot be manufactured by the traditional manufacturing processes, for example, electric discharge machining (EDM, accuracy ~2.5 µm) [2], waterjet machining

6

(accuracy ~ 25 µm) [3], micro-milling (accuracy ~2 µm) [4] and polymeric/metallic additive manufacturing (accuracy 50~200 µm) [5-10].

In precision devices, the material properties are main factors in the design stage to evaluate static behavior such as deformation, stiffness, and even damping. Especially for precision motion devices where the dynamic performance of the material is of primary importance. Presently, precision-engineered devices applied to precision machine tools, semiconductor equipment, high-resolution microscopes, and coordinate measuring machines are traditionally manufactured by using high-performance materials and tightly controlled processes. Such systems are quite expensive but necessary in technology, increasingly high needs for low-cost, complex-shaped, multi-functional, multi-materials, even internal-structured devices appear while traditional manufacturing technologies have hampered creativity or design.

The emerging of AM is to address those challenges and becoming a game-changer for individuals, academia, and industry. Yet, it has not been considered as a technology that can be used for high-performance end-use devices because of a number of material constraints and resolution issues. Enabling technologies for precision-engineered devices are the sensing and control systems; whether this sensing and control are used in the fabrication of devices such as micrometers and gauge blocks or in the device itself such as precision motion devices, particularly for precision stages. When dynamic and thermal behaviors of additive-manufactured structures are well-understood and characterized, precision motion systems can perform as good as the sensing and control systems in an easy, convenient, and low-cost manner.

2.2.2. Flexure mechanisms

The basic principles of compliant mechanisms have been known for a few decades, and the design and fabrication methods that can be found in the literature have been well documented in textbooks [11-13]. This development has been driven by the increasing need for nanometer motion accuracies and achieving high-precision in industrial sectors such as semiconductors, precision machine tools, and precision manufacturing.

Flexure design is nothing new. A wealth of design information existence enables predicting flexure performance based on the theory of elasticity. A flexure, typically, is any structural element or joint that connects two rigid bodies and it has been outlined as components of elastic compliance. At present, its versatility has been contributing to major breakthroughs in broad research areas and industrial applications together with bio-nanotechnology, nanometrology, semiconductor manufacturing, chemical science and engineering, nano-machining and nanofabrication, material science, high-density data storage systems, and even to micro-electro-mechanical systems (MEMS) [14-16]. Most current research relates to creating high-speed and high-precision positioning platforms for scanning probe microscopy (SPM) and related technologies [17-20].

The flexure mechanisms are able to provide nanometer-scale displacements with a total motion range of around, at least, tens of microns. To achieve such high performance, the design of the positioning mechanisms, the selection of the sensors and actuators, and the implementation of advanced controllers need to be systematically investigated. Researches on flexure mechanisms focus on three key areas: (1) Mechanical design of high-performance flexure mechanisms; (2) Control theory for enhancing the

performance of flexure mechanisms and (3) Sensing technologies for measuring the motion of flexure mechanisms.

As illustrated in Figure 2.1, when the force generated by a piezoelectric (PZT) actuator acts on the mechanism, the flexure joints or flexure structures are deformed to produce the desired displacement. Compared with conventional-scale motion slides, flexure mechanisms provide infinite-motion resolution and preclude friction and backlash found in sliding systems; thus, the positioning resolution is not limited by friction or stiction [12]. The trade-off for the resolution capability of the flexure mechanisms is their small range of displacement since the flexure joints must be operated at the elastic region of the flexure material. If a large motion range is critical, some low friction slides such as air-bearing slides, have to be selected to reduce the error from friction.
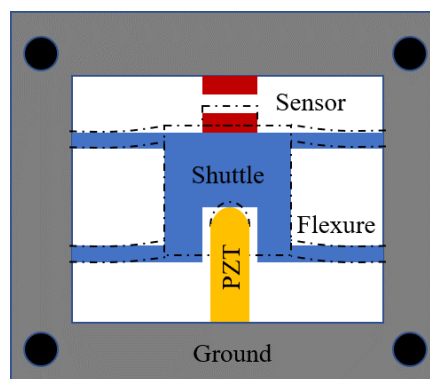
Figure 2.1. Schematic of flexure mechanism: d displacement.

The flexure mechanisms are manufactured in a monolithic configuration without any separation of components. Those systems are usually machined with a mill, EDM, waterjet, plasma-arc, electrochemical, laser, CNC (computer numeric control), and

9

abrasive jet that are precise in motion or minimal off-axis error motion to confirm the high positioning accuracy and resolution [2-10]. These manufacturing technologies take away materials (conductive materials, primarily metal) using planar processing methods (some of the more elaborate machines are capable of additional axes of motion to enable rotations of the planar machining operations). With the recent progress of MEMS technology, several MEMS motion stages are introduced [21, 22]. The total displacement is limited to a few tens of μm even though those are promising for high bandwidth and high resolution. AM, providing three dimensional and freeform manufacturing, promises to be another major contributor to further innovation in flexure mechanisms. All current design approaches focus on the synthesis from individual elements, from which, the structure is then translated into parts for manufacturing and subsequent assembly. The ability to translate a mechanism design directly to a functional mechanism manufactured from a single monolithic material represents the enormous potential for cost-savings and the predictability of subsequent performance.

2.2.3. Additive manufacturing-based flexure mechanism design

Flexure designs based on AM differ from existing flexure designs. First, flexures can be designed using AM process by emphasizing on the functional aspects without considering whether they can be machined. For instance, the existing cooling channel can be obtained by conventional machinability as shown in Figure 2.2 (a). However, if it is manufactured using AM technology, forming the internal channel will not be affected by its machinability. Therefore, it can be designed as Figure 2.2 (b) without considering the

limitation of machinability and by focusing only on improving its cooling performance [23, 24].

(a) conventional cooling channels   (b) conformal cooling channels
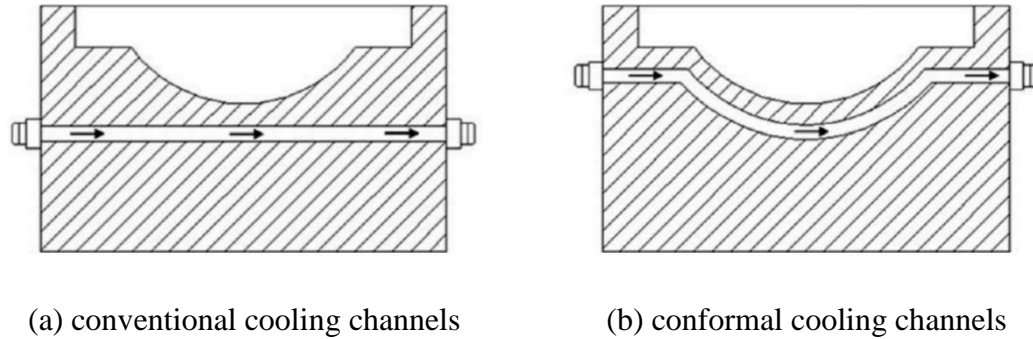
Figure 2.2. Cooling channels: (a) conventional cooling channels and (b) conformal cooling channels. Reprinted from [23, 24].

The flexure mechanisms can be designed by using AM to improve performance aspects rather than to increase possibilities of machining. When designing a conventional flexure mechanism, the machinability must be considered. Additionally, in designing a flexure mechanism, the desired properties include high precision, long feed distance, and high natural frequency. The flexure design can be performed using CAD software; however, the design geometry might not be able to be machined due to the limitation of conventional machining processes. A high-performance flexure mechanism is meaningless unless it is machinable. AM enables the completely new design type of flexure mechanism, which is, otherwise, unachievable through conventional machining. Furthermore, a compact-sized flexure design can be achieved using AM. One of the most

important aspects when creating a nano-precision positioning system using the flexure mechanism is symmetric design. In the ideal design, the flexure can move linearly in the driving direction without parasitic motions. Furthermore, the ideal motion is generally designed symmetrically from one side to another to account for the thermal expansion of materials and machining errors. Therefore, the symmetrical design is structurally stable but the design results in a large and heavy system. Hardware size and weight are issues in precision equipment. In general, sophisticated technology is required to fabricate smaller systems while maintaining the desired performance. Flexure designs based on AM enables a compact system as well as maintaining the symmetry of the system. A typical example of the flexure mechanism designed using the advantages of AM is depicted in Figure 2.3 [25]. While maintaining the symmetrical shape for the XY motion of the platform, the XY amplification mechanism was placed in one part of the outer section. The example flexure design as shown in Figure 2.3 cannot be achieved through conventional machining; however, it can only be realized using AM. Overall, flexure mechanisms are allowed to be compact, symmetric, and complex shaped geometry by using AM technology.
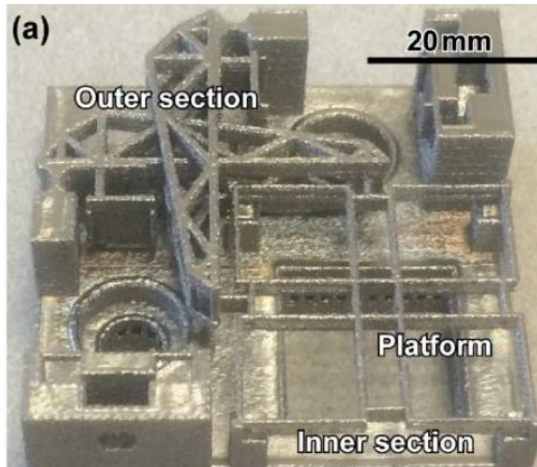
Figure 2.3. AM-printed nanopositioning flexure mechanism. Reprinted from [25].

2.2.4. Patent and journal paper map

Because the research on the nanopositioning systems or flexure mechanisms has been of interest in academia and industry a long time ago, many patents and journals are published. Novel ideas and approaches have been historically introduced in terms of design, control, and fabrication. There exist few records for intellectual property (IP) and journal publications that are based on AM technology. In this review, the IP filing and journal publication database archived since 2010 were collected. The keywords (additive manufacturing, 3D printing, flexure mechanisms, positioning stages, and compliance mechanisms) were used to search the patents registered or filed from the United States (US), Europe (EU), China, Japan, and South Korea in the patent search engines (Google patents and KIPRIS), and all searched patents were manually filtered. There were five patents (US 1, EU 1, China 1, and South Korea 2) searched [26-30]. Four patents were disclosed based on polymeric structures, and one patent from China was based on metal

13

structures. Similarly, publications were searched with the same keywords in Elsevier, Springer, Institute of Physics, Hindawi and Google Scholar. Since 2010, 11 journals (3 metal printing, 8 polymer printing) [8-10, 31-38] and 4 conference papers (2 metal printing) [39-42] have been published. It is expected that the precision positioning stage applications with AM processes will be dramatically increased with the development of AM technology and the popularization of AM machine tools. Thus, the novel design, control and implementation approaches created by AM technology will increase the number of patents and publications in the near future. This review will shed light on a new perspective of AM technology toward precision motion devices.

2.3. AM Design and Manufacturing Technology

2.3.1. Process characterization of AM

To achieve the high-performance flexure mechanisms, the AM process has been reviewed for selecting an appropriate AM technology and a corresponding build layout. As shown in Table 2.1, the AM process has been classified AM technologies into seven categories: (1) Material extrusion; (2) Powder bed fusion; (3) Vat photopolymerization; (4) Material jetting; (5) Binder jetting; (6) Sheet lamination; (7) Directed energy deposition [43].

Among those, the powder bed fusion (PBF) process uses an energy beam to build the 3-dimensional parts layer upon layer by sintering/melting fine powders in the powder bed. The powders in each layer are used together with a laser beam or electron beam which is used at a specific location for each layer specified by the design [44]. The PBF process includes the following commonly used these technologies: Selective laser melting (SLM),

Selective laser sintering (SLS), Direct metal laser sintering (DMLS), Laser metal fusion (LMF), Direct laser melting (DLM), Direct metal printing (DMP), and Electron beam melting (EBM) [45]. The advantages of PBF process are mostly about next. First, there is a wide range of materials that can be processed from polymers to metals. Second, the parts that are fully or even partially sintered/melted can have significant density, strength and stiffness advantages over non-sintered/melted processes as the material properties can be close to that of feedstock. Third, depending on the PBF process and the materials, support structures may not be needed, as the powder bed becomes the support. Fourth, the PBF process that uses laser beam or electron beam results in a high level of accuracy and details [44]. Therefore, the PBF process is most suited to design and fabricate the flexure mechanisms due to these advantages.

Table 2.1. Classification of AM Process. Adapted from [43].

Categories	Technologies	Materials	Energy sources	Strengths / Weaknesses
Material extrusion	Fused deposition modeling (FDM) Contour crafting	Thermoplastics, ceramic slurries, metal pastes	Thermal energy	· Inexpensive extrusion machine · Multi-material printing · Limited part resolution · Poor surface finish
Powder bed fusion	Selective laser sintering (SLS) Direct metal laser sintering (DMLS) Selective Laser Melting (SLM) Electron beam melting (EBM)	Polyamides, polymer Metal powder, ceramic powder	Laser beam Electron beam	· High accuracy and details · Fully dense parts · High specific strength & stiffness · Powder handling & recycling · Support and anchor structure

Table 2.1. Continued.

Categories	Technologies	Materials	Energy sources	Strengths / Weaknesses
Vat photo polymerization	Direct metal laser sintering (DMLS)	Photopolymer, ceramics (alumina, zirconia, PZT)	Ultraviolet laser	· High printing speed · Good part resolution · Overcuring, scanned line shape · High cost for supplies and materials
Material jetting	Selective Laser Melting (SLM)	Photopolymer, wax	Thermal energy /Photocuring	· Multi-material printing · High surface finish · Low-strength material
Binder jetting	Electron beam melting (EBM)	Polymer powder, ceramic powder, metal powder	Thermal energy	· Full-color printing · Require infiltration during post-processing · Wide material selection · High porosities on finished parts
Sheet lamination	Laminated object manufacturing (LOM)	Plastic film, metallic sheet, ceramic tape	Laser beam	· High surface finish · Low material, machine, process cost · Decubing issues
Directed energy deposition	Laser engineered net shaping (LENS) Electronic beam welding (EBW)	Metal powder	Laser beam	· Repair of damaged / worn parts · Functionally graded material printing · Require post-processing machine

2.3.2. Material characterization of AM

Two types of material such as polymer and metal have been used in the PBF process, representatively. Due to the low-cost and flexibility, the polymers have been applied for decades in the AM process. The polymers have the ability to soften and flow when sintered/melted and regain firmness when cooled, making them ideal for the AM process. High-quality polymers such as ABS, PLA, and PC have excellent mechanical

properties [46]. However, in the flexure mechanisms, most of polymer parts manufactured by the PBF process are still used as conceptual prototypes rather than functional parts, since the pure polymer parts manufactured by the PBF process are lack of strength and functionality.

Meanwhile, metals have become a continuous trend in the AM process. Its main advantage lies in continuous expansion in the range of metals that can be produced in the PBF process. Currently, the available metals enable to produce parts of any desired design and mechanical and chemical properties. Therefore, nowadays, metals have been actively applied to the PBF process to achieve high-performance flexure mechanisms [6].

In the PBF process, the feedstock such as a high-quality metal powder is especially important for a successful process. The most established and verified feedstock includes Stainless steel, Aluminium alloys, Cobalt alloys, Nickel alloys, Iron alloys and Titanium alloys. Among those, Stainless steel and Aluminium alloys are used in the flexure mechanisms thanks to their peculiar combination of properties and 10 ~ 30 % cheaper than other materials. Stainless steel exhibits few mechanical properties favored in the PBF process, including hardness, tensile strength, formability, and impact resistance. Especially, 316L Stainless steel is mainly used as feedstock to manufacture the flexure mechanisms due to its advantages in weldability, corrosion resistance and high strength. In the case of aluminium alloys, it demonstrates high strength to weight ratios, good resistance to metal fatigue and corrosions. Additionally, aluminium alloys typically offer better build rates than other metal feedstocks used in PBF process. They possess fine-grained microstructures with grains roughly equal in size and they are typically as strong

as wrought parts. Therefore, excellent fusion characteristics make them well suited for flexure mechanisms. As a result, they are actively applied to the flexure mechanisms [43-47].

2.3.2.1. Mechanical property of AM part

The mechanical properties of part manufactured by AM process are important to obtain desired characteristics. Thus, many researchers have investigated the mechanical properties of part manufactured by the PBF process. Mower *et al.* measured the flexural modulus of melted materials and compared with those of bulk materials that are chemically identical or similar [47]. The results of flexural modulus measurements are listed in Table 2.2. The SLM aluminum proved to be about 10% stiffer than bulk Al 6061 (machined by CNC). The comparison is useful since the only aluminum available at present for commercial SLM or DMLS production is AlSi10Mg. Specimens of this material produced with SLM in the vertical orientation demonstrated slightly higher modulus (73.8 GPa) than those fabricated in the horizontal orientation (71.8 GPa).

Table 2.2. Measured flexural modulus of part manufactured by PBF process. Adapted from [47].

Material	Longitudinal (GPa)	Horizontal (GPa)	Vertical (GPa)
Bulk Al6061	65.5	-	-
AM SLM AlSi10Mg	-	71.8	73.8
Bulk Ti6Al4V	114.0	-	-
AM DMLS Ti6Al4V	-	115.3	116.5

Table 2.2. Continued.

Material	Longitudinal (GPa)	Horizontal (GPa)	Vertical (GPa)
Am DMLS Ti6Al4V (HIP)	-	117.5	119.4
Bulk 316L	191.3	-	-
AM DMLS 316L	-	187.3	189.1
Bulk 17-4PH	193.9	-	-
AM DMLS 17-4PH	-	172.2	192.9

2.3.2.2. Common defect of AM part

Many researchers examined the impact of different types of defects on the mechanical performance of AM parts [48-54]. The existence of defects can be the source to possess poor mechanical properties and accuracy of mechanical motions under certain loading conditions. Variations such as heat source power, layer thickness, feed rate of powder, powder size distribution, scan speed, the spacing of scan lines, surface chemistries in the process of parameters, and the attribute of powder influence the microstructural characteristics present in PBF parts (e.g., grain size, texture, solute distribution) and these may have effects on the quality of deposited materials and the generation of defects [55-58]. Several studies are conducted to understand and quantify the effects of parameters on the final microstructural characteristics, e.g., Rombouts *et al.* [59] and Slotwinski [60-63]. As the combined influence of all related parameters is not fully understood yet, critical experiments and vigorous process models are still in need of developing [58, 59, 64-67].

The common defects are classified into three types: (1) Porosity; (2) Lack of fusion; (3) Crack. The porosity, lack of fusion, and crack are types of common defects found in AM parts as shown in Table 2.3 and these defects are induced to the AM parts during the AM process. Especially, several process parameters and feed material attributes have been associated with these defects of AM parts. The localized heating and rapid cooling along with consuming powdered material as the feed stock create a favorable environment for defect formation by leaving the porosity, lack of fusion regions, or crack [68, 69].

Porosity is formed when high energy source causes the materials to be vaporized locally. In order to prevent the inclusion of porosity, the process condition like high energy density caused by high energy source and low scanning speed should be avoided. Lack of fusion is generated due to the insufficient energy source and it generally contains un-melted metal powders in AM parts. Hence, the process condition should be optimized in order to create perfect AM parts. Crack is being caused by thermal histories such as complex heating and cooling cycles, and this could affect the fatigue crack growth. Therefore, post-processing is required to prevent crack [68-74].

Table 2.3. Common defects in PBF part. Adapted from [68-74].
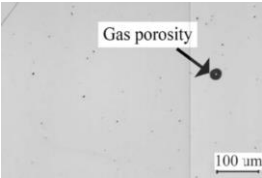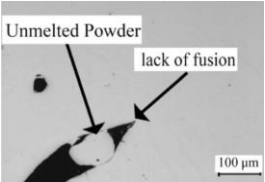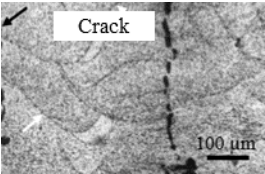
Defect	Description	Effects on part quality	Example
Porosity	Voids either within a layer or between layers caused by lack of fusion or gas entrapment, typically due to improper energy densities	· Decreased mechanical properties · Increased fatigue crack initiation · Increased anisotropic effects	

Table 2.3. Continued.

Defect	Description	Effects on part quality	Example
Lack of fusion	Unfused powder in final part caused by improper energy source densities, primarily very low energy source densities	· Decreased mechanical properties · Increased fatigue crack initiation · Increased anisotropic effects	
Crack	Cracks formed inside final part, typically from residual stress due to complex heating / cooling cycles experienced	· Decreased high and low cycle fatigue performance	

2.3.3. Technological challenges in metrology and inspection of AM part

The flexure mechanism for nanopositioning system has begun to adopt AM technologies. With the maturation of AM technologies, it is essential to characterize the performance of AM machine tools, focusing on in-situ process monitoring, in-process measurement, process feedback, and correction [75-80]. Especially, the PBF process is no longer simply a prototyping technology, and in consequence, metrology is an ever-present area of focus in this field. This transition comes to an array of considerations that must be dealt with the validation of the accuracy, precision, and effectiveness of parts made [79, 80]. Existing examination and metrology techniques are not optimized for PBF process, materials, or parts, although there is a growing need for PBF part inspection and quality control. In-situ non-destructive inspection technique is required to discover the defects that severely affect the performance of nanopositioning stages.

Several non-destructive techniques have been identified for the detection of defects, process monitoring, and analysis of materials in PBF parts and are in varying stages of development. A brief introduction of defect detection techniques under the development for monitoring PBF processes is described in Table 2.4.

Optical inspection such as Visual inspection and Dye inspection are useful tools for non-destructive techniques of AM parts due to its low-cost and ease of implementation [81-85]. Ultrasonic testing has a wide range of applications in materials testing and evaluation [86-91]. These techniques can be extensively applied for inspection of AM parts. Recently, electromagnetic testing can be utilized to detect changes in capacitance due to porosity, lack of fusion, and crack [92-97].

Table 2.4. Classification of metrology techniques for detecting defects of PBF part. Adapted from [81-97].

Categories	Strengths	Weaknesses
Visual inspections	· Rapid	· Mainly superficial defects
	· Minimal evaluations	· Require adequate illumination
	· Easy to automate	· Relative evaluations
Dye inspection	· Detect subsurface defects	· Require preparation
	· Wide range of materials	· Time consuming
	· Low cost	· Limited to small areas
Electromagnetic	· Rapid	· Only magnetic materials
testing	· Subsurface defects	· Single point measure
	· Low cost	· Penetration depth

Table 2.4. Continued.

Categories	Strengths	Weaknesses
Radiographic testing	· Subsurface defects	· Laboratory usage
	· Metallic and non-metallic materials	· Part size
	· Penetration depth	
Laser testing	· Full field image technique	· High stable mounting setup
	· Scanning area	· Expensive
	· Several materials	
Ultrasonic testing	· Penetration depth	· Single point measure
	· Accuracy	· Only simple shape
	· Low cost	
Acoustic emission	· Low cost	· Metallic materials
	· Continuous monitoring	· Inaccurate location of failure
	· Fatigue failure prediction	· Materials damping properties
Vibration analyses	· Rapid	· Dependent of material stiffness
	· Low cost	· Require preparation

2.4. Current Applications

2.4.1. Polymer AM flexure mechanisms

Lee *et al.* [8-10, 14-17] designed and tested a polymeric flexure mechanism for a long-working range and high-resolution. The monolithic double compound notch flexure mechanism (DCNFM) was constructed to demonstrate this concept, and the flexure geometric effects of the AM stage were investigated by estimating the compliance, stress,

and force applied to the flexure. The fundamental limitations of the proposed positioning system such as resolution, bandwidth, and control effectiveness are discussed following.

The DCNFM, well-known as a precision stage, employed in this study is illustrated in Figure 2.4. It has a symmetric design that consists of four compound springs attached to each side of the moving platform and the shuttle. The use of joined four compound springs constrains the stage motion to inhibit deviation from rectilinear motion. The translation of the shuttle is controlled by two identical four-spring mechanisms in the condition of elastic deformation. Another advantage of the implementation of two symmetrical four-spring mechanisms is to permit self-compensate for thermal expansion. Each spring was designed with circular flexure hinges at both ends as shown in Figure 2.4 because these hinges are used in compliant micro-motion stages for high-precision control. As shown in Figure 2.4, Ax and Ay are the lengths of the hinge, T is the thickness of the hinge, B is the width of the hinge, L is the length of the flexure, and H is the height of the flexure. These kinds of flexure hinges are precise in rotation since their center of rotation does not displace as much as other hinges, such as the leaf-type or the corner-fillet. Besides, the circular flexure hinge for the flexure stages can prevent abrupt changes in the cross-sectional flow area whereas generating typically pure rotation. The flexure stage was fabricated by the stereolithography process (Projet®6000HD, 3D Systems Inc.) using a photo-sensitive photopolymer (Visijet® SL Tough, 25µm fabrication resolution). It took only an hour to complete the fabrication of a full monolithic structure with a dimension of $100 \times 110 \times 15$ mm³. As seen in Figure 2.5, the flexure hinge was fabricated: $A_x = 0.6$ mm, $A_y = 0.2$ mm, $T = 0.6$ mm, $H = 1.0$ mm. The surface quality of the AM stage along the

height direction was evaluated by using a high-resolution optical scanning microscope (VHX-2000, Keyence Inc.).
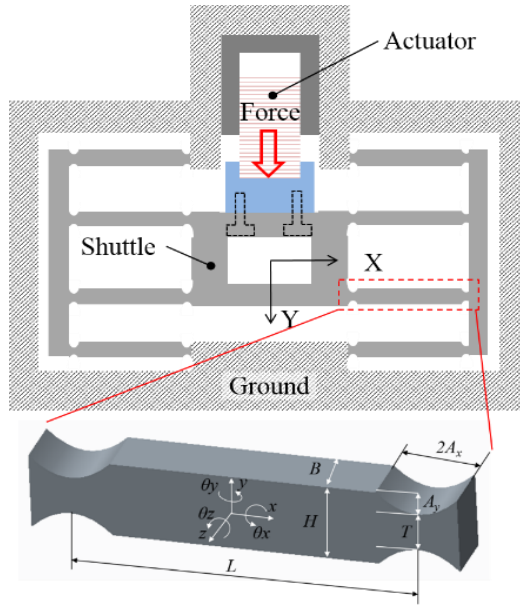
Figure 2.4. Configuration of double compound notch flexure mechanism.

The flexure surface quality introduces an additional stress concentration to the flexure, which considerably affects the fatigue strength due to the possibility of crack nucleation and propagation on the surface [27, 28]. The top surface of the printed flexure was smooth and shiny (Figure 2.5 (a)). The surface profiles along the vertical direction and horizontal direction were measured (Figure 2.5 (b)) and it showed approximately 6 µm and 1 µm surface waviness along with the vertical and horizontal directions, respectively. Compared with typical electrical discharged machining (EDM) tolerance (5~10µm), the AM approach to nanopositioning devices is able to provide high tolerance

design (6 μm), low printing time (1 hour), low cost, and freedom of design. The compliance of the AM stage was measured using a force sensor with a digital micrometer (resolution 1μm) and compared to FEM results. The measurement result of 0.317 mm/N was 23.0% lower than the FEM result of 0.413 mm/N. We conclude that the discrepancy can be arisen from the AM tolerance and fabrication conditions: the layer-to-layer printing thickness, printing speed, printing temperature, and curing temperature and time.
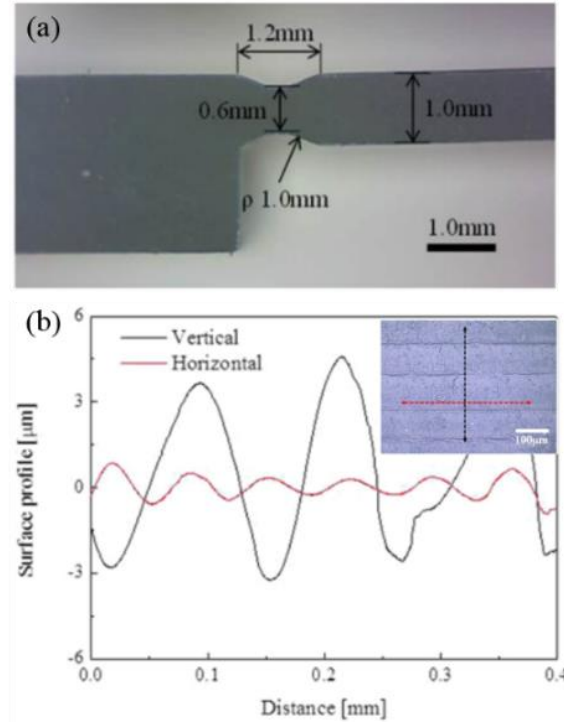
Figure 2.5. Fabrication results: (a) top surface flexure and (b) flexure wall surface image. Reprinted from [10].

Sharkey *et al.* [35] presented a new methodology to overcome several restrictions of 3D printed mechanisms by exploiting the compliance of the plastic to produce a monolithic 3D printed flexure translation stage. This structure is capable of sub-micron-scale motion over a range of $8 \times 8 \times 4$ mm. Parallelogram structures form the basis of the microscope mechanism: the four-bar linkage enables the objective to vertically translate while not changing orientation or lateral position. This is close to the yield strain of both the PLA and ABS plastics which are typically utilized in 3D printing. They implemented a simple optical microscope based around the printed translation stage (Figure 2.6) to quantify their mechanical performance in a realistic situation. This allows us to measure its stability over a range of time scales and to demonstrate the precision which can position a sample relative to the objective lens.
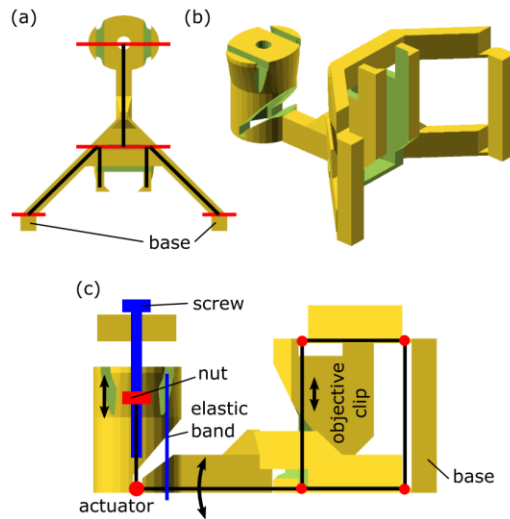
Figure 2.6. Flexure mechanism for vertical motion of the microscope objective, (a) plan view, (b) orthographic projection, and (c) elevation showing the flexure hinge points as circles. Reprinted from [35].

2.4.2. Metal AM flexure mechanisms

Wei *et al.* [32] reported the fabrication and characterization of a flexure parallel mechanism through the laser beam melting (LBM) process to demonstrate the development of the proposed AM technique. The geometrical accuracy of the AM flexure mechanism was investigated by three-dimensional scanning.

Figure 2.7 shows the deviation of geometry between the AM flexure mechanism measured by 3D laser scanning and the designed 3D model. This result of measurement indicates the overall fabrication error (or tolerance) of the LBM process for the flexure mechanism. It was found out that 77% of the geometry deviation was within ±0.093 mm and the deviation along the width (printing direction) was larger than that along with the thickness. The deviation can be mainly caused by the layer-by-layer process of the AM and the thermal stress due to the high cooling rate during the LBM process.
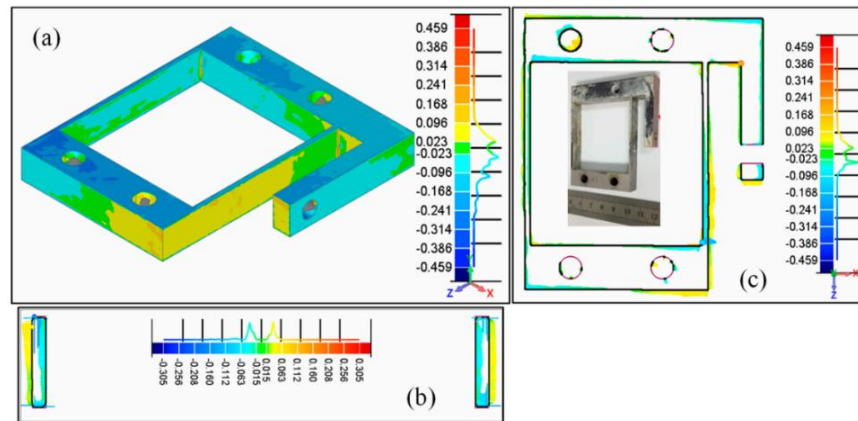
Figure 2.7. Geometrical analysis of the LBM AM flexure mechanism through 3D laser scanning: (a) 3D deviation, (b) cross-section at the middle of the hinge and (c) cross-section at the middle of the hinge along the width direction. Reprinted from [35].

Fowler *et al.* proposed a large-displacement monolithic compliant rotational hinge (Figure 2.8) was fabricated by three materials (polypropylene, titanium, and carbon nanotube), the so-called Flex-16, which attains 90° of rotation from monolithic construction and is aimed for application of compliant satellite deployment hinge [98]. Advances in electron beam melting (EBM) enable AM with a variety of metals, including alloys of Titanium. Two grades of Titanium powder are currently available for the use in EBM machine tools: Ti6Al4V and Ti6Al4V ELI (extra low interstitials).
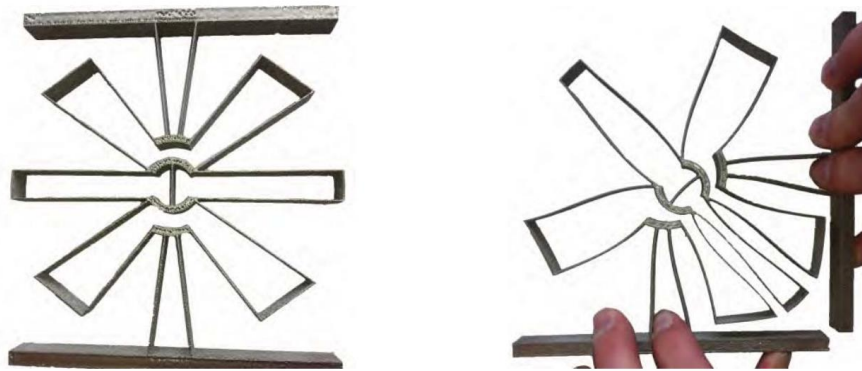
Figure 2.8. A compliant Titanium hinge produced with electron beam melting (EBM). Reprinted from [101].

Pham *et al*. [33] presented the synthesis and evaluation method for a 3-D printed three degree-of-freedom spatial-motion compliant parallel mechanism by EBM technology (Figure 2.9). A 0.5 mm thick linear spring mechanism was fabricated by EBM technology with the identical material and building direction as the compliant mechanism prototype. The stiffness of the printed linear spring mechanism was then evaluated using the experimental setup as shown in Figure 2.9. A micrometer was applied to produce the

input displacement and a six-axis force/torque (F/T) sensor (ATI, MINI-40) was employed to measure the actuating force. A force was applied to the flexures through a rod that was rigidly connected to the free end of the linear spring mechanism. Under the actuating force, the free end of the linear spring mechanism would be displaced along the horizontal direction, which was parallel to the input displacement from the micrometer. To ensure the accuracy of the measured force, a linear guide was used to eliminate the parasitic motion perpendicular to the main motion of the linear spring mechanism due to the elastic deformation of two flexures.
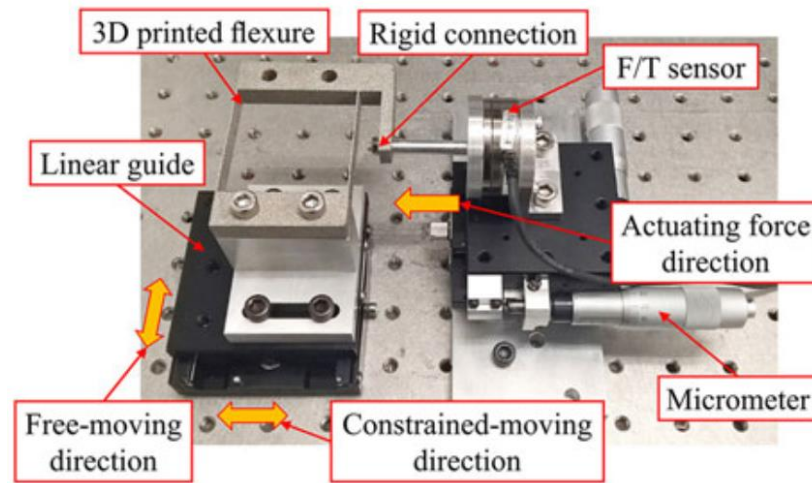
Figure 2.9. Experimental setup for AM stage fabricated by EBM technology. Reprinted from [33].

2.4.3. Composite AM flexure mechanisms

Whilst the mechanism possesses excellent mechanical properties overall, the comparatively low ratio of compressive-to-tensile strength for carbon fibers may be a

disadvantage for the use of carbon fiber-reinforced polymer (CFRP) composites when it is utilized as members of a structure subjected to compressive and/or flexural loading [99-101]. Notwithstanding glass fibers have a lower tensile strength in comparison even to low strength carbon fiber [102-104], their strain-to-failure is higher than carbon fiber due to the lower modulus. Thus, it is possible to incorporate high elongation fibers e.g. glass into low elongation fibers e.g. carbon to enhance the failure strain.

Previous studies about the effects of hybridization on the flexural properties of fiber-reinforced composites have shown varied results. Sudarisman and Davies [105] reported the replacement of 33% of E-glass fibers by S-2 glass fibers produced an increase in the flexural strength of 23%, without any significant effects of hybridization to the flexural modulus. Kalnin [106] found that the flexural strength rapidly decreases as an all-glass reinforcement is gradually replaced by graphite fiber. The theoretical maximum strain failure criteria showed slight positive deviations. A recent study by Sudarisman *et al.* [107] delineated that the optimal placement of glass fibers on the compressive side of a test specimen would magnify flexural performance in CFRP. As such, the study showed an intriguing result that was noted to display a positive hybrid effect through the partial substitution of carbon fibers for glass fibers in the flexural strength, strain at maximum stress, and energy storage at maximum stress. Dong *et al.* [108] presented the flexural properties of hybrid glass and carbon fiber reinforced epoxy composites by conducting both experiments and FEA. Three combinations of the carbon and glass fibers, i.e. S-2&T700S, S-2&TR30S, and E&TR30S, were used to make hybrid composite specimens. Specimens were created by the hand lay-up process in an intra-ply configuration with

31

varying degrees of glass fibers added to the surface of a carbon laminate. Both the experiments and FEA suggest a decrease in flexural modulus with an increasing percentage of glass fibers as shown in Figure 2.10. Positive hybrid effects exist by substituting carbon fibers with glass fibers, and applying a thin layer of GFRP on the compressive surface yields the highest flexural strength.
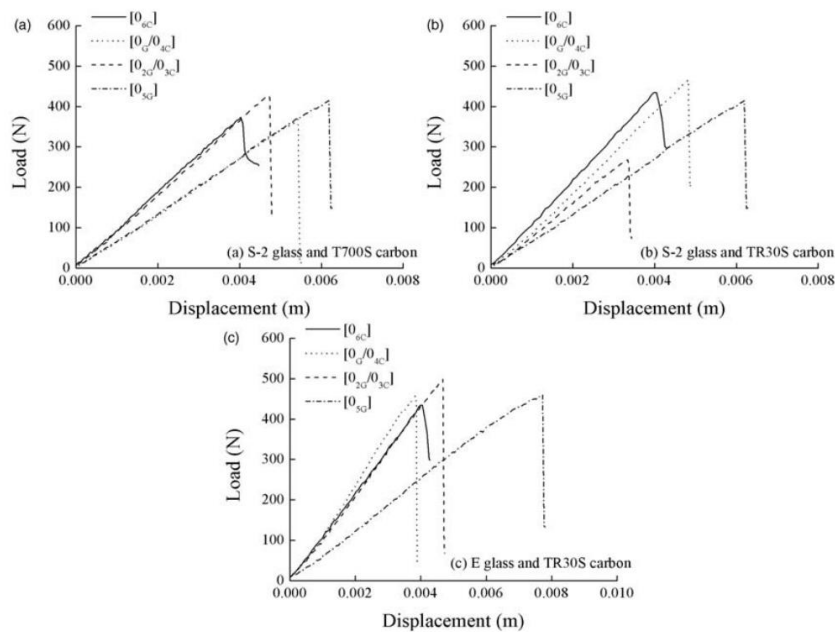
Figure 2.10. Load-displacement curves from flexural tests: (a) S-2 glass and T700S carbon, (b) S-2 glass and TR30S carbon and (c) E glass and TR30S carbon. Reprinted from [108].

2.5. Future Applications and Properties Analysis

2.5.1. Pressure-fed mechanisms

Flexures are primarily constraint elements that utilize material elasticity to produce small, yet frictionless and precise in motions, and an ideal flexure provides infinite

stiffness and zero displacements along its degrees of constraint (DOC). Dynamic and thermal characteristics of the flexures are influenced by constitutive properties of materials, geometric compatibility, or force equilibrium conditions as illustrated in Figure 2.11. In other words, AM technology that makes use of the flexibility in mechanical design can effectively control the material distribution (channel size, shape, and placement) in terms of stiffness, damping, resonance frequency, and heat dissipation of the flexures. In this study, the pressure-fed mechanism applying different pressure across the internal channel was firstly characterized by dynamic and thermal testing.
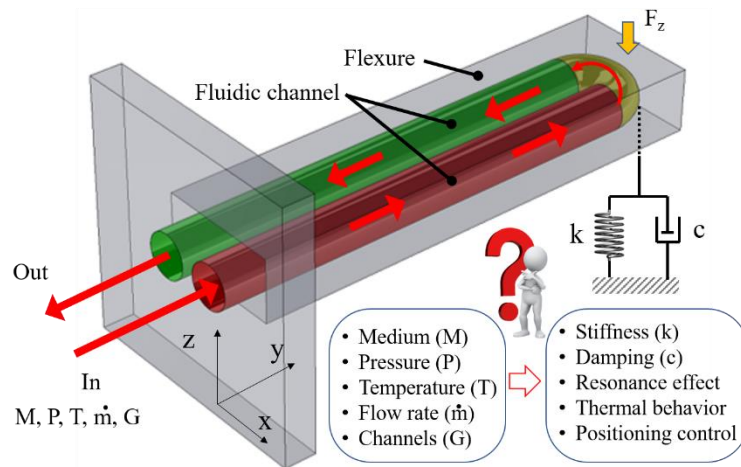
Figure 2.11. A concept of pressure-fed flexure mechanism. Reprinted from [38].

The pressure distribution and direction around each channel surface will be dependent on the channel shape, and the dynamic characteristics of flexures will rely upon the cross-sectional geometry of the channel. Thus, test samples ($30 \times 10 \times 100$ mm^3) of a one-dimensional cantilever beam with various internal channel shapes (Circular,

33

triangular, semicircular, inverse triangular, and inverse semicircular) were designed and fabricated by the AM machine (Connex 500, high fidelity) with the same cross-sectional area. The channel surface area remained constant at 19.625 mm^2. This design compared when only a cross-sectional area affecting material and mechanical properties, a real and volumetric variation of the channels was not taken into account.

The major focus of this paper is on the utilization of AM process for testing dynamic behaviors of AM-manufactured pressure-fed flexures, with the idea of providing controllability of structural stiffness and damping performances. This controlled variable stiffness and damping mechanism can be advantageously applied in robotics [109], adaptive vibration control [110], bio-engineering [111], haptics [112], aerodynamics [113], and architectural structures and manufacturing [114]. As a preliminary study [38], in this paper, the pressure-fed mechanisms with five fluidic channel geometry were tested under various pressure conditions to experimentally study dynamic characteristics of pressure-fed flexure mechanisms. Stiffness, damping ratio, and natural frequency of each cantilever according to varying air pressure conditions were characterized, and dynamic behaviors of each cantilever were discussed.

2.5.2. Dynamic and thermal behaviors of flexures with fluidic channel

Lee *et al.* [38] investigated the effects of the pressure distribution around the surface of the channel on the stiffness of the polymeric flexure with a circular fluidic channel. First, the stiffness of the air tube (inner diameter ø8 mm, outer diameter ø10 mm) was measured according to air pressure condition as shown in Figure 2.12. The displacement data were collected by a capacitive displacement sensor while applying force

to the tube that measured at the same time. It showed that the pressure-fed mechanism could increase the structural stiffness by approximately 33.3%.
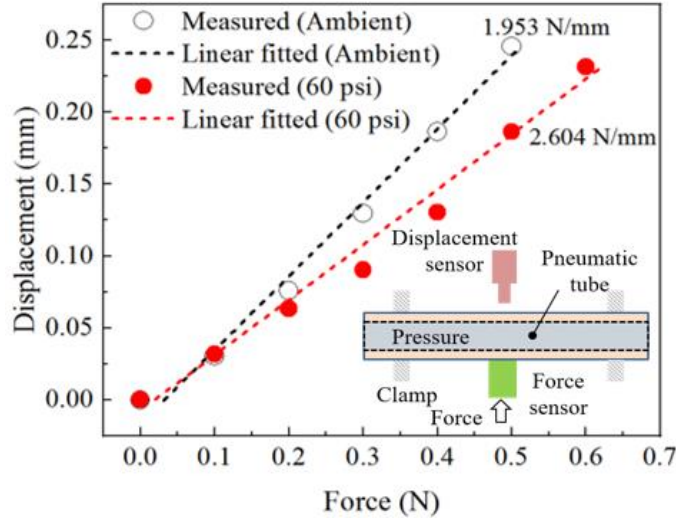
Figure 2.12. Stiffness test results according to the pressure condition in the fluidic channel.

To test the thermal behavior of the AM pressure-fed flexure with an internal fluidic channel, the polymeric cantilever (10×24×100 mm3) with circular (ø5 mm) fluidic channel was designed and fabricated by AM process. The heat source was placed at the end of the cantilever and 5 thermocouples were placed in the flexure. The temperature data were collected under unpressurized condition, pressurized condition (60 psi) and water-filled condition respectively while heating the end area of the cantilever as shown in Figure 2.13 (a). The temperature increased approximately 17 °C in 10 min under unpressured condition. Whereas the temperature increased only 10 °C in 10 min under the pressurized condition and water-filled condition, as shown in Figure 2.13 (b).
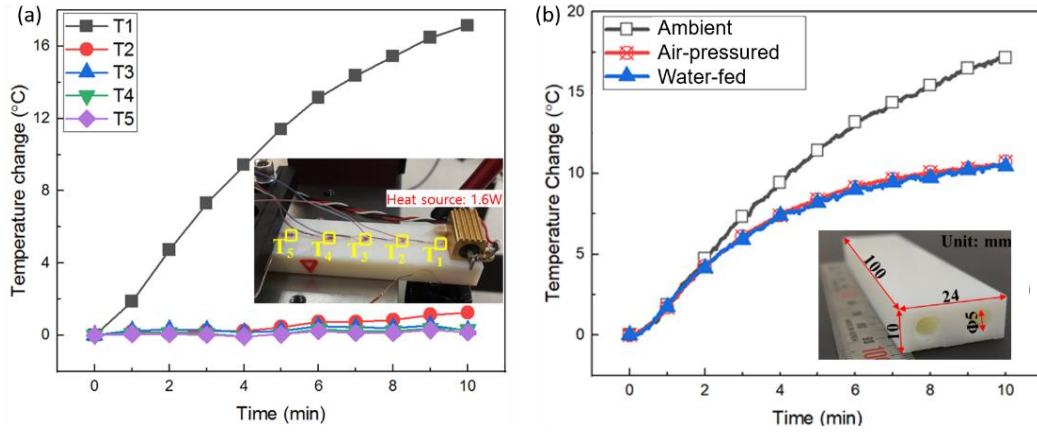
Figure 2.13. Thermal behavior of flexure: (a) temperature distribution along the flexure and (b) cooling effectiveness of medium-fed mechanism. Reprinted from [38].

Water and air pressure conditions showed similar cooling performance. These results indicate that the air or water-fed mechanisms can be used for thermal management in precision systems that are critical to thermal expansion and deformation or thermal noise. As a result of this preliminary study, it was confirmed that the pressure-fed mechanism has a significant influence not only on dynamic characteristics but also on the thermal behavior of the flexure [27]. Further investigation of the pressure-fed AM flexures will allow for adaptive dynamic and thermal control of precision positioning systems and will provide new insight into how to design mechanical system controls.

2.5.3. Thermal issues in flexure mechanisms

The mechanical structure is influenced by environmental conditions. For example, the thermal expansion of a 5 cm long aluminum bar (typical size of nanopositioning stages) subjected to 1 °C change (A typical change that may happen in a controlled environment) may thermally expand 1.2 µm which is roughly 1000 times the resolution of the stage.

Several works have been made to deal with nanopositioning stages [115-117] highlighting the need for using a geometric model combined with thermal compensation. Tan *et al.* [118] notably quantified the influence of thermal drift by creating thermal models. Improvements in performances of the nanopositioning stage were investigated through robot calibration (i.e., open-loop approach) and two models (static and adaptive models) were proposed to compensate for both geometric errors and thermal drift. Validation experiments were conducted over a long period (several days) that showed the accuracy of the stage is improved from a typical micrometer range to 400 nm using the static model and even down to 100 nm using the adaptive model. The experimental results demonstrate that the model efficiently improved the 2D accuracy from 1400 nm to 200 nm.

Lee *et al.* [119] preliminarily investigated the thermal effects of the polymeric AM nanopositioning system. The temperature of three points at the voice coil motor (VCM), the frame near the VCM, and the frame far from the VCM was measured. The temperature was monitored while the flexure was subjected to cyclic loading of 3.6 million cycles in a temperature-controlled lab environment. The temperature of the VCM and the frame near the VCM rapidly increased and saturated at 6.0ºC and 2.5ºC, respectively, after approximately 2 million cycles as shown in Figure 2.14; however, the temperature at the frame far from the VCM remained constant with small fluctuation.
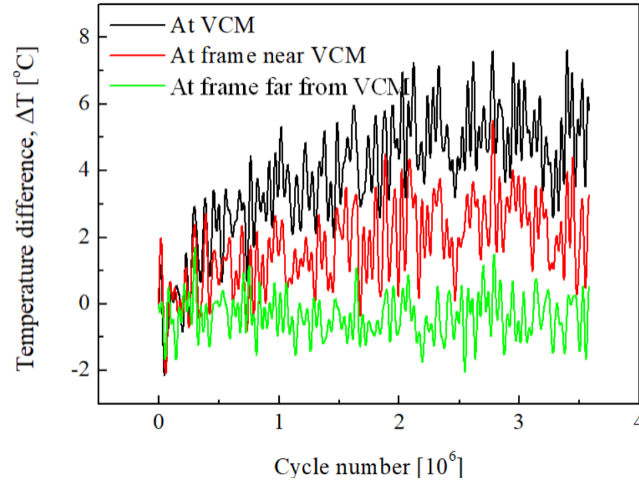
Figure 2.14. Temperature effects: temperature measurement during 3.6 million cycles. Reprinted from [119].

Therefore, to reduce the thermal issues, a novel thermal management strategy for a nanopositioning system architecture for extreme temperature conditions that is capable of low-cost, high signal-to-noise ratio (SNR), high closed-loop dynamic performance, and user-friendly interfaces, have recently proposed by authors. For hardware architecture, the nanopositioning stages will be fabricated using additive manufacturing (AM) technology to maximize the thermo-mechanical design flexibility. As illustrated in Figure 2.15, this flexibility will enhance the passive (conduction) and active (convection) cooling by a fluidic channel array, control of material distribution (overall size and shape), material selection, and manufacturing time and cost. The hydraulic pressure-fed cooling mechanism will be applied to accelerate heat dissipation.

38
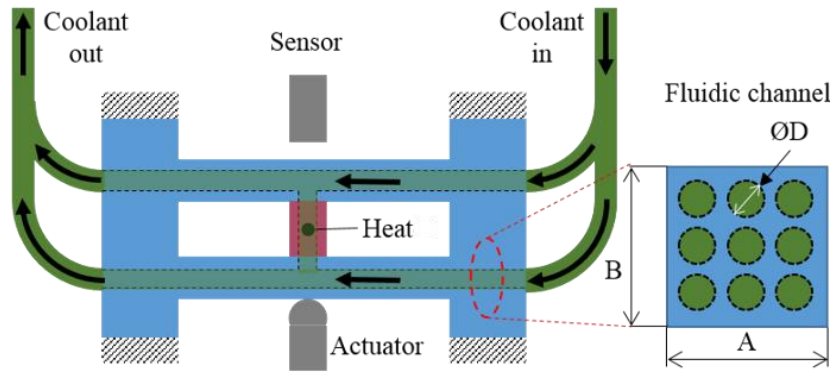
Figure 2.15. Thermal management method using fluidic channels: A and B are the dimension of the beam and D is a diameter.

Through this study, a new thermo-mechanical topology synthesis approach based on AM will also be investigated to eliminate the positioning control issues raised in the stage, sensor, actuator, and controller of nanopositioning systems due to increased temperature. Although the nanopositioning system can avoid an extreme situation by the proposed cooling method, the residual heat that is not removed during the conduction and convection heat transfer can cause positioning error. Thus, advanced control algorithms (e.g., adaptive, iterative, and linear quadratic regulator (LQR) control) [120-122] combined with a thermal compensation based on the reliable mass-spring-damper model of nanopositioning systems (Figure 2.16) will be investigated to achieve accurate and effective positioning control by creating a nanopositioning hardware and software architecture with AM technology for better performance at the extreme temperature conditions.
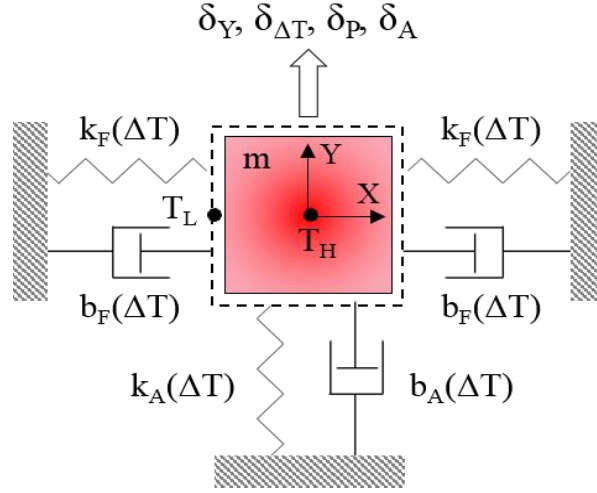
Figure 2.16. Thermo-dynamic model of nanopositioning system.

The dynamic thermo-mechanical model of the moving parts can be built with the parameters: m, mass of moving part; b_F, damping coefficient of flexure; k_F, spring constant of flexure; b_A, damping coefficient of piezo actuator; k_A, spring constant of piezo actuator; T_L, lower temperature; and T_H, upper temperature. All parameters are temperature-dependent, and the displacement measured will include the piezo actuator input displacement (δ_Y), thermal elongation ($\delta_{\Delta T}$), flexure drift (δ_P), and piezo actuator drift (δ_A). Theoretical models of hardware and software architecture will need to be created.

2.5.4. Static and dynamic motion compensation

Dynamic characteristics of compliant mechanisms are highly dependent on constitutive properties of material, geometric compatibility, or force equilibrium conditions [12]. Unlike conventional manufacturing methods such as electric discharge machining, waterjet machining, and micro-milling, an additive manufacturing technology applied with mechanical design flexibility can impressively control the material

distribution in terms of stiffness, damping, and natural frequency. Also, AM methods can fundamentally change the current design principles to improve their own performance such as accuracy, precision, repeatability, or removing motion error at a low-cost.

In the author's preliminary study [123], as shown in Figure 2.17 (a), the internal fluidic channels in the spring structures of the compliant mechanism were designed to give a different compressed air pressure across the internal fluidic channels. The pressure distribution can be monitored from four pressure gauges installed in inlets and outlets. The stiffness ($k_{X,L}$, $k_{X,R}$) and damping ($c_{X,L}$, $c_{X,R}$) may be disparate due to AM tolerance, and the displacement $\delta_{X,L}$ and $\delta_{X,R}$ may also be different when the force (F) applied to the shuttle part might not be perfectly aligned with the principal direction of the compliant mechanism as it can generate yaw error depending on the two displacement amplitudes as described in figure 2.17 (b) and (c). Since the bilateral spring structures are monolithically connected and there are force-displacement interactions between each spring structure, it is difficult to estimate or measure the dynamic parameters (stiffness and damping) independently. It could be rather convenient or preferred to measure the motion error of compliant mechanisms. The proposed pressure-fed mechanism can separately control bilateral spring structures, and the difference in pressure can be in-situ adjusted according to the linear motion results to make the displacement $\delta_{X,L}$ same as the displacement $\delta_{X,R}$. Moreover, it can play a crucial role to assist the actuator to push and pull the shuttle.

41
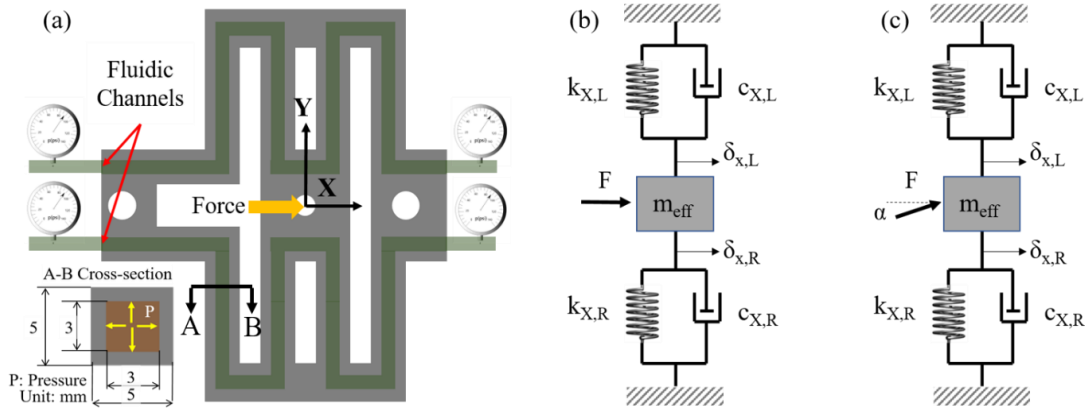
Figure 2.17. Operating principle of the proposed pressure-fed mechanism: (a) schematic description, (b) dynamic model and (c) dynamic model when the force is not applied along the principal direction. Reprinted from [123].

2.5.5. Dimensional metrology for additive manufacturing by X-ray computerized tomography

AM, perhaps, is most appealing to industries aim at low-volume production of highly customized parts for specific applications. The main challenge for the continued adoption of AM in industries is the uncertainty in structural properties of fabricated parts. In a previous study [10], it was found that this uncertainty arises from the microstructural heterogeneities of AM parts and randomly dispersed defects. There still remain significant gaps in fully understanding and establishing the relationship between the process, structure, property, and performance of AM parts. In this past research, the characteristics of crack and related challenges inherent to metallic parts fabricated via laser-assisted AM were analyzed by an X-ray computerized tomography (CT) scanner.

The current CT scan software supplies extensive analysis tools for quantifying defects and deviations of wall thickness and creating nominal to actual comparisons.

42

Figure 2.18 (a) presents an example of the features that can be measured by using this technique. The right image shown in Figure 2.18 (c) is a cross-section of the scan of a solid flexure and a solid model obtained using the CT scan data and the sectional planes are shown in Figure 2.18 (b). Furthermore, the quality of the AM stage was investigated by the use of X-ray CT (METROTOM® 800, resolution ~5 µm). The scanned data was compared with the original CAD data, and the error of fabrication was analyzed. The variation (error of fabrication) over the whole flexure area was less than 0.1 mm (Figure 2.18 (a)), and the air-voids were not found in the flexure area as well as the ground frame (Figure 2.18 (b)). In addition, the geometry of the cross-sectional area at the half-plane along the Z-direction was monitored as seen in Figure 18c and the obtained data shows that the designed stage was successfully fabricated without any air-voids and shape irregularity within the CT scanning-resolution limit. We concluded that the X-ray CT scanning to be an alternative method for investigating the defect of AM-applied devices and the fabrication performance of the AM process.
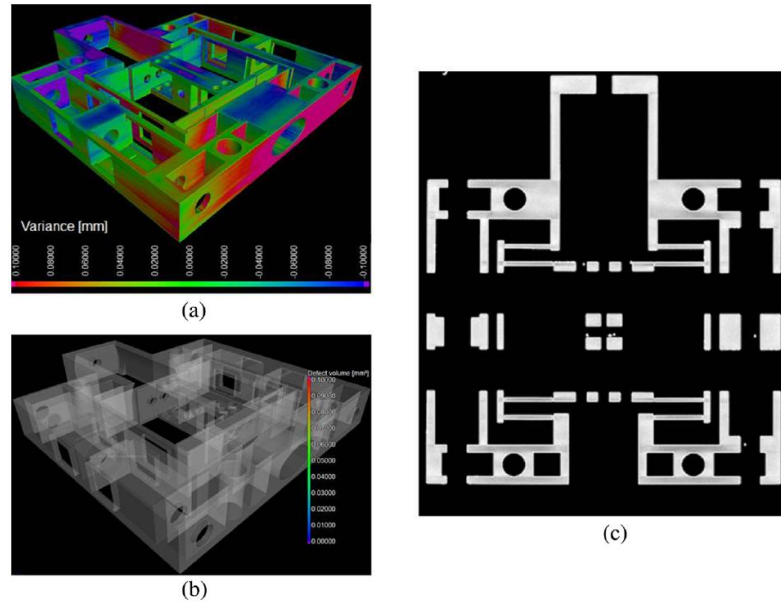
Figure 2.18. Images of the flexure mechanism measured by X-ray CT: (a) fabrication error analysis, (b) defect analysis, and (c) cross-sectional view at the half-plane. Reprinted from [10].

2.5.6. Reliability and repeatability of flexure mechanism motion and AM manufacturing process

To obtain high precision motion quality, precision devices should have the ability to perform the repeatable motion and therefore it can be considered as a reliable motion mechanism. As discussed in section 2.5.3, Lee *et al.* [119] preliminarily conducted research on the thermal effects of flexure mechanism as well as investigating the performance of flexural deflection and stress. The polymeric flexure mechanism was fabricated by AM. The VCM ran the cycle loading of 3.3 million cycles to compare the results of the step response before and after the cycle loading. The positioning accuracy and control of the step response did not significantly influenced by the number of cycle

loadings as shown in Figure 2.19. Moreover, two measurements tracked the reference input with almost no variation in the steady-stated response characteristics. However, the small distinction was observed in rising and falling time. It was assumed that the temperature variation in the flexure structure after 3.6 million cycles had influenced the material properties of the flexure mechanism as well as the dynamic characteristics of the designed flexure mechanism.
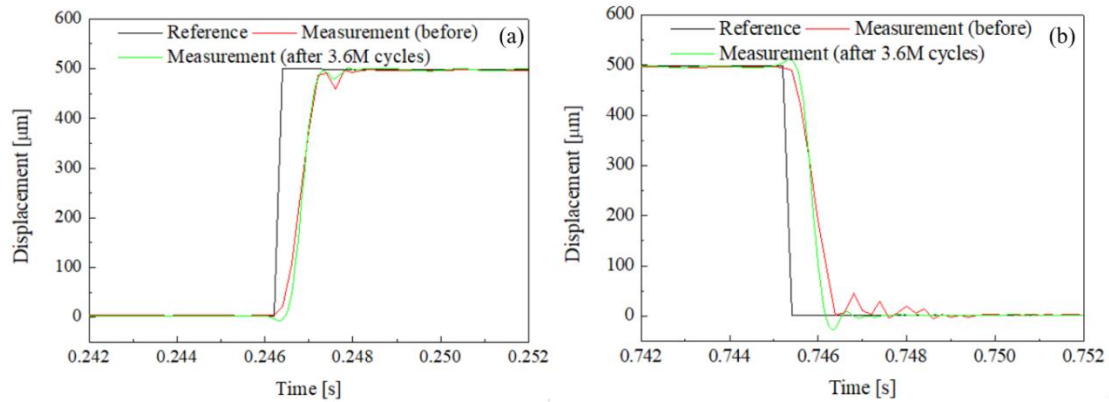
Figure 2.19. Positioning control effectiveness after 3.6 million cycle loadings: forward (a) and backward (b). Reprinted from [119].

Though the step response showed little distinction in rising and falling time, the overall motion behavior of AM manufactured flexure mechanism showed the repeatable response and it was found out that the positioning accuracy was reliable comparing with the reference input.

Utilizing the AM manufacturing enables to create intricate geometry such as internal channels that could not be able to achieve through traditional manufacturing methods. Chun *et al.* [123] investigated the proposed flexure-based compliant mechanism that was additively manufactured (metal power bed). Since the flexure mechanism was additively manufactured, the AM manufacturing material, denoted as AM SS, was characterized and evaluated with conventional manufacturing material, denoted as Bulk SS, to validate the AM process as the alternative manufacturing methods. X-ray powder diffraction (XRD) was utilized to determine the composition of material composition. The results, as shown in Figure 2.20, indicated that the AM SS and the Bulk SS showed identical material compositions due to the same angles of sharp intensity peaks.
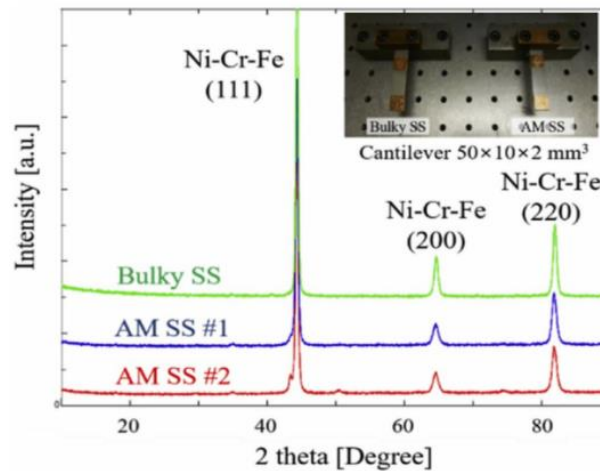
Figure 2.20. Comparison of the XRD pattern of AM SS and Bulk SS samples. Reprinted from [123].

Further investigation was done by comparing the dynamic characteristics in damping coefficient and natural frequency which are the crucial parameters for flexure mechanisms. The comparison results indicated that, as shown in Figure 2.21, in the natural frequency, there exists approximately 1% difference between AM SS and Bulk SS. In addition, the range of damping coefficients of the two samples was from 0.005 to 0.01. Hence, it was considered that the compliant mechanisms manufactured by AM process can be considered as one of the manufacturing methods to fabricate compliant mechanisms.
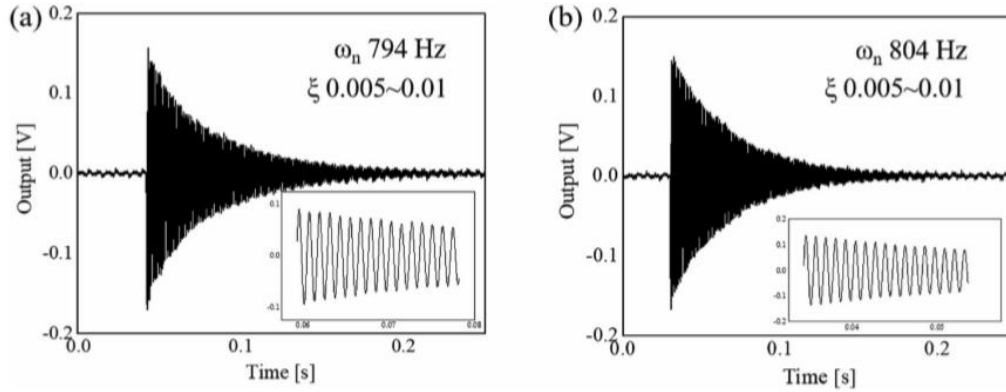
Figure 2.21. Free-vibration comparison between (a) Bulk SS and (b) AM SS. Reprinted from [123].

The void analysis was also performed to detect the flaw such as cracks and porosities by an industrial CT scan. As shown in Figure 2.22, while the bulk SS sample exhibits the uniform void size as approximately 3,000 μm, the void size of AM SS sample reveals irregularly up to 120,000 μm. It was considered that the AM SS material was layer-by-layer printed. However, it was hard to draw the conclusion that the AM manufacturing

process is not suitable for the flexure mechanism since it may be attractive to some designers to fabricate the flexure mechanism as long as the dynamic characteristics meet the criteria.
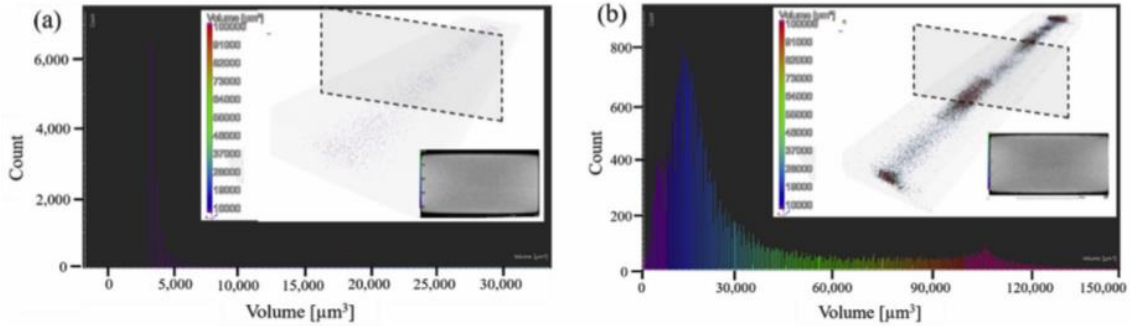
Figure 2.22. Void analysis of (a) Bulk SS and (b) AM SS. Reprinted from [123].

As discussed in section 2.5.5, the polymeric flexure mechanism fabricated by the stereolithography (STL) method showed around ±0.1 mm surface variation for its fabrication error when the printing resolution was 0.5 µm. Additionally, the flexure mechanism was fabricated without exhibiting any shape irregularity and air-voids within the resolution limitation of CT scanning. Villarraga *et al.* [48] assessed the different polymeric flexure stages with the X-Ray CT method, and it was found that the surface tolerance was within ± 0.15 mm when the same printing resolution was applied to fabricate the flexure mechanism. The difference of surface variation in two different flexure mechanisms when the same printing resolution applied might be from other uncertainties such as the printing temperature. Though it showed some differences in surface variations, the difference was about ± 50 µm and if the printing condition is properly controlled such

as heating and cooling rate, operating temperature, and printing speed, then the differences in surface variations expected to be less. Therefore, the AM process can be considered as one of a repeatable process and considered as one of the attractive fabrication methods.
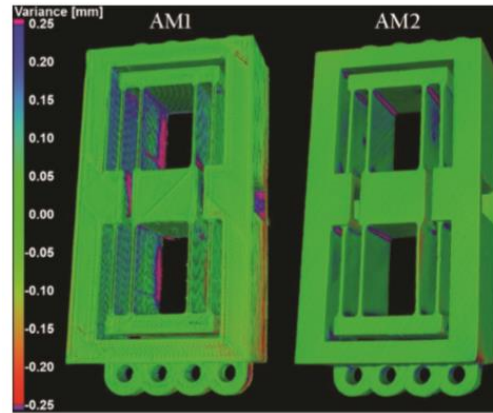
Figure 2.23. Fabrication error comparison with printing resolution of 100 µm (AM1) and 0.5 µm (AM2). Reprinted from [48].

2.5.7. New materials and structures of flexure mechanisms

The two biggest issues with conventional mechanisms are fabrication and selection of materials. Plastic prototypes can be readily manufactured with a low-cost using 3D printing or molding and employed the large elasticity of polymers. However, the use of polymer mechanisms is inappropriate for structural applications because of their low strength and degradation, particularly in spacecraft (polymers degrade in space due to the high UV exposure). Hence, the utilization of amorphous metals and their composites [124-128], the so-called AMCs (amorphous metal composites), is ideal for both the mechanical properties and processing of compliant mechanisms and flexures. AMCs are composite

alloys that have high strength, the elasticity of polymers, and the processability of plastics, which provide similar properties and processing ability to monolithic AM structures. Thus, they can be easily fabricated into a monolithic mechanism at a significantly lower cost than machining, and exhibit better performance than any other crystalline material under the same application. Since AMCs can be fabricated using reusable steel or brass molds, many parts can be fabricated by spending only the initial material cost and the initial mold cost which allows for many mechanisms to be cheaply made. These materials have the capability to be much tougher (to avoid brittle failure), much higher fracture toughness, and fatigue life. It can also be controlled to have a low coefficient of thermal expansion (CTE) by utilizing low CTE inclusions [129]. Until now, these combinations of properties (mechanical performance and processing ability) have not been utilized for compliant mechanisms.

AM alloys (which are also known as bulk metallic glasses or BMGs) and their composites [130-135] can be easily made up into optomechanical, compliant, or flexure mechanisms at a low-cost. To accomplish the fabrication, a selected composition of AM or AMC needs to be fabricated into a feedstock material that is heated (using radiofrequency heating or resistance heating) and forged into a final part with either net or near-net shape. Because AM alloys have the characteristic of low-melting temperatures, just like plastic, they can be melted and forced into a very complex mold, but simultaneously form a glass under the high cooling rate that obtained by cooling lines in the mold. The quenched part does not react with the mold and is mechanically robust enough to survive from the ejection process. The final part has the equivalent tolerances

as the mold (since there is very little shrinkage when forming a glassy metal) and yet can be removed without damage to the mold. This offers the potential to develop mechanisms that outperform currently available metals (aluminum, titanium, and steel) but that also can be fabricated at a low-cost with a repeatable process.

It has been shown in the literature that microstructure and its corresponding mechanical properties are a crucial function of the printing parameters that control the thermal history of the so-called "melt-pool" [136-139]. Moreover, many researchers have demonstrated the application method of flexibly controlling the print parameters during printing to create a gradient of microstructures and mechanical properties across the part. The basis of this idea was following 'paths' in phase diagrams to achieve certain phases by controlling the temperature of the melt pool at the nozzle. Building off this idea, it is likely possible to also manipulate dynamic properties in a similar way.

Granato and Lucke [140] established a model with the damping and modulus changes to dislocations quantitatively and they also presented the inverse relationship between the modulus and damping. Dislocations within the lattice are considered as a defect because of their inverse relationship with stiffness or moduli. However, dislocations have a positive correlation with mechanical damping. These relationships motivate a material for flexure mechanisms to form a technique that can achieve a highly damped core, stiff outer layers, and tight control on the topological gradient of these properties. Dislocations are generated by four major factors:

- Homogeneous nucleation
- Grain boundary initiation

- Interfaces between the lattice and the surfaces

- Interfaces between precipitates and/or dispersed phases.

AM techniques in the present state for metals can feasibly control the interface between the lattice and surfaces as well as precipitates and/or dispersed phases. The porosity can be controlled by a feed; a more porous core will greatly generate surface area which causes an increase in dislocations. Furthermore, the control of the melt pool temperature along with the concentration of alloying agents can manage the formation, density of precipitates, and/or dispersed phases. Besides, temperature control leads to control over the size of the grain, which further increases the number of dislocations to be damping.

Using these ideas and the findings of the preliminary research, a monolithic flexure can be generated, including a highly damped core that gradually stiffens along with the thickness. The success of this idea will lead to further researches on the application for flexure systems such as a metrological nanopositioning stage that exhibits strong resistance to out of plane motions and faster-operating speed than conventional stages. Furthermore, the geometrical benefits of additive manufacturing over traditional machining will lead to facilitate topology optimization. This can be combined with micro and macrostructure design to create significant increases in performance.

Due to the need in stringent breaking strength and constraints of design, flexures are commonly made out of non-transparent materials that interfere with the use in miniaturized optics in general and especially in integrated optomechanics. Here, Bellouard [141] reported on the mechanical properties of transparent flexures made out of fused

silica. By using a femtosecond laser, this report proved that high flexural strength can be achieved, which opens new opportunities in the design of monolithically integrated optomechanical devices.

The amorphous phase of SiO_2, fused silica (a-SiO_2) is one of the most common high-quality optical substrates transparent to a broad spectrum (from about 170 nm to above 2.5 µm). It is inert to most chemicals, which also makes it a wide range of material selection for broad biological studies. Fused silica has a very low coefficient of thermal expansion (0.55 10-6 /°C) and is resistant to thermal shocks. It also possesses a low density (2200 kg/m^3) and Young's modulus (72 GPa) comparable to that of aluminum alloys. It is an attractive material for flexures, though initially counterintuitive.
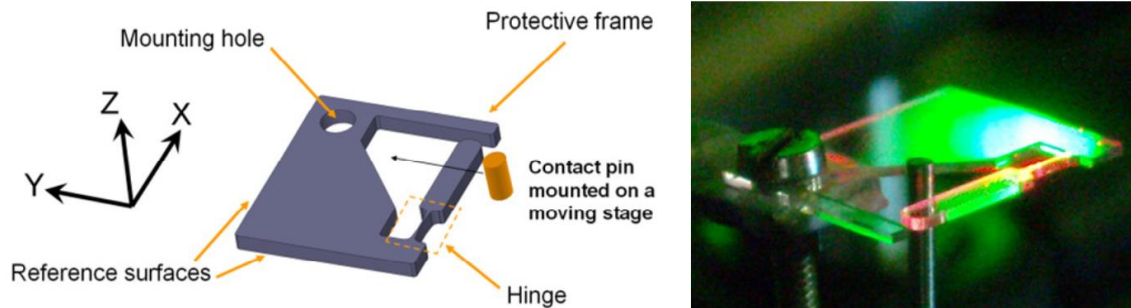
Figure 2.24. A single-degree-of-freedom translational flexure stage made of 1 mm-thick fused silica. Reprinted from [141].

2.6. Summary

The AM technology for precision engineering motion devices has been first reviewed in academic society. The AM fabrication method with its materials and properties are compared with those current traditional manufacturing methods. Moreover,

the common defects and its proper inspection methods in AM technology which directly influence the performance of nanopositioning systems are discussed, where fatigue is the most sensitive property. Some researches focused on thermal, static and dynamic performance, new material, and structure design for further applications are also summarized. This review provided the potential for new insights in using AM technology for smart structures-based precision engineering devices to break through the current performance and structural limitations. The AM technology promises to create a new structural/thermal design principle for flexures and to provide the most outstanding performances in terms of precision, long-term stability as well as the advantages of compactness, low-profile, and low-cost. The reviewed technology will quickly lead to high productivity, innovation, higher-quality products, and energy efficiency. Ultimately, the technology will offer solutions with a variety of options for smart materials, structures, and advanced manufacturing.

2.7. Acknowledgement

2.8. References

[1]   Asd Campbell, I., Diegel, O., Kowen, J., & Wohlers, T. (2018). Wohlers report 2018: 3D printing and additive manufacturing state of the industry: annual worldwide progress report: Wohlers Associates.

[2]   Sommer, C., & Sommer, S. (2017). Complete EDM handbook: Advance Publishing Incorporated.

[3]   "Waterjet machining tolerances" (2019) available at https://waterjets.org/ (accessed 28th June. 2019).

[4]   Guckenberger, D. J., de Groot, T. E., Wan, A. M., Beebe, D. J., & Young, E. W. (2015). Micromilling: a method for ultra-rapid prototyping of plastic microfluidic devices. Lab on a Chip, 15(11), 2364-2378.

[5]   Aliakbari, M. (2012). Additive manufacturing: State-of-the-art, capabilities, and sample applications with cost analysis. In.

[6]   Bhavar, V., Kattire, P., Patil, V., Khot, S., Gujar, K., & Singh, R. (2017). A review on powder bed fusion technology of metal additive manufacturing. In Additive Manufacturing Handbook (pp. 251-253): CRC Press.

[7]   Villarraga-Gómez, H., Lee, C., & Smith, S. T. (2018). Dimensional metrology with X-ray CT: A comparison with CMM measurements on internal features and compliant structures. Precision Engineering, 51, 291-307.

[8]   Lee, C., Stepanick, C. K., Lee, S.-K., & Tarbutton, J. A. (2016). Cross-coupling effect of large range XY nanopositioning stage fabricated by stereolithography process. Precision Engineering, 46, 81-87.

[9]   Lee, C., Lee, S.-K., & Tarbutton, J. A. (2015). Positioning control effectiveness of optical knife edge displacement sensor-embedded monolithic precision stage. Sensors and Actuators A: Physical, 233, 390-396.

[10]   Lee, C., & Tarbutton, J. A. (2015). Compliance and control characteristics of an additive manufactured-flexure stage. Review of Scientific Instruments, 86(4), 045107.

[11]   Howell, L. L., Magleby, S. P., & Olsen, B. M. (2013). Handbook of compliant mechanisms: John Wiley & Sons.

[12]   Smith, S. T. (2000). Flexures: elements of elastic mechanisms: Crc Press.

[13] Henein, S. (2001). Conception des guidages flexibles: PPUR presses polytechniques.

[14] Lee, C., Jeon, S., Stepanick, C. K., Zolfaghari, A., & Tarbutton, J. A. (2017). Investigation of optical knife edge sensor for low-cost, large-range and dual-axis nanopositioning stages. Measurement, 103, 157-164.

[15] Zolfaghari, A., Jeon, S., Stepanick, C. K., & Lee, C. (2017). A novel sensor for two-degree-of-freedom motion measurement of linear nanopositioning stage using knife edge displacement sensing technique. Review of Scientific Instruments, 88(6), 065110.

[16] Lee, C. (2017). Long-range nano-scanning devices based on optical sensing technology. In Advanced Mechatronics and MEMS Devices II (pp. 495-522): Springer.

[17] Awtar, S., Slocum, A. H., & Sevincer, E. (2007). Characteristics of beam-based flexure modules.

[18] Awtar, S., & Parmar, G. (2010). Physical and control systems design challenges in large range nanopositioning. IFAC Sym. on Mechatronic Systems, Cambridge, MA.

[19] Eves, B. J. (2009). Design of a large measurement-volume metrological atomic force microscope (AFM). Measurement Science and Technology, 20(8), 084003.

[20] Werner, C., Rosielle, P., & Steinbuch, M. (2010). Design of a long stroke translation stage for AFM. International journal of machine tools and manufacture, 50(2), 183-190.

[21] Kim, Y. S., Dagalakis, N. G., & Gupta, S. K. (2014). Design of MEMS based three-axis motion stage by incorporating a nested structure. Journal of Micromechanics and Microengineering, 24(7), 075009.

[22] Sun, L., Wang, J., Rong, W., Li, X., & Bao, H. (2008). A silicon integrated micro nano-positioning XY-stage for nano-manipulation. Journal of Micromechanics and Microengineering, 18(12), 125004.

[23] Thompson, M. K., Moroni, G., Vaneker, T., Fadel, G., Campbell, R. I., Gibson, I., & Martina, F. (2016). Design for Additive Manufacturing: Trends, opportunities, considerations, and constraints. CIRP annals, 65(2), 737-760.

[24] Altaf, K., Rani, A. M. A., & Raghavan, V. R. (2013). Prototype production and experimental analysis for circular and profiled conformal cooling channels in aluminium filled epoxy injection mould tools. Rapid Prototyping Journal.

[25] Fiaz, H. S., Settle, C. R., & Hoshino, K. (2016). Metal additive manufacturing for microelectromechanical systems: Titanium alloy (Ti-6Al-4V)-based nanopositioning flexure fabricated by electron beam melting. Sensors and Actuators A: Physical, 249, 284-293.

[26] Fabrication of piezo driven micro-positioning 3-dof stage with flexure hinges using multi-material 3-d printer, (2015), KR101647598B1.

[27] Precision positioning device, (2017), KR101957244B1.

[28] Manufacturing of multi-degree-freedom precise stage comprising multi-materials and using three-dimensional printer, (2018), US20180126503A1.

[29] Techniques for designing and manufacturing precision-folded, high strength, fatigue-resistant structures, (2015), EP1599400B1.

[30] Equipment for manufacturing large-size metal part in high energy beam additive manufacturing mode and control method of equipment, (2016), CN104001915A.

[31] Fiaz, H. S., Settle, C. R., & Hoshino, K. (2016). Metal additive manufacturing for microelectromechanical systems: Titanium alloy (Ti-6Al-4V)-based nanopositioning flexure fabricated by electron beam melting. Sensors and Actuators A: Physical, 249, 284-293.

[32] Wei, H., Wang, L., Niu, X., Zhang, J., & Simeone, A. (2018). Fabrication, Experiments, and Analysis of an LBM Additive-Manufactured Flexure Parallel Mechanism. Micromachines, 9(11), 572.

[33] Pham, M. T., Teo, T. J., Yeo, S. H., Wang, P., & Nai, M. L. S. (2017). A 3-D printed Ti-6Al-4V 3-DOF compliant parallel mechanism for high precision manipulation. IEEE/ASME Transactions on Mechatronics, 22(5), 2359-2368.

[34] Wang, P., & Xu, Q. (2017). Design and testing of a flexure-based constant-force stage for biological cell micromanipulation. IEEE Transactions on automation science and engineering, 15(3), 1114-1126.

[35] Sharkey, J. P., Foo, D. C., Kabla, A., Baumberg, J. J., & Bowman, R. W. (2016). A one-piece 3D printed flexure translation stage for open-source microscopy. Review of Scientific Instruments, 87(2), 025104.

[36] Sun, L., Wang, J., Rong, W., Li, X., & Bao, H. (2008). A silicon integrated micro nano-positioning XY-stage for nano-manipulation. Journal of Micromechanics and Microengineering, 18(12), 125004.

[37] Clark, L., Shirinzadeh, B., Zhong, Y., Tian, Y., & Zhang, D. (2016). Design and analysis of a compact flexure-based precision pure rotation stage without actuator redundancy. Mechanism and Machine Theory, 105, 129-144.

[38] Han, J., & Lee, C. (2019). Dynamic and thermal characterization of additively manufactured pressure-fed flexures with internal fluidic channels. Smart Materials and Structures, 28(10), 105032.

[39] Zhang, Z., Liu, Z., & Yan, P. (2016). Design of a flexure-based XY positioning stage with balanced axial forces on decoupling modules. Paper presented at the 2016 IEEE International Conference on Manipulation, Manufacturing and Measurement on the Nanoscale (3M-NANO).

[40] Fiaz, H., & Hoshino, K. (2015). Large displacement nanopositioning flexure fabricated by direct 3D printing of Titanium. Paper presented at the 2015 Transducers-2015 18th International Conference on Solid-State Sensors, Actuators and Microsystems (TRANSDUCERS).

[41] Roy, N., & Cullinan, M. (2016). Design of a flexure based XY precision nanopositioner with a two inch travel range for micro-scale selective laser sintering. Paper presented at the Proceedings of the ASPE 2016 Annual Meeting, Portland, OR, USA.

[42] Merriam, E. G., Jones, J. E., & Howell, L. L. (2014). Design of 3D-printed titanium compliant mechanisms. Paper presented at the 42nd Aerospace Mechanism Symposium.

[43] Gao, W., Zhang, Y., Ramanujan, D., Ramani, K., Chen, Y., Williams, C. B., & Zavattieri, P. D. (2015). The status, challenges, and future of additive manufacturing in engineering. Computer-Aided Design, 69, 65-89.

[44] Vock, S., Klöden, B., Kirchner, A., Weißgärber, T., & Kieback, B. (2019). Powders for powder bed fusion: a review. Progress in Additive Manufacturing, 1-15.

[45] King, W. E., Anderson, A. T., Ferencz, R. M., Hodge, N. E., Kamath, C., Khairallah, S. A., & Rubenchik, A. M. (2015). Laser powder bed fusion additive manufacturing of metals; physics, computational, and materials challenges. Applied Physics Reviews, 2(4), 041304.

[46] Goodridge, R., & Ziegelmeier, S. (2017). Powder bed fusion of polymers. Laser Additive Manufacturing, 181-204. Woodhead Publishing.

[47] Mower, T. M., & Long, M. J. (2016). Mechanical behavior of additive manufactured, powder-bed laser-fused materials. Materials Science and Engineering: A, 651, 198-213.

[48] Villarraga, H., Lee, C., Corbett, T., Tarbutton, J. A., & Smith, S. T. (2015). Assessing additive manufacturing processes with X-ray CT metrology. Paper presented at the ASPE spring topical meeting: achieving precision tolerances in additive manufacturing.

[49] Leuders, S., Thöne, M., Riemer, A., Niendorf, T., Tröster, T., Richard, H. a., & Maier, H. (2013). On the mechanical behaviour of titanium alloy TiAl6V4 manufactured by selective laser melting: Fatigue resistance and crack growth performance. International Journal of Fatigue, 48, 300-307.

[50] Song, B., Zhao, X., Li, S., Han, C., Wei, Q., Wen, S., Shi, Y. (2015). Differences in microstructure and properties between selective laser melting and traditional manufacturing for fabrication of metal parts: A review. Frontiers of Mechanical Engineering, 10(2), 111-125.

[51] Shifeng, W., Shuai, L., Qingsong, W., Yan, C., Sheng, Z., & Yusheng, S. (2014). Effect of molten pool boundaries on the mechanical properties of selective laser melting parts. Journal of Materials Processing Technology, 214(11), 2660-2667.

[52] Brice, C., Shenoy, R., Kral, M., & Buchannan, K. (2015). Precipitation behavior of aluminum alloy 2139 fabricated using additive manufacturing. Materials Science and Engineering: A, 648, 9-14.

[53] Brice, C., & Fraser, H. (2003). Characterization of Ti-Al-Er alloy produced via direct laser deposition. Journal of materials science, 38(7), 1517-1521.

[54] Brice, D. A., Ghamarian, I., Mendoza, M., Samimi, P., Hayes, B. J., Ott, R. T., Kuhr, S. J. (2016). On the prediction and engineering of microstructures and properties in additively manufactured metallic materials. Paper presented at the SAMPE Long Beach 2016 Conference and Exhibition.

[55] Liu, Q. C., Elambasseril, J., Sun, S. J., Leary, M., Brandt, M., & Sharp, P. K. (2014). The effect of manufacturing defects on the fatigue behaviour of Ti-6Al-4V specimens fabricated using selective laser melting. Paper presented at the Advanced Materials Research.

[56] Lu, S. L., Tang, H., Ning, Y., Liu, N., StJohn, D., & Qian, M. (2015). Microstructure and mechanical properties of long Ti-6Al-4V rods additively manufactured by selective electron beam melting out of a deep powder bed and the effect of subsequent hot isostatic pressing. Metallurgical and Materials Transactions A, 46(9), 3824-3834.

[57] Tammas-Williams, S., Withers, P. J., Todd, I., & Prangnell, P. B. (2016). The effectiveness of hot isostatic pressing for closing porosity in titanium parts manufactured by selective electron beam melting. Metallurgical and Materials Transactions A, 47(5), 1939-1946.

[58] Gong, X., Lydon, J., Cooper, K., & Chou, K. (2014). Beam speed effects on Ti–6Al–4V microstructures in electron beam additive manufacturing. Journal of Materials Research, 29(17), 1951-1959.

[59] Rombouts, M., Kruth, J.-P., Froyen, L., & Mercelis, P. (2006). Fundamentals of selective laser melting of alloyed steel powders. CIRP annals, 55(1), 187-192.

[60] Slotwinski, J., & Moylan, S. (2014). Metals-based additive manufacturing: metrology needs and standardization efforts. Paper presented at the 2014 ASPE Spring Topical Meeting: Dimensional Accuracy and Surface Finish in Additive Manufacturing, Berkeley, CA, April.

[61] Slotwinski, J. A. (2014). Additive manufacturing: Overview and NDE challenges. Paper presented at the AIP Conference Proceedings.

[62] Slotwinski, J. A., & Garboczi, E. J. (2014). Porosity of additive manufacturing parts for process monitoring. Paper presented at the AIP conference proceedings.

[63] Slotwinski, J. A., Garboczi, E. J., Stutzman, P. E., Ferraris, C. F., Watson, S. S., & Peltz, M. A. (2014). Characterization of metal powders used for additive manufacturing. Journal of research of the National Institute of Standards and Technology, 119, 460.

[64] Ng, G., Jarfors, A., Bi, G., & Zheng, H. (2009). Porosity formation and gas bubble retention in laser metal deposition. Applied Physics A, 97(3), 641.

[65] Gockel, J., Fox, J., Beuth, J., & Hafley, R. (2015). Integrated melt pool and microstructure control for Ti–6Al–4V thin wall additive manufacturing. Materials Science and Technology, 31(8), 912-916.

[66] Gong, H., Rafi, K., Gu, H., Starr, T., & Stucker, B. (2014). Analysis of defect generation in Ti–6Al–4V parts made using powder bed fusion additive manufacturing processes. Additive Manufacturing, 1, 87-98.

[67] Barua, S., Liou, F., Newkirk, J., & Sparks, T. (2014). Vision-based defect detection in laser metal deposition process. Rapid Prototyping Journal.

[68] Taheri, H., Shoaib, M., Koester, L. W., Bigelow, T. A., Collins, P. C., & Bond, L. J. (2017). Powder based additive manufacturing-A review of types of defects, generation mechanisms, detection, property evaluation and metrology. Int. J. Addit. Subtractive Mater. Manuf, 1(2), 172-209.

[69] Benson, J. M., & Snyders, E. (2015). The need for powder characterisation in the additive manufacturing industry and the establishment of a national facility. South African Journal of Industrial Engineering, 26(2), 104-114.

[70] Lee, S.-Y., Kim, T.-S., Lee, J.-K., Kim, H.-J., Kim, D. H., & Bae, J. (2006). Effect of powder size on the consolidation of gas atomized Cu54Ni6Zr22Ti18 amorphous powders. Intermetallics, 14(8-9), 1000-1004.

[71] Stencel, J., Li, T., Neathery, J., & Lherbier, L. (2000). Removal of ceramic defects from a superalloy powder using triboelectric processing. Superalloys, 5, 95-99.

[72] Moylan, S., Whitenton, E., Lane, B., & Slotwinski, J. (2014). Infrared thermography for laser-based powder bed fusion additive manufacturing processes. Paper presented at the AIP Conference Proceedings.

[73] Philtron, J. H., & Rose, J. L. (2014). Guided wave phased array sensor tuning for improved defect detection and characterization. Paper presented at the Nondestructive Characterization for Composite Materials, Aerospace Engineering, Civil Infrastructure, and Homeland Security 2014.

[74] Abd-Elghany, K., & Bourell, D. (2012). Property evaluation of 304L stainless steel fabricated by selective laser melting. Rapid Prototyping Journal.

[75] Tapia, G., & Elwany, A. (2014). A review on process monitoring and control in metal-based additive manufacturing. Journal of Manufacturing Science and Engineering, 136(6).

[76] Chua, Z. Y., Ahn, I. H., & Moon, S. K. (2017). Process monitoring and inspection systems in metal additive manufacturing: Status and applications. International Journal of Precision Engineering and Manufacturing-Green Technology, 4(2), 235-245.

[77] Moon, S. K., Tan, Y. E., Hwang, J., & Yoon, Y.-J. (2014). Application of 3D printing technology for designing light-weight unmanned aerial vehicle wing structures. International Journal of Precision Engineering and Manufacturing-Green Technology, 1(3), 223-228.

[78] Frazier, W. E. (2014). Metal additive manufacturing: a review. Journal of Materials Engineering and Performance, 23(6), 1917-1928.

[79] Mani, M., Feng, S., Lane, B., Donmez, A., Moylan, S., & Fesperman, R. (2015). Measurement science needs for real-time control of additive manufacturing powder bed fusion processes.

[80] Technologies, A. C. F. o. A. M., & Terminology, A. C. F. o. A. M. T. S. F. o. (2012). Standard terminology for additive manufacturing technologies: ASTM International.

[81] Bourell, D., Stucker, B., Barua, S., Sparks, T., & Liou, F. (2011). Development of low-cost imaging system for laser metal deposition processes. Rapid Prototyping Journal.

[82] Barua, S., Liou, F., Newkirk, J., & Sparks, T. (2014). Vision-based defect detection in laser metal deposition process. Rapid Prototyping Journal.

[83] Zenzinger, G., Bamberg, J., Ladewig, A., Hess, T., Henkel, B., & Satzger, W. (2015). Process monitoring of additive manufacturing by using optical tomography. Paper presented at the AIP Conference Proceedings.

[84] Iravani-Tabrizipour, M., & Toyserkani, E. (2007). An image-based feature tracking algorithm for real-time measurement of clad height. Machine Vision and Applications, 18(6), 343-354.

[85] Sames, W. J., List, F., Pannala, S., Dehoff, R. R., & Babu, S. S. (2016). The metallurgy and processing science of metal additive manufacturing. International Materials Reviews, 61(5), 315-360.

[86] Peter, B. (2015). Development in additive manufacturing for high temperature alloys, challenges across complete reduce risk, accelerate advanced technologies while reducing. Paper presented at the DOE/NETL Crosscutting Research Program Annual Review Meeting 2015, Oak Ridge National Laboratory.

[87] Dehoff, R. (2015). In-situ process monitoring and big data analysis for additive manufacturing of Ti-6Al-4V. Titanum 2015.

[88] Margetan, F. J. (2012). Bruce Thompson: Adventures and advances in ultrasonic backscatter. Paper presented at the AIP Conference Proceedings.

[89] Taheri, H., Ladd, K. M., Delfanian, F., & Du, J. (2014). Phased array ultrasonic technique parametric evaluation for composite materials. Paper presented at the ASME 2014 International Mechanical Engineering Congress and Exposition.

[90] Ciliberto, A., Cavaccini, G., Salvetti, O., Chimenti, M., Azzarelli, L., Bison, P., Grinzato, E. (2002). Porosity detection in composite aeronautical structures. Infrared physics & technology, 43(3-5), 139-143.

[91] Cerniglia, D., Scafidi, M., Pantano, A., & Rudlin, J. (2015). Inspection of additive-manufactured layered components. Ultrasonics, 62, 292-298.

[92] Rogé, B., Fahr, A., Giguere, J., & McRae, K. (2003). Nondestructive measurement of porosity in thermal barrier coatings. Journal of thermal spray technology, 12(4), 530-535.

[93] Du, J., Taheri, H., & Delfanian, F. (2013). Wireless Eddy current system prototype for nondestructive testing. Paper presented at the ASNT Annual Conference 2013.

[94] O'brien, R., & James, W. (1988). A review of nondestructive testing methods and their applicability to powder metallurgy processing. Paper presented at the MPIF Seminar on Prevention and Detection of Cracks in Ferrous P/M Pads, International Powder Metallurgy Conference and Exhibition.

[95] Bond, L., Gray, J., Margetan, F., Utrata, D., & Anderson, I. (2014). NDE for adding value to materials from metal powder processing. Advances in Powder Metallurgy and Particulate Materials, 1944-1959.

[96] Du Plessis, A., le Roux, S. G., Els, J., Booysen, G., & Blaine, D. C. (2015). Application of microCT to the non-destructive testing of an additive manufactured titanium component. Case Studies in Nondestructive Testing and Evaluation, 4, 1-7.

[97] Siddique, S., Imran, M., Rauer, M., Kaloudis, M., Wycisk, E., Emmelmann, C., & Walther, F. (2015). Computed tomography for characterization of fatigue performance of selective laser melted parts. Materials & Design, 83, 661-669.

[98] Fowler, R. M. (2012). Investigation of compliant space mechanisms with application to the design of a large-displacement monolithic compliant rotational hinge.

[99] Oya, N., & Hamada, H. (1996). Effects of reinforcing fibre properties on various mechanical behaviors of unidirectional carbon/epoxy laminates. Science and Engineering of Composite Materials, 5(3-4), 105-130.

[100] Oya, N., & Johnson, D. J. (2001). Longitudinal compressive behaviour and microstructure of PAN-based carbon fibres. Carbon, 39(5), 635-645.

[101] Shioya, M., & Nakatani, M. (2000). Compressive strengths of single carbon fibres and composite strands. Composites science and technology, 60(2), 219-229.

[102] Davies, I. J. (2008a). Flexural failure of unidirectional hybrid fibre-reinforced polymer (FRP) composites containing different grades of glass fibre. Paper presented at the Advanced Materials Research.

[103] Davies, I. J. (2008b). Influence of compressive pressure, vacuum pressure, and holding temperature applied during autoclave curing on the microstructure of unidirectional CFRP composites. Paper presented at the Advanced Materials Research.

[104] Kretsis, G. (1987). A review of the tensile, compressive, flexural and shear properties of hybrid fibre-reinforced plastics. Composites, 18(1), 13-23.

[105] Sudarisman, d. S. M. B., & Davies, I. (2009). The effect of partial substitution of E-glass fibre for carbon fibre on the mechanical properties of CFRP composites. Paper presented at the Proceedings of the international conference on materials and metallurgical technology.

[106] Kalnin, I. (1972). Evaluation of unidirectional glass-graphite fiber/epoxy resin composites. Paper presented at the Composite Materials: Testing and Design (Second Conference).

[107] Sudarisman, d. S. M. B., & Davies, I. (2009). The effect of partial substitution of E-glass fibre for carbon fibre on the mechanical properties of CFRP composites. Paper presented at the Proceedings of the international conference on materials and metallurgical technology.

[108] Dong, C., & Davies, I. J. (2013). Flexural properties of glass and carbon fiber reinforced epoxy hybrid composites. Proceedings of the Institution of Mechanical Engineers, Part L: Journal of Materials: Design and Applications, 227(4), 308-317.

[109] Qaiser, Z., Kang, L., & Johnson, S. (2017). Design of a bioinspired tunable stiffness robotic foot. Mechanism and Machine Theory, 110, 1-15.

[110] Liu, Y., Matsuhisa, H., & Utsuno, H. (2008). Semi-active vibration isolation system with variable stiffness and damping control. Journal of sound and vibration, 313(1-2), 16-28.

[111] Fan, X., Zhu, L., Wang, K., Wang, B., Wu, Y., Xie, W., & Du, Y. (2017). Stiffness-controlled thermoresponsive hydrogels for cell harvesting with sustained mechanical memory. Advanced healthcare materials, 6(5), 1601152.

[112] Cheng, N. G., Lobovsky, M. B., Keating, S. J., Setapen, A. M., Gero, K. I., Hosoi, A. E., & Iagnemma, K. D. (2012). Design and analysis of a robust, low-cost, highly articulated manipulator enabled by jamming of granular media. Paper presented at the 2012 IEEE International Conference on Robotics and Automation.

[113] McEvoy, M. A., & Correll, N. (2015). Thermoplastic variable stiffness composites with embedded, networked sensing, actuation, and control. Journal of Composite Materials, 49(15), 1799-1808.

[114] Blanc, L., Delchambre, A., & Lambert, P. (2017). Flexible medical devices: review of controllable stiffness solutions. Paper presented at the Actuators.

[115] Tan, N., Clévy, C., & Chaillet, N. (2013). Calibration of single-axis nanopositioning cell subjected to thermal disturbance. Paper presented at the 2013 IEEE International Conference on Robotics and Automation.

[116] Lubrano, E., & Clavel, R. (2008). Thermal behavior of an ultra-high-precision linear axis operating in industrial environment. Paper presented at the REM 2008 9th International Workshop on Research and Education in Mechatronics.

[117] Chen, J., Yuan, J., & Ni, J. (1996). Thermal error modelling for real-time error compensation. The International Journal of Advanced Manufacturing Technology, 12(4), 266-275.

[118] Tan, N., Clévy, C., & Chaillet, N. (2015). Calibration of nanopositioning stages. Micromachines, 6(12), 1856-1875.

[119] Lee, C., Lee, S.-K., & Tarbutton, J. (2015). Long-term positioning effectiveness of additive manufactured-monolithic double compound notch type flexure stage. Paper presented at the Proceedings of American Society for Precision Engineering 2015 Topical Meeting, Raleigh NC, USA.

[120] Salapaka, S., Sebastian, A., Cleveland, J. P., & Salapaka, M. V. (2002). High bandwidth nano-positioner: A robust control approach. Review of scientific instruments, 73(9), 3232-3241.

[121] Parmar, G., Barton, K., & Awtar, S. (2014). Large dynamic range nanopositioning using iterative learning control. Precision engineering, 38(1), 48-56.

[122] Liu, X., Wu, Y., Zhang, Y., & Xiao, S. (2014). A control method to make LQR robust: A planes cluster approaching mode. International Journal of Control, Automation and Systems, 12(2), 302-308.

[123] Chun, H., Han, J., Wright, L., Elwany, A., Villarraga-Gómez, H., & Lee, C. (2020). Pressure-fed mechanism to compensate for motions and dynamic characteristics of compliant nanopositioning stages. Precision Engineering, 63, 33-40.

[124] Li, B., Li, Z., Xiong, J., Xing, L., Wang, D., & Li, Y. (2006). Laser welding of Zr45Cu48Al7 bulk glassy alloy. Journal of Alloys and Compounds, 413(1-2), 118-121.

[125] Wang, G., Huang, Y., Shagiev, M., & Shen, J. (2012). Laser welding of Ti40Zr25Ni3Cu12Be20 bulk metallic glass. Materials Science and Engineering: A, 541, 33-37.

[126] Kawahito, Y., Terajima, T., Kimura, H., Kuroda, T., Nakata, K., Katayama, S., & Inoue, A. (2008). High-power fiber laser welding and its application to metallic glass Zr55Al10Ni5Cu30. Materials Science and Engineering: B, 148(1-3), 105-109.

[127] Chen, B., Shi, T., Li, M., Yang, F., Yan, F., & Liao, G. (2014). Laser welding of annealed Zr55Cu30Ni5Al10 bulk metallic glass. Intermetallics, 46, 111-117.

[128] Chen, B., Shi, T., Li, M., Zhang, Z., Zhu, Z., & Liao, G. (2013). Laser welding of Zr41Ti14Cu12Ni10Be23 bulk metallic glass: experiment and temperature field simulation. Advanced Engineering Materials, 15(5), 407-413.

[129] Hofmann, D. C., Kolodziejska, J., Roberts, S., Otis, R., Dillon, R. P., Suh, J.-O., Borgonia, J.-P. (2014). Compositionally graded metals: A new frontier of additive manufacturing. Journal of Materials Research, 29(17), 1899-1910.

[130] Duwez, P., & Lin, S. (1967). Amorphous ferromagnetic phase in iron-carbon-phosphorus alloys. Journal of applied physics, 38(10), 4096-4097.

[131] Yamauchi, K., & Nakagawa, Y. (1971). Amorphous ferromagnetic Fe-PB alloys prepared by a new technique of splat cooling. Japanese Journal of Applied Physics, 10(12), 1730.

[132] Kikuchi, M., Fujimori, H., Obi, Y., & Masumoto, T. (1975). New amorphous ferromagnets with low coercive force. Japanese Journal of Applied Physics, 14(7), 1077.

[133] Inoue, A., Kobayashi, K., & Masumoto, T. (1980). Mechanical Properties and Thermal Stability of (Fe, Co, Ni)-Mo-C Quaternary Amorphous Alloys. Science reports of the Research Institutes, Tohoku University. Ser. A, Physics, chemistry and metallurgy, 28(2), 172-181.

[134] Inoue, A., Kobayashi, K., Kanehira, J., & Masumoto, T. (1980). Mechanical Properties and Thermal Stability of (Fe, Co, Ni)-MB (M= IV, V and VI Group Transition Metals) Amorphous Alloys with Low Boron Concentration. Science reports of the Research Institutes, Tohoku University. Ser. A, Physics, chemistry and metallurgy, 29, 331-342.

[135] Magnetic amorphous metal alloys (1982), US4321090.

[136] Kruth, J.-P., Mercelis, P., Van Vaerenbergh, J., & Craeghs, T. (2007). Feedback control of selective laser melting. Paper presented at the Proceedings of the 3rd international conference on advanced research in virtual and rapid prototyping.

[137] Chivel, Y. (2013). Optical in-process temperature monitoring of selective laser melting. Physics Procedia, 41, 904-910.

[138] Furumoto, T., Alkahari, M. R., Ueda, T., Aziz, M. S. A., & Hosokawa, A. (2012). Monitoring of laser consolidation process of metal powder with high speed video camera. Physics Procedia, 39, 760-766.

[139] Alkahari, M. R., Furumoto, T., Ueda, T., & Hosokawa, A. (2014). Melt pool and single track formation in selective laser sintering/selective laser melting. Paper presented at the Advanced Materials Research.

[140] Granato, A. v., & Lücke, K. (1956). Theory of mechanical damping due to dislocations. Journal of applied physics, 27(6), 583-593.

[141] Bellouard, Y. (2011). On the bending strength of fused silica flexures fabricated by ultrafast lasers. Optical Materials Express, 1(5), 816-831.

3. PRESSURE-FED MECHANISM TO COMPENSATE FOR MOTIONS AND DYNAMIC CHARACTERISTICS OF COMPLIANT NANOPOSITIONING STAGES[*]

3.1. Overview

This paper introduces a novel pressure-fed mechanism that can correct or compensate for motions and dynamic behavior and characteristics of compliant mechanism-based nanopositioning stages. The nanopositioning stages with double compound spring structures are typically bilaterally symmetric. However, due to themanufacturing tolerances and actuator-stage alignment errors, stiffness or damping characteristics of bilaterally symmetric spring structures could be different. Such results lead to motion error and a shift in the natural frequency of the system, and can adversely affect nanopositioning performance. The novel pressure-fed mechanism proposed here could solve such problems. The monolithic nanopositioning stage made of Stainless Steel was fabricated by metal 3D printing process, and the internal fluidic channels inside the spring structures were designed to apply pneumatic pressure to each channel. The pressure-fed mechanism was designed to pneumatically pressurize the internal channels of the nanopositioning stage. By controlling the pneumatic pressure level inside of the internal fluidic channels, the linear motion, yaw motion, stiffness, damping, natural frequency and positioning behavior of the additively manufactured nanopositioning stage

---

were experimentally characterized. As a result, the proposed pressure-fed mechanism could control yaw motion and natural frequency of the system by changing the air pressure within the two fluidic channels.

3.2. Preface

The basic principles of compliant mechanisms have been known for a few decades, and the design and fabrication methods that can be found in the literature have been well documented in textbooks [1-3]. This research has been driven by the increasing need for nanometer motion accuracies and the efforts to achieve high precision in many semiconductor, machine tool, automotive and aerospace industries.

Most of the nanopositioning systems adopt compliant mechanisms, and are used in high precision instruments, as they can provide nanometer-scale motions with a total range of at least tens of microns. When the actuation force acts on the mechanism, the bearing structures are deformed to produce the desired displacement. In general, compliant mechanisms are monolithically-manufactured and therefore prevent assembly errors. The monolithic construction also implies a relatively easy manufacturing process and a potentially compact design. Electric discharge machining [4] (accuracy ~2.5 µm), waterjet machining [5] (accuracy ~ 25 µm), micromilling [6] (accuracy ~2 µm) and polymeric/metallic additive manufacturing (AM) [7-12] (accuracy 50~200 µm) are the most common manufacturing methods for compliant mechanisms. However, their part accuracy or manufacturing tolerance (width, height, total length, and sometimes roughness) realistically increase in most cases due to complex geometries such as hinges, or machining compliance issues [13, 14] in the case of machining thin slabs. In compliant

mechanisms that are typically bilaterally symmetric, such part accuracy errors challenge the stiffness or damping design of the bilateral symmetric spring structures, as it results in motion error and changes in the natural frequency of the system. Since compliant mechanisms are commonly used in mechanical systems requiring high precision and accuracy, such as atomic force microscopy or fast tool servos, part accuracy errors are not acceptable. In addition to the manufacturing tolerance, in many cases, part accuracy errors, combined with actuator-compliant mechanism alignment errors or contact errors [15, 16], will ultimately affect positioning performance. For example, the stiffness, k, of a rectangular cross-section cantilever [16] can be expressed as its geometric parameters $k = (¼)(bh^3/L^3)(E)$. It can be seen from the expression that k is linearly proportional to the base width b and Young's modulus E, and it strongly depends on the third power of the ratio (height/length) or (h/L). Therefore, in designing a flexure, one can "grossly tune" the stiffness by varying the ratio (h/L), or one can "fine-tune" the stiffness by varying the base width b. However, it is only valid if there exist no manufacturing error. Since the part machining accuracy error can occur 3-dimensionally within the manufacturing tolerance ranges, the variation of the part stiffness is unavoidable and unpredictable.

Many studies identifying such errors and measuring the effects (e.g., motion error, cross-talk error, positioning accuracy, and resolution) [2, 9, 10] have been reported, but error compensation methods were not well introduced. Most of the studies were stiffness model-based [17-21]. Since these approaches require an update or correction to the model according to the input changes or environmental conditions, they cannot be considered as ultimate solutions. Therefore, there is no method to physically correct these errors,

70

providing the convenience of real-time tuning the dynamic parameters of the compliant mechanisms.

This study introduces pressure-fed mechanism through hollow-type spring structures, to overcome these challenges. The monolithic compliant mechanisms made of Stainless Steel is fabricated by metal 3D printing process, and the internal fluidic channels inside the spring structures are designed to apply pneumatic pressure to each channel. The pressure-fed mechanism can correct or compensate for motion error of the compliant mechanism by pneumatically pressurizing the internal channels. Here, by controlling the pneumatic pressure level and flow direction inside the internal fluidic channels, the linear motion, yaw motion, stiffness, damping, natural frequency, and positioning precision of the compliant mechanism are analyzed.

3.3. Method

Dynamic characteristics of compliant mechanisms are highly dependent on material constitutive properties, geometric compatibility, or force equilibrium conditions. Unlike conventional manufacturing methods such as electric discharge machining, waterjet machining, and micro milling, an AM technology that makes use of mechanical design flexibility can effectively control the material distribution (channel size, shape, and placement) in terms of stiffness, damping, and natural frequency. Also, AM methods can fundamentally change the current design principles to improve performance, such as accuracy, precision, repeatability, or removing motion error at a low-cost.

In this study, as shown in Figure 3.1 (a), the internal fluidic channels in the spring structures of the compliant mechanism are designed to allow for pressure variation within

71

the structure. The pressure distribution can be monitored from four pressure gauges installed in inlets and outlets. As discussed in Section 3.2, the stiffness ($k_{X,L}$, $k_{X,R}$) and damping ($c_{X,L}$, $c_{X,R}$) may be different due to AM tolerance as seen in Figure 3.1 (b), and the displacement $\delta_{X,L}$ and $\delta_{X,R}$ may be different when the force (F) is applied to the shuttle, which will cause yaw error depending on the two displacement amplitudes. In addition to the stiffness mismatching, the force (F) applied to the shuttle part may not be aligned with the principal direction of the compliant mechanism as seen in Figure 3.1 (c). Since bilateral spring structures are monolithically connected and there are force-displacement interactions between each spring structure, it is difficult to estimate or even measure the dynamic parameters (stiffness and damping) independently. It is rather convenient to measure the motion error of complaint mechanisms. The proposed pressure-fed mechanism can independently control bilateral spring structures, and the pressure can be in-situ adjusted depending on the linear motion results to make this displacement $\delta_{X,L}$ equal to the displacement $\delta_{X,R}$. In addition, it can assist the actuator to push and pull the shuttle.
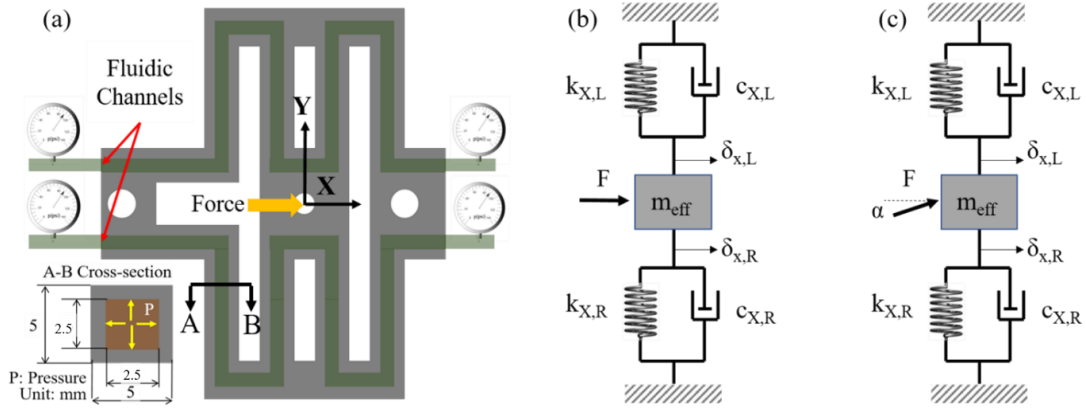
Figure 3.1. Operating principle of the proposed pressure-fed mechanism: (a) schematic description, (b) dynamic model and (c) dynamic model when the force is not applied along the principal direction.

3.4. Characterization

Since the proposed compliant mechanism was additively manufactured (metal power bed), the AM Stainless Steel material, here denoted as AM SS, was characterized and compared with the baseline comparison of bulk SS material properties. Three comparison tests were conducted in this study.

X-ray powder diffraction (XRD), which is primarily used for phase identification of a crystalline material, was used to determine the bulk material composition. As seen in Figure 3.2, the material compositions of the bulk SS and the AM SS were found identical because the sharp intensity peaks were found at the same angles. This result indicates that additively manufactured compliant mechanisms can be designed the way conventional compliant mechanisms are designed.
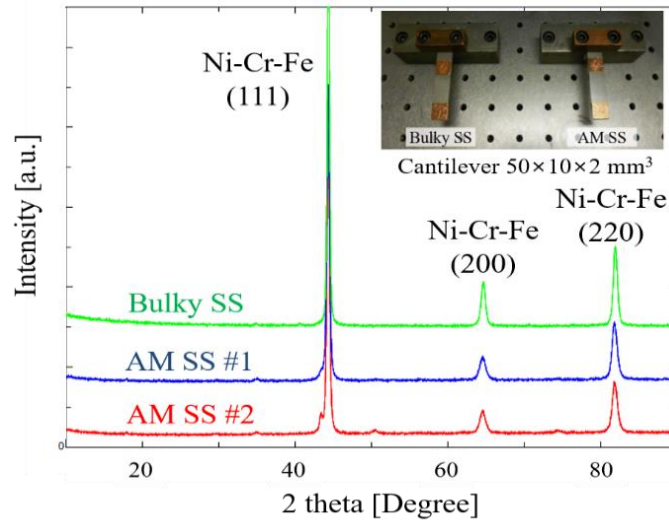
Figure 3.2. XRD pattern results: the bulk SS and AM SS samples.

The void analysis of the two samples above was performed by an industrial CT scan that can detect internal features and flaws such as porosity, inclusion or crack, displaying this information in 3-dimension [9]. As seen in Figure 3.3, the void size of the bulk SS sample was uniform, approximately 3,000 μm^3. On the other hand, the void size of the AM SS sample was irregularly distributed up to 120,000 $\mu m^{3,}$ the peak count amounting up to 15.000 $\mu m^{3.}$ Since the AM SS sample was layer-by-layer printed, there exist air voids between metal powders. As a result of the void sizes and their distribution of the AM SS sample, it is, however, difficult to draw a conclusion that the AM materials and the fabricated parts are not adaptable to compliant mechanisms. Although the AM SS material is less homogeneous than the bulk SS part, it could be attractive to the designers of the compliant mechanisms if it meets its requirements in dynamic aspects.

74
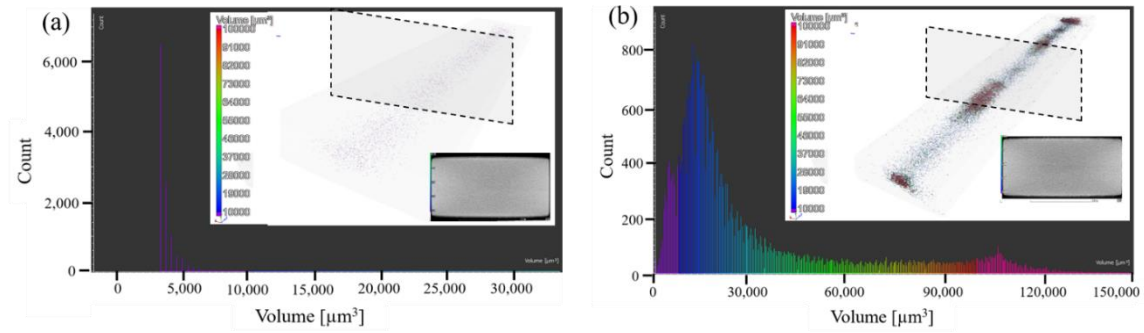
Figure 3.3. Void analysis results of (a) bulk SS and (b) AM SS samples by industrial CT scan.

The dynamic characteristics such as the natural frequency and damping coefficient are key parameters for compliant mechanisms. As seen in Figure 3.4, the natural frequency ω_n and damping coefficient ξ of the bulk SS and AM SS samples were obtained from the free vibration test that measures the displacement while applying an impact at the tip of each cantilever. The capacitive sensor (Lion Precision, 15 kHz bandwidth, 10 nm resolution) was used to measure the oscillation signal of each cantilever. To equally compare the outputs of free vibration test, the dimensions of the AM SS sample were measured and the bulk SS sample was machined to have the same width, height, and length. The Vernier calipers with 1 µm reading resolution was used to control the dimensions of two samples. As a result, there existed approximately 1% discrepancy in the natural frequency, and the damping coefficients of the two samples ranged from 0.005 to 0.01. The natural frequency was estimated by taking the reciprocal of the oscillation period and the damping coefficient was calculated by using a logarithmic decrement method.
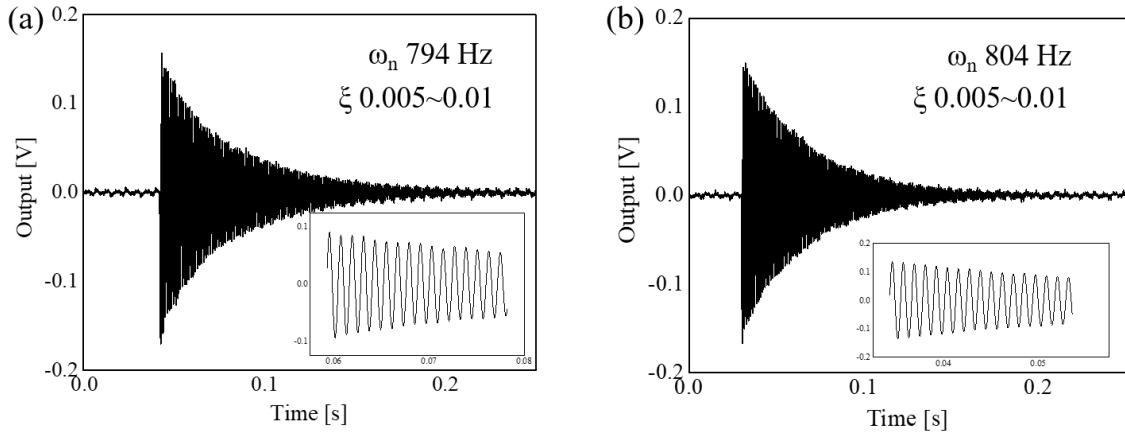
Figure 3.4. Free vibration test results: (a) bulk SS sample and (b) AM SS sample.

3.5. Experiments

The double compound-type compliant mechanism, the so-called nanopositioning stage, was designed and fabricated with spring structures (width 5 mm, height 5 mm, length 40 mm). The printed mechanism was scanned by the industrial CT scanner, and its cross-sectional channel areas (2.5 mm × 2.5 mm) were visualized as shown in Figure 3.5. Due to the metal AM tool tolerance (1 mm), the wall thickness is maintained as 1.25 mm, in consideration of compressed air-filled pressure condition. The internal fluidic channels were formed as designed, but there existed surface integrity issues, especially on the bottom surface of the channel. It was considered as printing tolerance, which is beyond the scope of this research.
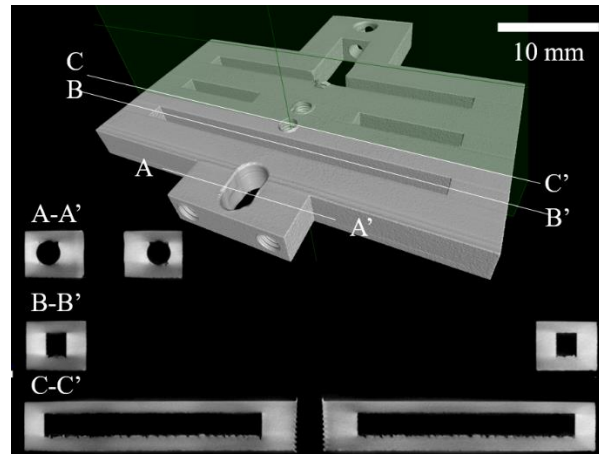
Figure 3.5. Cross-sectional images by CT scan.

Prior to the experiment, the finite element model was developed. The 3D model of the compliant mechanism was drawn by SolidWorks, and then, was exported to the commercial structural analysis package, ANSYS. As shown in Figure 3.6 (a), the stiffness of pressure-fed compliant mechanisms was estimated approximately 5.18 kN/mm from finite element analysis (FEA), and was also measured 4.99 kN/mm by using a force sensor and capacitive sensor (CS). There existed approximately 3% discrepancy between the FEA results and experiment results. In addition, the natural frequency and damping ratio of the compliant mechanism was found 2,520 Hz and 0.004 from the free vibration experiment, and the vibration mode of FEA model at 2,590 Hz was obtained as shown in Figure 3.6 (b).
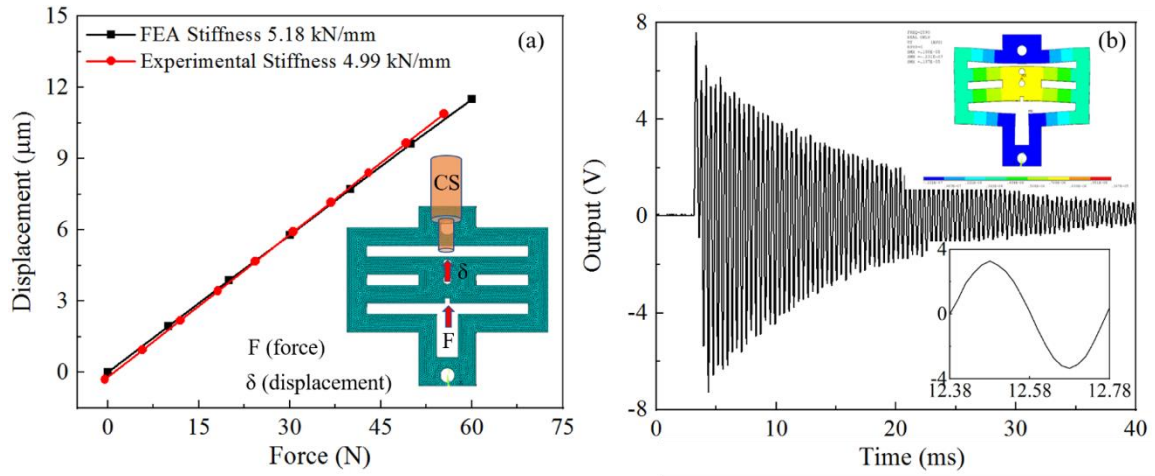
Figure 3.6. Stiffness curves of pressure-fed compliant mechanisms.

The internal fluidic channels (2.5 mm × 2.5 mm) were incorporated to apply a pressure distribution (P) inside the structure. The entire stage was 3D printed with metal and is shown in Figure 3.7. The pneumatic lines were connected to the fluidic channels, the pressure gauges were installed in each pneumatic line, and the two CS were placed near the measurement target installed on the shuttle. Here the two CS placed in the left and right sides were denoted as L_CS and R_CS. The stack-type piezoelectric (PZT) actuator was inserted between the shuttle and the ground parts, and was controlled by a PZT driver.
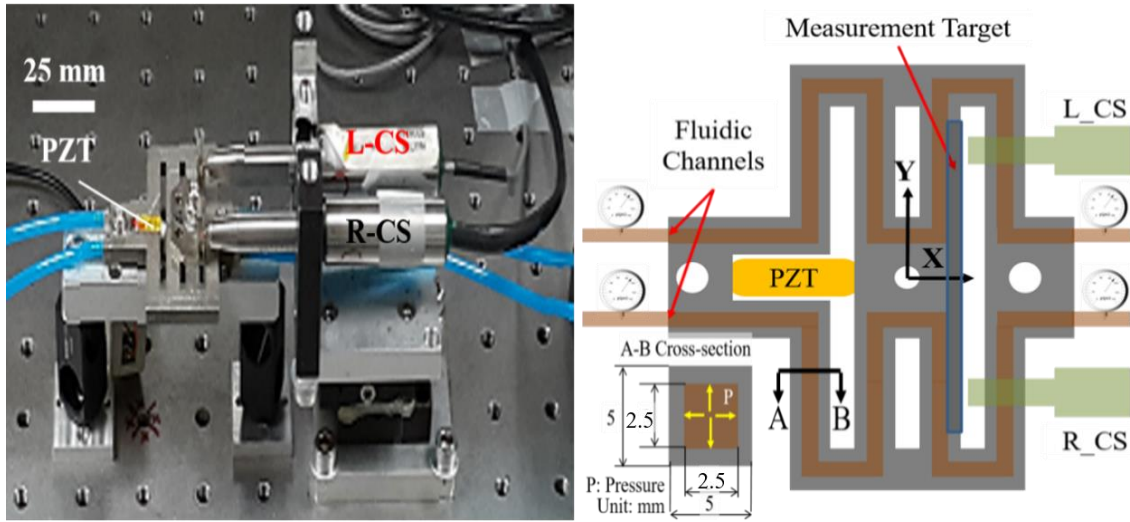
Figure 3.7. Experimental setup.

As a result, the two CS showed identical responses to the PZT input voltages under the ambient condition, and the displacement increased as the PZT input voltage increased as shown in Figure 3.8. In this test, the DC 30V was given to the PZT actuator as an offset voltage.
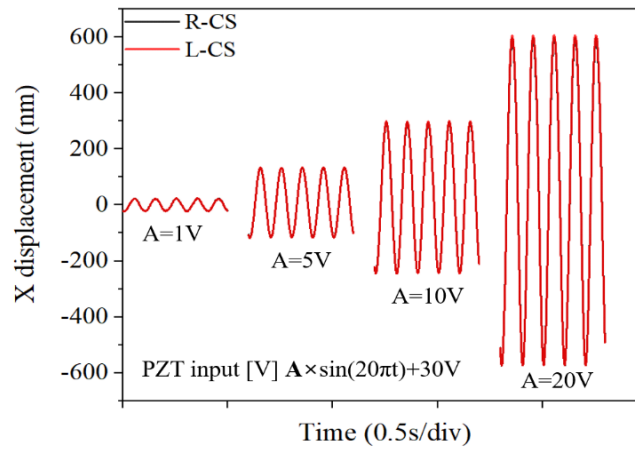
Figure 3.8. Displacement measurement results according to PZT input voltages.

Since the concept of pressure-fed mechanism is to compensate for the manufacturing tolerance-induced discrepancy in dynamic characteristics of the compliant mechanisms, it would be limited to visualize the increase of the structural stiffness by the pressure-fed mechanism. As seen in Figure 3.9, the CS outputs were collected under pressure-fed conditions (compressed air pressure and direction) according to the PZT input voltages. Here the displacement can be obtained from the ratio of stiffness of compressed air in the channels, PZT actuator and compliant mechanisms and the applying force. Therefore, the direction comparison with the results (Figure 3.9 (a)) would be difficult with the PZT actuator's stiffness unknown. This study primarily focused on the characterization of pressure-fed compliant mechanisms. Overall, the CS outputs linearly increased as the PZT input voltage increased. Compared to the two CS outputs collected under the ambient condition, those collected under 80 psi conditions at both channels increased approximately 3~4% although the same PZT input voltages were applied. The CS outputs measured under the pressure-fed condition applied to only one channel, either way, were too small to make a clear difference from those results obtained under the ambient condition. Assuming that the PZT input voltage is proportional to the force applied to the shuttle, the stiffness was estimated. These results indicate that pressure-fed mechanism can slightly increase structural stiffness.
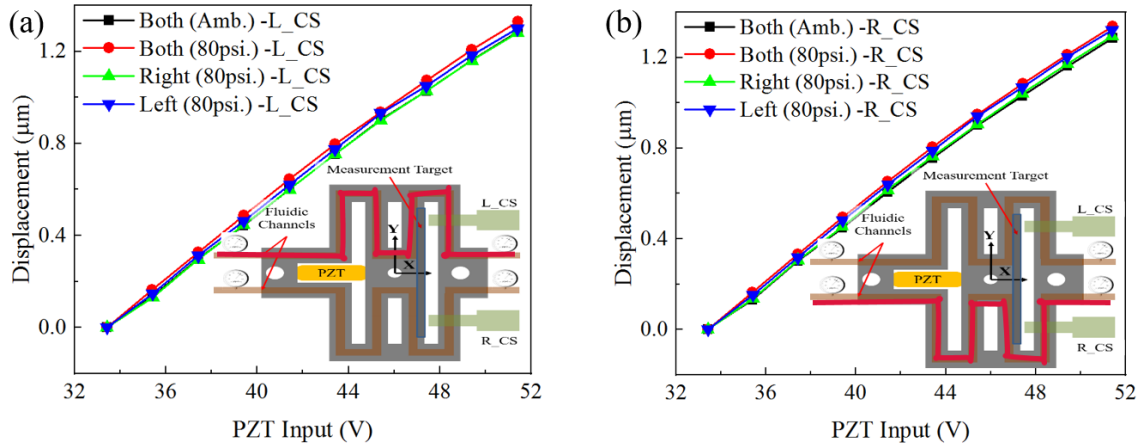
Figure 3.9. Displacement measurement results according to PZT input voltages under pressure-fed conditions: (a) L_CS outputs and (b) R_CS outputs under pressure-fed conditions.

3.6. Results

The effectiveness of the pressure-fed mechanism was tested by reading the two CS outputs with respect to the two compressed air pressure conditions, 50 psi, and 80 psi. The internal structure was pressurized by closing the valves at the outlet of the channel while regulating the pressure into the channel. Therefore, the air pressure could be set at a constant value of 50 psi or 80 psi. Since the PZT actuator can affect the fundamental characteristics of the compliant mechanism, the PZT actuator was removed from the compliant mechanism. In a similar way, as detailed in the previous section, the two CS outputs were collected under various pressure conditions and pressure-fed directions as seen in Figure 3.10. The condition (L, R) indicates the pressure-fed conditions in the left (L) and right (R) channels, that is, the condition (0, 0) indicates the ambient condition in both left and right channels, and the condition (B, F) indicates the pressure-fed condition

81

when the compressed air pressure difference is applied backward in the left channel and is applied forward in the right channel. The initial position information of the compliant mechanism was set to zero because there was no actuator to move the shuttle. The displacement information obtained under a few pressure-fed conditions was compared with the initial position information. From the experiment results, the pressure-fed mechanism could move the shuttle up to 50 nm range at 50 psi condition (Figure 3.10 (a)) and up to 100 nm range at 80 psi condition (Figure 3.10 (b)). Also, the displacement of the spring structures in the left and the right side could be adjusted by controlling the pressure level and pressure-fed direction. More interestingly, the angular displacement (Figure 3.10 (c) and (d)), yaw motion, could be calculated by dividing the difference of the two CS outputs with the distance of two CS (here approximately 20 mm). The two angular displacements according to the pressure conditions showed a similar trend as shown in Figure 3.10 (a) and (b). Yaw motions increased in a higher pressure condition. This result showed that pressure-fed mechanism can effectively control the linear and angular motion of the nanopositioning stage by fine-tuning the stiffness of each spring structure independently.
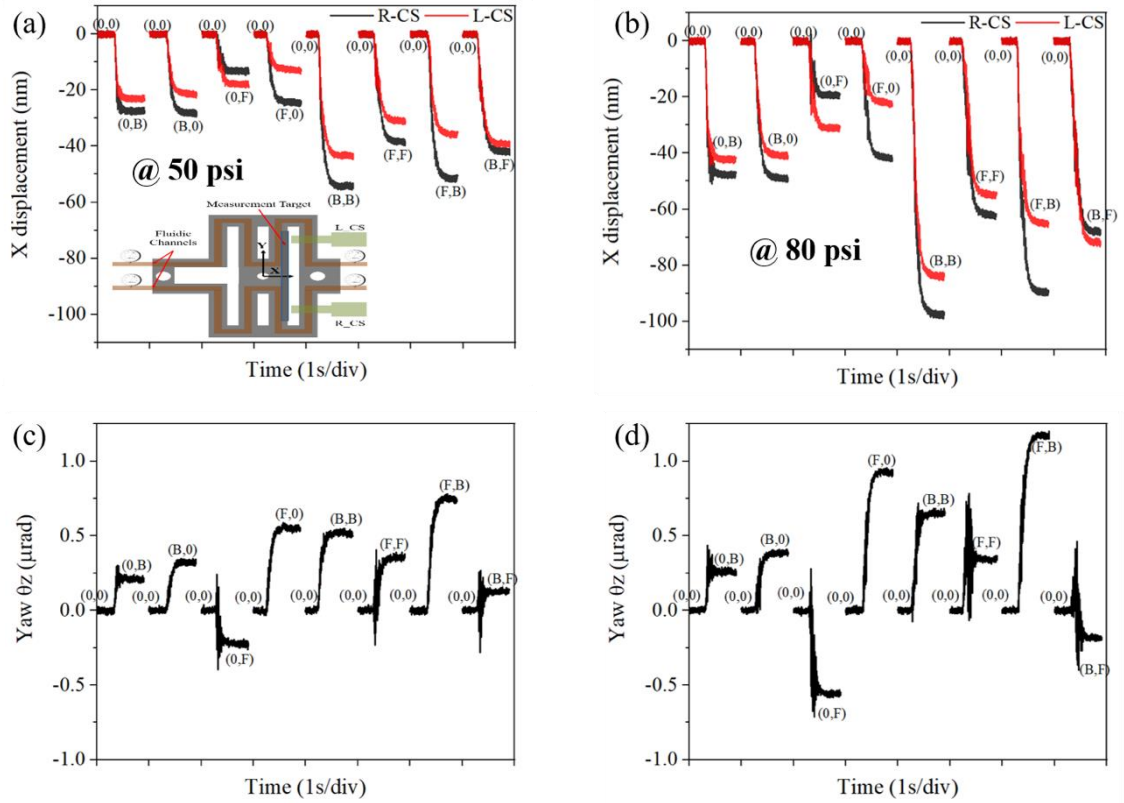
Figure 3.10. Linear and angular displacement measurement results according to pressure-fed conditions.

The PZT actuator was again installed between the shuttle and the ground parts. Binary pulses were applied to the PZT actuator to obtain the step responses of the nanopositioning stage under the pressure-fed direction while measuring the displacement by the two CS. Similar to the previous experiment, the two CS were installed to produce the identical displacement information of the nanopositioning stage at the ambient condition (0, 0). This initial condition was set to the reference for the relative comparison of the nanopositioning stage behavior between the ambient (0 psi) and pressure-fed (80 psi) conditions. As seen in Figure 3.11, four different pressure-fed conditions, (0, 0), (F,

0), (0, F) and (F, F), were tested while moving the stage approximately 40 nm range. The results of (F, 0) and (0, F) conditions showed a similar trend but the displacement directional information is reversed. In Figure 3.11 (b), the right and left sides of the spring structures moved approximately 50 nm and 30 nm in a negative X direction under the condition (F, 0). On the other hand, the right and left spring structures under the condition (0, F) moved opposite to the case of condition (F, 0) as exact as it was moved. Also, at the condition (F, F), the stage moved approximately 80 nm toward the PZT actuator, and there was no difference in the two CS outputs.
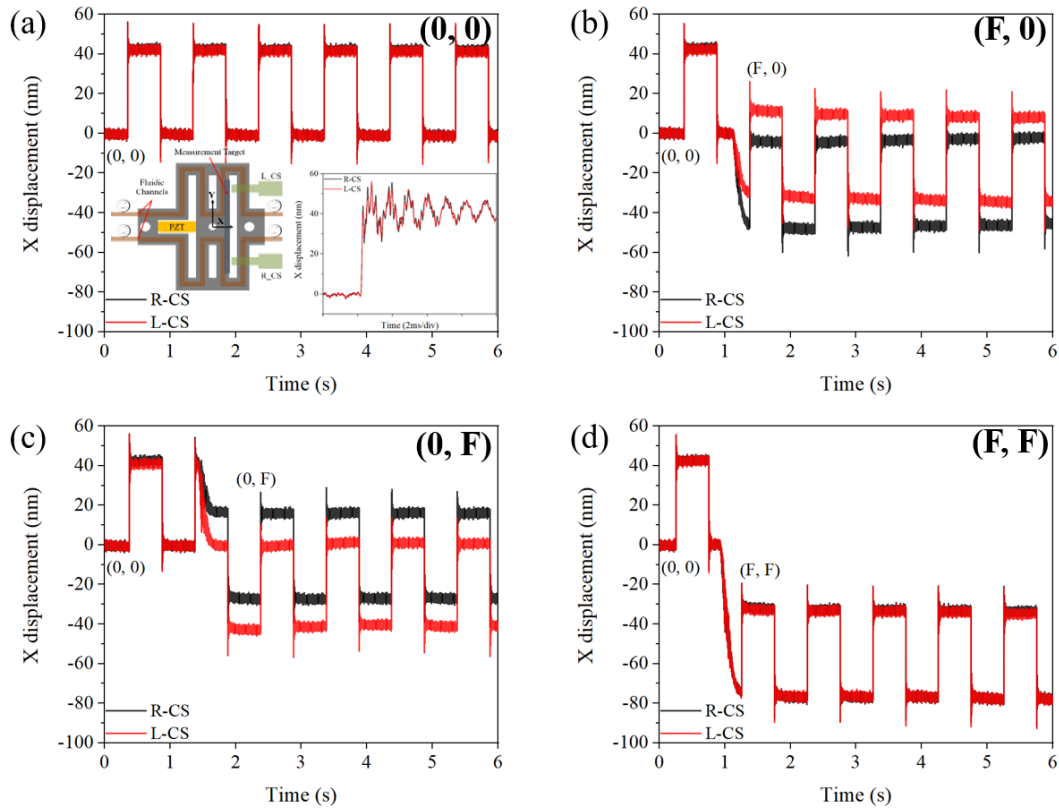
Figure 3.11. Linear displacement results of the step responses according to pressure-fed conditions.

More interestingly, the angular displacement of the step responses under pressure-fed conditions was calculated by dividing the difference of the two CS outputs (Figure 3.11) with the distance of the two CS. As seen in Figure 3.12, yaw motion could be bi-directionally controlled approximately 0.8 μrad according to the pressure condition (0 and 80 psi) and pressure-fed direction. The signal spikes were considered due to the slight difference in the sensitivity of the two CS.
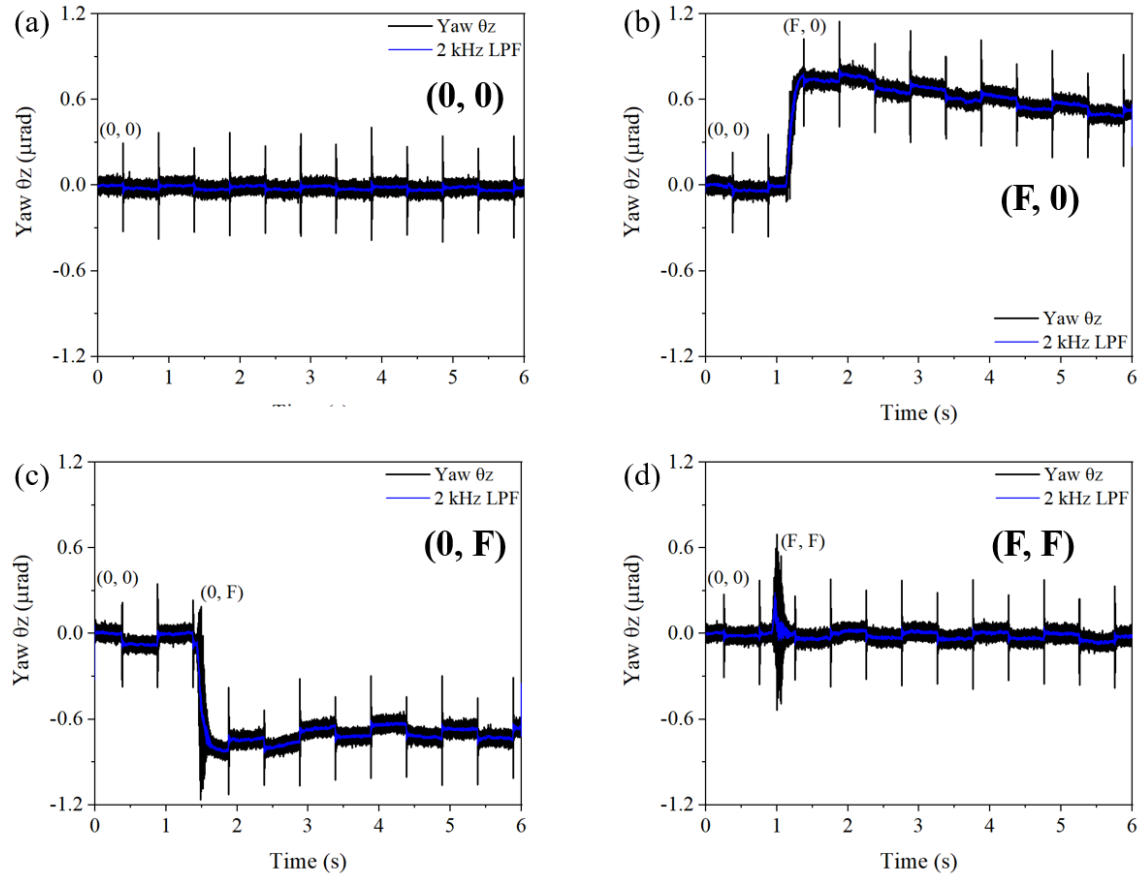
Figure 3.12. Angular displacement results of the step responses according to pressure-fed conditions.

In addition to the motion control of the pressure-fed mechanism, the impulse hammering test with a dynamic signal analyzer (DSA) was conducted and the Bode plots were obtained according to the pressure-fed conditions. It is obvious that the natural frequency peak shifts to higher bandwidth because the stiffness increases when the preload is applied to the mechanical system. Similarly, the pressure-fed mechanism can produce the DC offset displacements (Figure 3.11) and can slightly increase the stiffness of the compliance mechanism (Figure 3.9), which means that the pressure-fed mechanism can effectively control the natural frequency shift. From Figure 3.13, the frequency peak of the compliant mechanism was shifted from 936 Hz to 952 Hz when each spring structure was pressure-fed. Also, a few more peaks were shifted a few tens of Hz. The 1st peak was considered as a natural frequency of PZT actuator and the later peaks were from the compliant mechanisms. This result indicates that pressure-fed mechanism can control fundamental behaviors of dynamic systems; hence this method can be used to compensate for errors and to tune the dynamic characteristics of the compliant mechanisms in real-time.
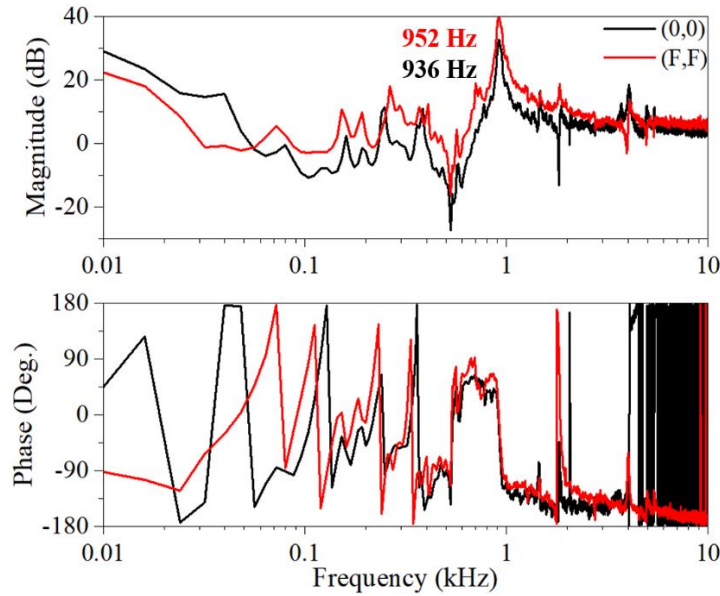
Figure 3.13. Dynamic system responses of the compliant mechanism under conditions (0, 0) and (F, F).

3.7. Summary

The pressure-fed mechanism was experimentally validated with the double compound compliant nanopositioning stage. It showed that the pressure-fed mechanism not only compensates for motion errors of the compliant mechanisms but also in-situ tune their dynamic behaviors to be compatible with their applications. According to the shape and arrangement of the internal fluidic channels, fluid types (air, water, oil, mixed fluids) and pressure conditions, the performance of the pressure-fed nanopositioning stages can be significantly improved. Also, the further development of AM processes and materials will accelerate the fundamental approaches to pressure-fed mechanisms for various dynamic motion systems. In future, the pressure-fed mechanism will be tested in the feedback positioning-controlled conditions and at the elevated temperature conditions to

test if this mechanism can effectively compensate for thermal drift. Also, the fluidic

dynamic effects and geometry and surface integrity effects of the fluidic channels will be

investigated to determine the right FEA model for system parameter identification.

3.8. References

[1]   L. Howell, Compliant mechanisms, John Wiley & Sons Inc, 2001.

[2]   S. T. Smith, Flexures, Gordon and Breach Science Publishers, ISBN 90-5699-261-9, 2000.

[3]   S. Henein, Conception des guidages flexibles, Presses Polytechniques et Universitaires Romandes, ISBN 2-88074-481-4, 2001.

[4]   Understanding the wire EDM process, obtained June 24, 2019 from http://www.reliableedm.com/Complete%20EDM%20Handbook/Complete%20EDM%20Handbook_5.pdf

[5]   Waterjet machining tolerance, obtained June 24, 2019 from https://waterjets.org/archive/getting-the-most/tips/waterjet-machining-tolerances/.

[6]   David J. Guckenberger, Theodorus E. de Groot, Alwin M. D. Wan, David J. Beebe, and Edmond W. K. Young, Micromilling: A method for ultra-rapid prototyping of plastic microfluidic devices, Lab Chip, Vol. 15, No. 11, pp. 2364-2378 (2015).

[7]   M. Aliakbari, Additive Manufacturing: State-of-the-Art, Capabilities, and Sample Applications with Cost Analysis, Master of Science Thesis, Department of Industrial Production, KTH, June 2012.

[8]   Valmik Bhavar, Prakash Kattire, Vinaykumar Bapuso Patil, S. M. Khot, Kiran Gujar, Rajkumar Raju Singh, A review on power bed fusion technology of metal additive manufacturing, Additive Manufacturing Handbook DOI:10.1201/9781315119105-15 (2017).

[9]   Herminso Villarraga Gomez, ChaBum Lee, and Stuart T. Smith, Dimensional metrology with X-ray CT: a comparison with CMM measurements on internal features and compliant structures, Precision Engineering, 51, pp. 291-307 (2018).

[10] ChaBum Lee, Christopher K. Stepanick, Sun-Kyu Lee, and Joshua A. Tarbutton, Cross-coupling effect of large range XY nanopositioning stage fabricated by stereolithography process, Precision Engineering, Vol. 46, pp. 81-87 (2016).

[11] ChaBum Lee, Sun-Kyu Lee and Joshua A Tarbutton, Positioning control effectiveness of optical knife edge displacement sensor-embedded monolithic precision stage, Sens. Actuators A. Vol. 233, pp. 390-396 (2015).

[12] ChaBum Lee and Joshua A Tarbutton, Compliance and control characteristics of an additive manufactured-flexure stage, Rev. Sci. Instrum. 86(4) 045107 (2015).

[13] Nuodi Huang, Chunhui Yin, Liang Liang, Jicai Hu, Shijing Wu, Error compensation for machining of large thin-walled part with sculptured surface based on on-machine measurement, The International Journal of Advanced Manufacturing Technology, Vol. 96, Iss. 9-12, pp. 4345-4352 (2018).

[14] Kolluru K, Axinte D, Becker A, A solution for minimizing vibrations in milling of thin walled casings by applying dampers to workpiece surface. CIRP Ann-Manuf Technol., Vo. 62, No. 1, pp. 415–418 (2013).

[15] Thomas R Hicks and Paul D Atherton, The nanopositioning book, Queensgate Instruments Ltd. 1997.

[16] Herman Soemers, Design principles for precision mechanisms, Enschede, the Netherlands: T-Point Print VoF 2010.

[17] R. Brent Gillespie, Taeyoung Shin. Felix Huang, Brian Trease, Automated Characterization and Compensation for a Compliant Mechanism Haptic Device, IEEE/ASME Transactions on Mechatronics, Vol. 13, Iss. 1, pp. 136-146 (2008).

[18] Margaret Koehler, Allison M. Okamura, Christian Duriez, Stiffness control of deformable robots using finite element modeling, Robotics and Automation Letters IEEE, Vol. 4, No. 2, pp. 469-476 (2019).

[19] Mohammad I. Awad, Dongming Gan, Marco Cempini, Mario Cortese, Nicola Vitiello, Jorge Dias, Paolo Dario, Lakmal Seneviratne, Modeling design & characterization of a novel Passive Variable Stiffness Joint (pVSJ), Intelligent Robots and Systems (IROS) 2016 IEEE/RSJ International Conference, pp. 323-329 (2016).

[20] Abolfazl Zolfaghari, Seongkyul Jeon, Christopher K. Stepanick, and ChaBum Lee, A novel sensor for two degree-of-freedom motion measurement of linear nanopositioning stage using knife edge displacement sensing technique, Review of Scientific Instruments, Vol. 88, Iss. 6, 065110 (2017).

[21] S. Henein, Short communication: Flexure delicacies, Mechanical Sciences, Vol. 3, pp. 1-4 (2012).

4. CHARACTERIZATION OF THERMALLY STABLE COMPLIANT STRUCTURES WITH INTERNAL FLUIDIC CHANNELS[*]

4.1. Overview

This paper represents a novel method to suppress the thermal effects of flexure mechanism-based nanopositioning system by fluid (air or water) flow under certain pressure conditions through the internal fluidic channels of the compliant structure. The nanopositioning system made of stainless steel was additively manufactured, and the rectangular fluidic channels were formed on each side of the double compound type flexure mechanism-based compliant structure. The motion behavior was characterized by measuring the stiffness and frequency responses of the compliant structure with the hammering test while filling compressed air or the water through the fluidic channels. The thermal behavior was characterized by measuring the temperature distribution over the compliant structure and thermal displacement under the various compressed air pressure and water flow-rate conditions. Dynamic behaviors of the nanopositioning system under various fluid-fed conditions were also characterized by the Finite Element Method and were validated with experimental results. As a result, the compressed air- or water-fed mechanisms have the following characteristics: (1) the damping may increase when the fluid exists in the channels, (2) the compressed air-fed mechanism can move the stage with

nanometer precision with fast response time, and (3) the media filled in the fluidic channels significantly lower the temperature increase and reduce thermal displacement error. Interestingly, two-fluid flows of the compressed air and water showed a similar tendency in suppressing the temperature increase. The proposed method is expected to meet the increasing needs for nanometer motion accuracies and the efforts achieving high precision in the thermally stable environments requiring from semiconductor industries and precision machine tool industries.

4.2. Preface

In precision engineering, thermal stability of the mechanical, electrical or chemical systems has always been important to keep high accuracies and precision manners [1-4]. Although most of the precision systems such as atomic force microscopes (AFM), scanning electron microscopes (SEM), semiconductor manufacturing systems or precision machine tools are set up and used in vibration-isolated and temperature-controlled environments, precision system performances are still highly dependent on thermal stability because the most of motion mechanisms are driven by motors and motors are generally major heat sources in the precision motion systems [5-7]. In addition to the motors, power consumptions of frictions or laser-based sensors could be also the heat sources in the precision machine systems. Such heat prevents the machine system from achieving high accuracy and precision because the machine frames, guides, feedback sensors, control systems, or the motors themselves are vulnerable to deformation and changes in their dynamic behaviors such as mechanical properties, travel range of motion system, and natural frequency due to the heat source. Although temperature sensors may

directly monitor the temperature changes and may allow the motion controller to compensate for such errors caused by heat, even a relatively small heat source can have a dramatic effect on the stability of precision system and the heat sources are unpredictable in most cases [8-10]. Thus, there still exist needs for improving and maintaining the thermally stable environment for the precision machine systems in convenient, low-cost and reliable ways.

The flexure (or compliant) mechanisms are one of the most commonly used precision motion systems [9, 10]. Nowadays compliant mechanisms made of metals, polymers, composites, silicon or glass can be fabricated by traditional machining processes (wire electric discharge machining, milling, water jet machining) [8-11], additive manufacturing processes [12-19], or semiconductor lithography processes [20, 21]. Those mechanisms are driven by electrostatic, thermal, magnetic or piezoelectric actuation, even microscale gears [22]. The compliant mechanisms are articulated by the flexure joints, the so-called hinges or springs. The advantages of elastic bending or torsional motion include frictionless, stictionless, backlash-free configuration and compact design. On the other hand, the motion is limited by small flexure joint deflection, low load capacity, and fatigue [23]. As addressed above, the uncertainty induced by thermal effects is unavoidable as long as the electrical motors are used in the motion mechanisms. A majority of studies on the compliant mechanisms have been focused on system design, modeling, actuation, motion control, long-stroke, and high-speed manipulation methods to improve the positioning performance although their motion and dynamic characteristics are extremely sensitive to the temperature variation. The thermal

issues cannot be completely eliminated by calibration or compensation. Zhang [24] characterized dynamic motion behavior of the compliant mechanisms considering the thermal effects at various temperature conditions based on the Finite Element Method (FEM). Furthermore, Zhang [25] characterized the thermal-structural coupling effect of flexure compliant mechanism due to temperature raised from voice coil motor actuating at a high speed. Moreno [26] reported the effect of thermal ageing on the impact and flexural damage behavior. There was an increase in the maximum strength and a decrease in the mechanical properties at high temperatures. Nguyen [27] presented the frequency dependence of thermal noise in aluminum and niobium flexures with a range of 10 ~ 10,000 Hz. Also, it was found that the frequency dependence of thermal noise is relevant to the flexural surface damage or ageing behavior. Awtar [28] proposed the double parallelogram flexure configuration that is fairly insensitive to thermal disturbances. It is obvious that those approaches are attractive to thermal management of the nanopositioning stages toward high positioning performance. Lee [29] reported his preliminary experimental results on dynamic characteristics and temperature effects of pressure-fed mechanisms by using simple cantilever structures with internal fluidic channels. However, there is still insufficient study to directly perform thermal management of flexure mechanisms in an efficient, convenient, low-cost manner as well as avoiding additional attachments or structures to achieve thermal management.

Significant contributions of this study include a new thermal management method to achieve high precision motion quality and new actuation mechanisms by pneumatic pressure and piezoelectric force to minimize the heat source-driven effects on the machine

precision. The static and dynamic behavior of the fluid-fed flexure mechanism-based compliant structure was characterized. The thermal management performance was evaluated by measuring the temperature distribution over the compliant mechanism and thermal displacement under the various compressed air and water flow conditions.

4.3. Mechanism Design and Fabrication

The double compound-type flexure mechanism-based compliant structure with the internal fluidic channels (2.5 mm × 2.5 mm) was designed as shown in Figure 4.1, and was fabricated by metal (Stainless Steel) additive manufacturing. The piezoelectric actuator (5 mm × 5 mm × 10 mm) has placed and the rectangular fluidic channels have symmetrically implemented on each side of compliant mechanism. Pressure gauges are placed at the inlet and outlet of the fluidic channels, so the pressure level (pressure difference) in the internal fluidic channels can be monitored.
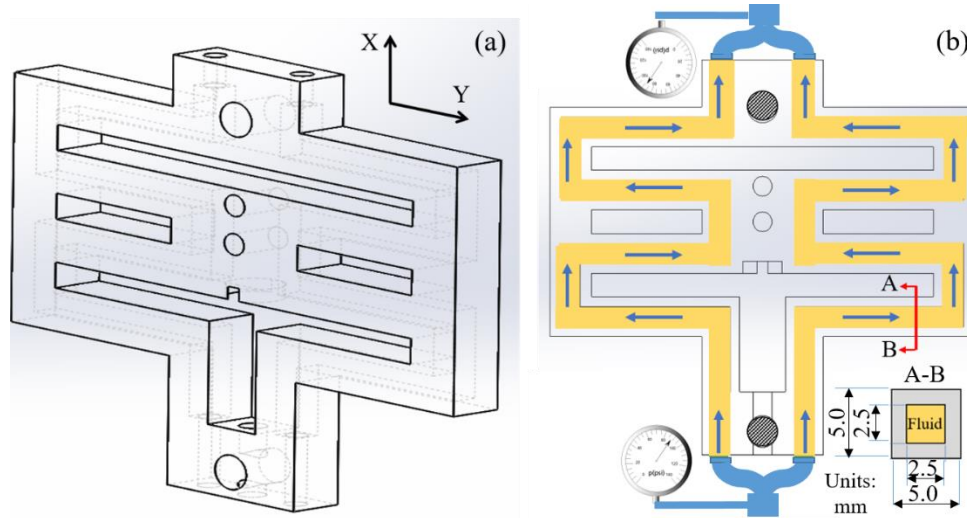
Figure 4.1. Configuration of compliant structure: (a) 3D model and (b) cross-section view. All units are in mm.

Modal analysis of the fluid-fed flexure-based compliant structure was performed by FEM. The 304 Stainless Steel material properties (density 8,000 kg/m^3, elastic modulus 193 GPa, Poisson's ratio 0.29), compressed air properties (density 1.2 kg/m^3 at ambient, 4.0 kg/m^3 at 50 psi and 6.4 kg/m^3 at 80 psi, bulk modulus 101 kPa) and water properties (density 998.2 kg/m^3 at ambient, 996.7 kg/m^3 at 50 psi and 996.7 kg/m^3 at 80 psi, bulk modulus 2.2 GPa) were used for the FEM analysis. Tetra type mesh was used and the number of nodes and elements were 155,766 and 87,382, respectively. As shown in Figure 4.2, the stiffness of the compliant structure showed a similar trend without reference to the fluid media and pressure levels. On the other hand, the high-frequency vibration modes of the compliant structure showed somehow discrepancy in the compressed-air filled conditions. The fundamental and second mode natural frequencies were estimated approximately 3,030 Hz and 3, 050 Hz. The experimental validation was conducted in limited conditions because the compressed water conditions are somehow different to set

95

up in a lab environment. The water was fully filled in the fluidic channels and ran at a certain flow rate. As depicted in Figure 4.3, the pressure gauges were installed in the inlet and outlet of the fluidic channels colored in yellow, respectively. The capacitive sensor (CS, 10 nm resolution) was used, and the displacement was collected by using the data acquisition device (LabVIEW DAQ) while applying force to the shuttle part of the compliant structure. The pressure difference (P_1-P_2) as denoted as ΔP here was manually controlled by reading the pressure gauges. Similar to the FEM result (Figure 4.2 (a)), the experimental results indicated that the stiffness of the compliant structure reveals a similar trend without reference to the medium and pressure. The discrepancy of stiffness between FEM results and experimental results showed approximately 5%.
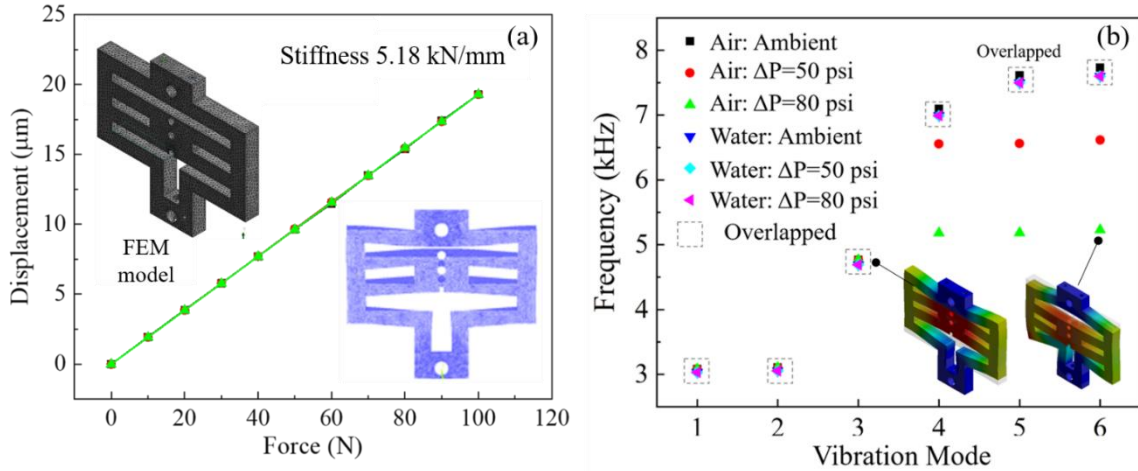
Figure 4.2. Stiffness curves (a) and vibration modes (b) of the flexure-based compliant structure calculated by FEM.
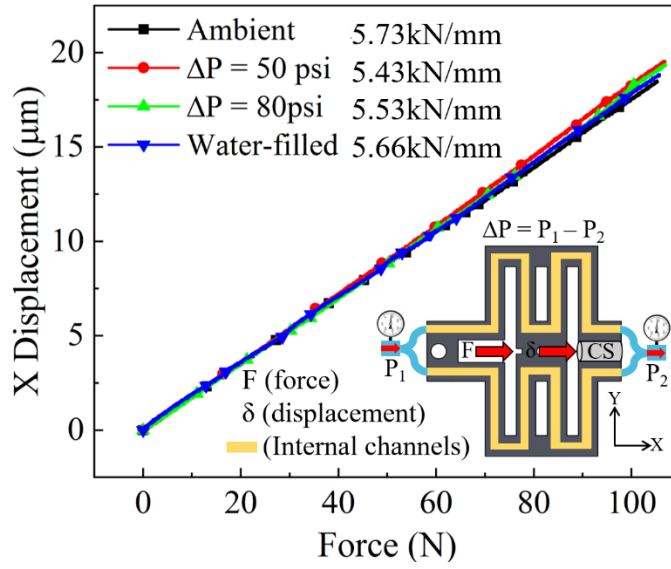
Figure 4.3. Experimental results: stiffness curves.

Two cross-sectional views of the metal additively manufactured compliant structure can be seen in Figure 4.4 and the views were obtained from X-ray CT images. Figure 4.4 (a) shows a 3D reconstruction of the part from CT data and a two-dimensional view of the internal grooves of the part at the location indicated by the green plane in the figure. In the two-dimensional image, it showed two opposite surfaces, top and bottom (or roof and base-floor), with substantially different surface roughness. This can be attributed to the layer growing direction of the printing process. Figure 4.4 (b) shows a two-dimensional CT image at the middle plane between the top and bottom surfaces of the part. From visual inspection, it can be seen that the part is symmetric with respect to the right and left features within CT scan resolution (10~20 µm). Regarding the CT scan details, scanning conditions are listed in Table 4.1. The CT data was reconstructed with a Feldkamp-Davies-Kress (FDK) type algorithm [30, 31] through a cropped Ram-Lak or

97

ramp filter using 3600 projection radiographs for each sample, which were obtained with a Nikon XTH 225 ST system using a tungsten reflection target. The CT data was analyzed with VGStudio MAX (Volume Graphics GmbH) software by applying local adaptive thresholding for surface determination. Since the current CT metrology technique still encounters technical issues to quantify measurement uncertainties associate with the feature recognition dimensional accuracy, the evaluation of surface integrity of the additively manufactured part would be challenging [32]. Therefore, a proper method to compensate for unexpected motion that could not be recognized through conventional scanning systems might require to achieve a high precision level of motion quality.
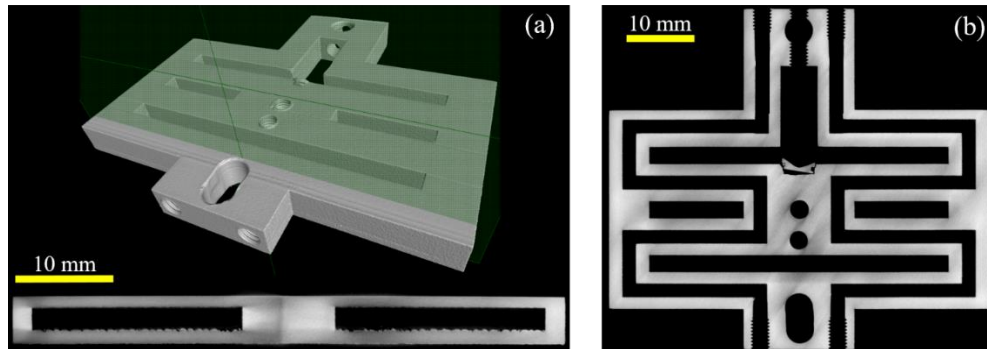
Figure 4.4. CT scanning results: (a) X-direction scanned image and (b) Z-direction scanned image.

Table 4.1. Experimental settings for the X-ray CT scans performed on the metal additively manufactured compliant structure. SOD = source-to-object distance, SDD = source-to-detector distance, Vx = Voxel size, V = tube voltage, I = tube current, Fs = Focal spot size, It = integration time, G = Analog gain.

SOD (mm)	SDD (mm)	Vx (μm)	V (kV)	I (μA)	Fs (μm)	It (s)	G	Pre-filter (mm)
187.2	1125	25	205	89	18.2	1	30x	Cu 1.5

4.4. Experiments and Results

4.4.1. Motion behavior characterization

The experimental setup was constructed on the vibration-isolated optical table. Since the flexure-based compliant structure can be affected by the media and pressure conditions inside the fluidic channels, the stability tests were conducted under ambient, ΔP=50 psi, ΔP=80 psi, and water-filled conditions. The CS outputs were collected for 5 minutes under four experimental conditions. From Figure 4.5, the drift due to the compressed air or water existence inside the fluidic channels was not observed. The displacement noise was approximately 20 nm, root-mean-square (rms) value, for four experiment conditions. As a result, it was confirmed that the media and pressure levels inside the fluidic channels did not have a significant influence on motions of flexure-based compliant structure.
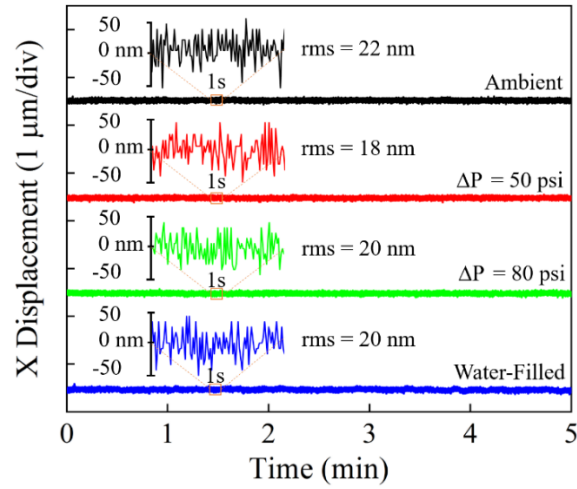
Figure 4.5. Stability test.

The frequency responses of the compliant structure according to the various media and air pressure conditions were obtained by the hammering test. The impact hammer and CS were used and the dynamic signal analyzer (DSA, Agilent 35670a) was used to collect two inputs and to plot the Bode plot as shown in Figure 4.6. The fundamental resonance peak was found out to be approximately 3.2 kHz. It was clearly observed that the existence of media and pressure inside of channels increase damping of the compliant structure and reduce its high-frequency noise. The hammer and sensor were limited to the bandwidth (~5 kHz). Consequently, it is expected that the frequency responses beyond 5 kHz have uncertainty. Based on the response curve, the Q-factor that represents the resonance behavior of the dynamic system between before and after passing through the dynamic resonance regime was also calculated to validate the damping increasing in Table 4.2. As a result, the ambient case showed the highest Q-factor which implies the smallest damping ratio following by water-filled, 50 psi, 80 psi. Therefore, the existence of media in the

fluidic channels increased the damping ratio. These results could be improved by using

high bandwidth sensor and hammering test units.

Table 4.2. Calculated Q-factor based on the frequency response curves.

Condition	Ambient	Δ 50 psi	Δ 80 psi	Water-filled
Q-factor	386	277	117	305
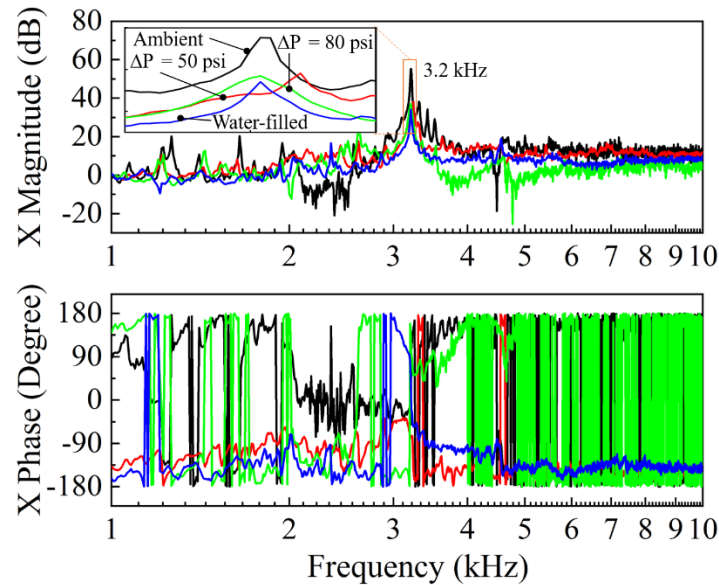
Figure 4.6. Frequency response curve (Bode plot) of the compliant structure under various conditions.

In addition to static and dynamic system characterization, the motion

characteristics of the compliant structure was tested. By applying pressure difference,

denoted as ΔP, between the inlet and outlet of the fluidic channels, the CS measured the

motion of the shuttle part of compliant structure as shown in Figure 4.7. It was found that the flexure-based compliant structure moves up to approximately 160 nm at ΔP 75 psi condition. Although the motion did not linearly increase as the pressure increased because of the open-loop control, the structure promptly responded to the pressure difference. Since the experiment was conducted manually with increasing and decreasing the pressure levels every 5 minutes at the inlet of the compliant structure, this study was limited to obtain the exact response characteristics (rising time, settling time, steady-state error). However, this result implied that such compressed air-driven motion mechanisms can be integrated with piezoelectric (PZT) actuation as coarse-fine motions. The solenoid-based compressed air pressure controller may be employed to properly characterize the compressed air-driven motion mechanisms and to implement a closed-loop positioning control method for better performance.
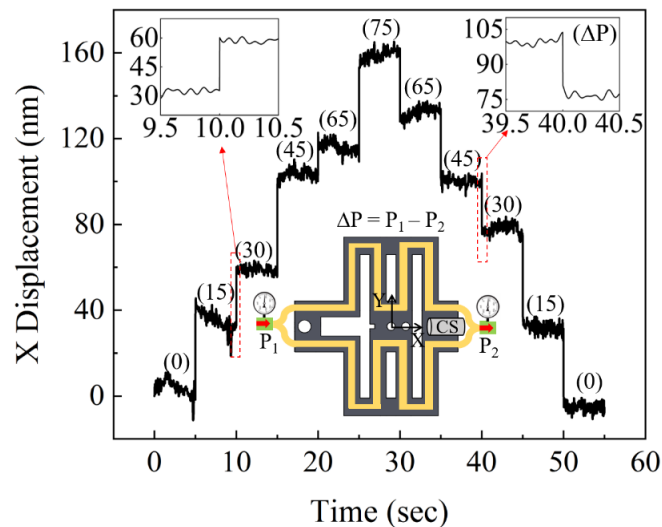
Figure 4.7. Open-loop pneumatic pressure-driven stepwise motion: here (15) indicates the pressure difference ΔP=15 psi.

4.4.2. Thermal behavior characterization

The experimental setup for thermal behavior characterization is shown in Figure 4.8. One cartridge heater was placed on the center of the shuttle part and the five thermocouples (TC) were attached on the top surface of the flexure stage. The CS was placed to measure the variations of thermal displacement as the temperature increases and the compressed air or water starts to flow through the fluidic channels.
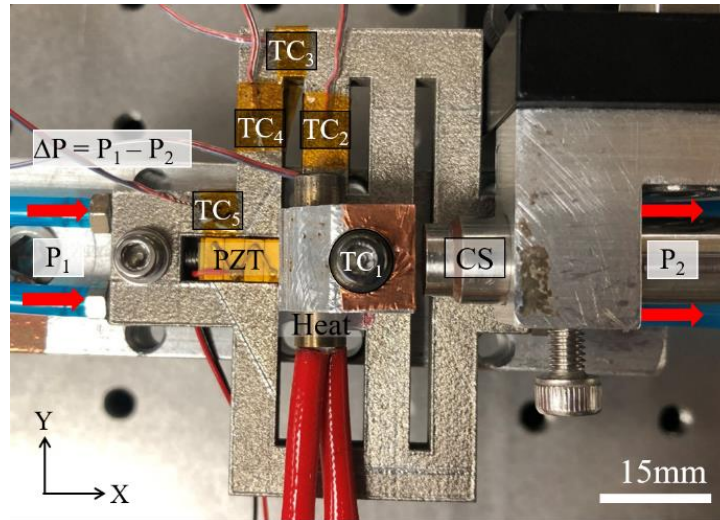
Figure 4.8. Experimental setup for thermal management characterization.

The cartridges heater increased the temperature at TC_1 up to 76 $^\circ$C from the room temperature, and the temperature was saturated within 15 min. The piezoelectric actuator was not included in this experiment. The temperature variations of six different cases (no treatment (ambient), ΔP (10, 20, 50, 80) psi, water flow rate 470 mm/s) at TC_1 were measured for 30 min as shown in Figure 4.9. The temperature at TC_1 continued to rise up

to 76 °C from the room temperature when any thermal management plan was not applied. The compressed air and water started to run at 15 min when the rising in temperature was saturated. From the experiment, the water case showed the best cooling performance. The temperature dropped to approximately 43 °C in 3.5 min in water cases, whereas the compressed air 10, 20 and 50 psi cases showed the temperature drop by 30~35 °C and it took 5.5 min. Interestingly, in the case of compressed air 80 psi showed only 17 °C temperature drop. It was considered that the compressed air 80 psi may exceed the critical fluidic flow rate for the convection heat transfer, and the thermal boundary layer growth could block heat transfer. Further investigation by FEM will be followed-up in a near future.
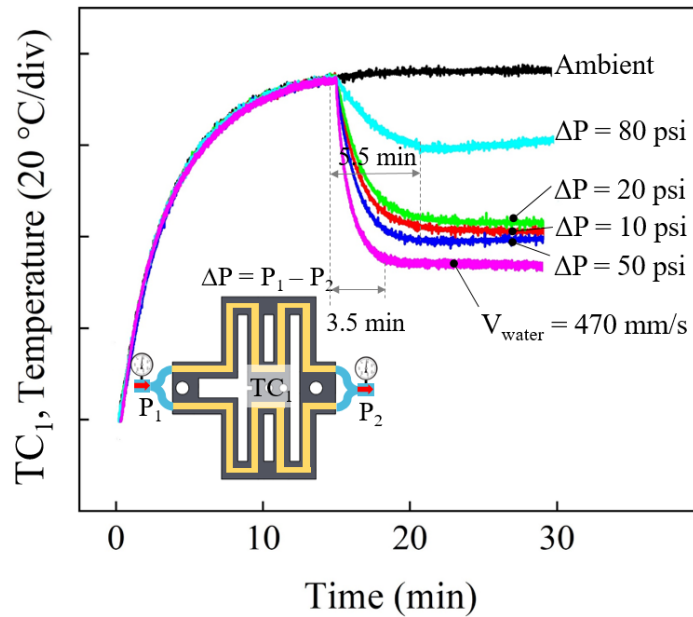
Figure 4.9. Temperature distribution at the hot spot (TC1) according to the media and pressure conditions.

The temperature distributions of each thermal management conditions with five thermocouples were summarized in Figure 4.10 (a)-(f). Although the temperature increase at TC_1 (near the heater) is inevitable, the temperature at TC_5 (near the piezoelectric actuator) was decreased to the room temperature for all cases (Figure 4.10 (b)-(f)). These experiment results indicated that the media and air pressure conditions in the fluidic channels can effectively control the temperature increase. Such thermal management mechanisms have the potential for high precision instruments that require proper thermal environmental controls.
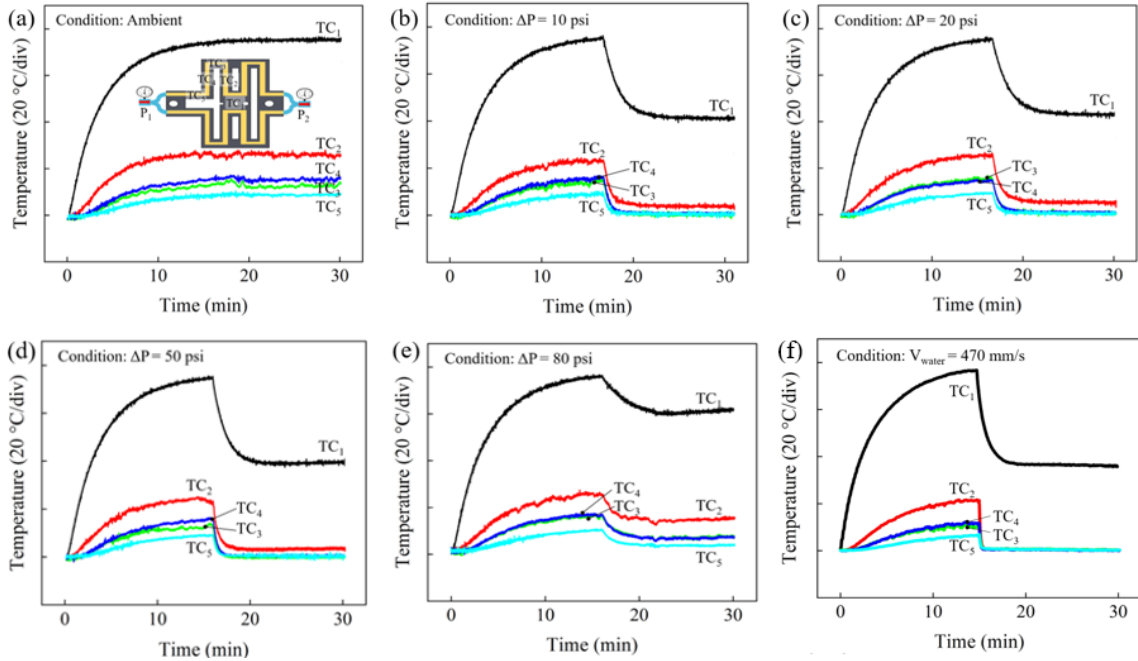
Figure 4.10. Temperature distribution on the compliant structure according to the media and pressure conditions.
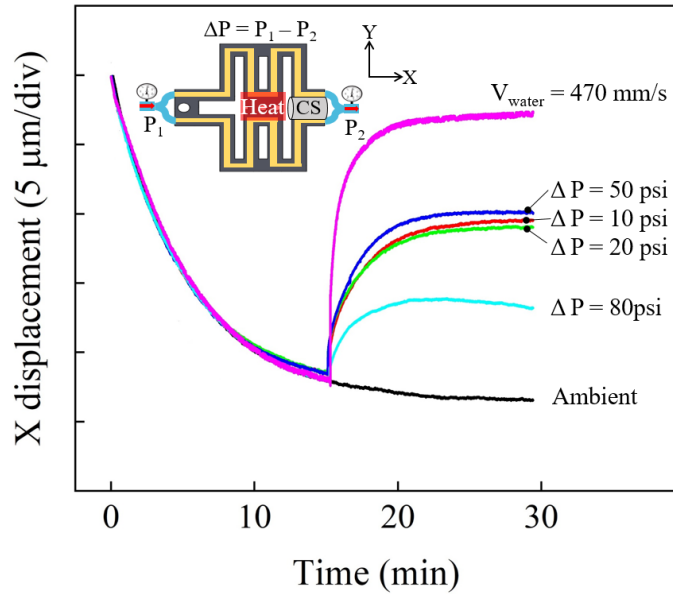
Figure 4.11. Thermal displacement at the shuttle part of compliant structure according to the media and pressure conditions.

While heating up the shuttle area of compliant structure, the thermal displacement was collected under the six different cases similar to above. The CS was used to measure the displacement. As shown in Figure 4.11, the thermal displacement at the shuttle exponentially increased as the heater was on. Although the thermal displacement could not be zero, when the compressed air and water started to run through the fluidic channels, thermal displacements were back up somehow and saturated depending on the media and pressure conditions. Similar to the results in Figure 4.9, the water case had the most effect on the thermal displacement and the ΔP 80 psi case was not efficient to reduce the thermal displacement error compared to other cases.
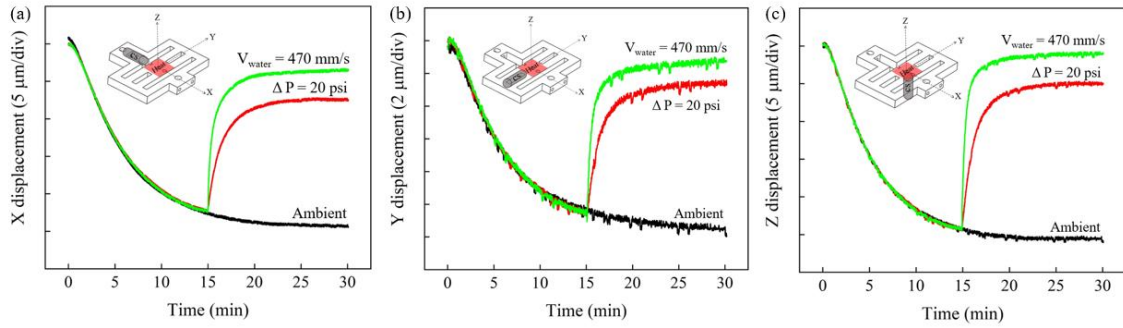
Figure 4.12. X, Y, and Z axes thermal displacement at the shuttle part of compliant structure according to the media and pressure conditions.

To evaluate the performance of proposed thermal management method in uncontrolled directions (e.g. y and x), three CS sensors, indicated as gray cylinder in Figure 4.12, were placed and the data were collected over 30 min. The cartridge heater was placed at the shuttle part to heat up the compliant structure and the compressed air and water started to flow at 15 min. The thermal displacements were collected under three different cases: Ambient, ΔP 20 psi, and water flow at 470 mm/s. Similar to Figure 4.11, thermal displacements induced by heat in all three axes were exponentially increased as temperature raised. By introducing the media and pressure conditions, the increased thermal displacements were backed up and saturated. The thermal displacements could not be all compensated by flowing media; however, when the water started flowing, the thermal displacement significantly reduced to approximately 1.2 μm in the case of y and z axis. Also, the experiment results showed that the water case had most influence in the thermal displacement compare to the compressed air. These experiment results indicated

that the proposed method can effectively minimize the thermal displacement errors not only in the fundamental direction but also in the uncontrolled directions.

4.4.3. Thermal management

After setting up the piezoelectric actuator on the compliant structure, the motions of the flexure mechanism-based compliant structure were measured under four different conditions as shown in Figure 4.13. The sinusoidal and binary inputs were applied to the piezoelectric actuator under ambient, ΔP 50 psi and 80 psi, and water-filled conditions. The actuator was operated in open-loop and the displacement was measured by the CS. Similar to the results of Figure 4.5, the motion quality had no significant difference according to four different conditions. It was considered that the medium-fed mechanisms do not make any fluctuation or variation on the linear motion quality.
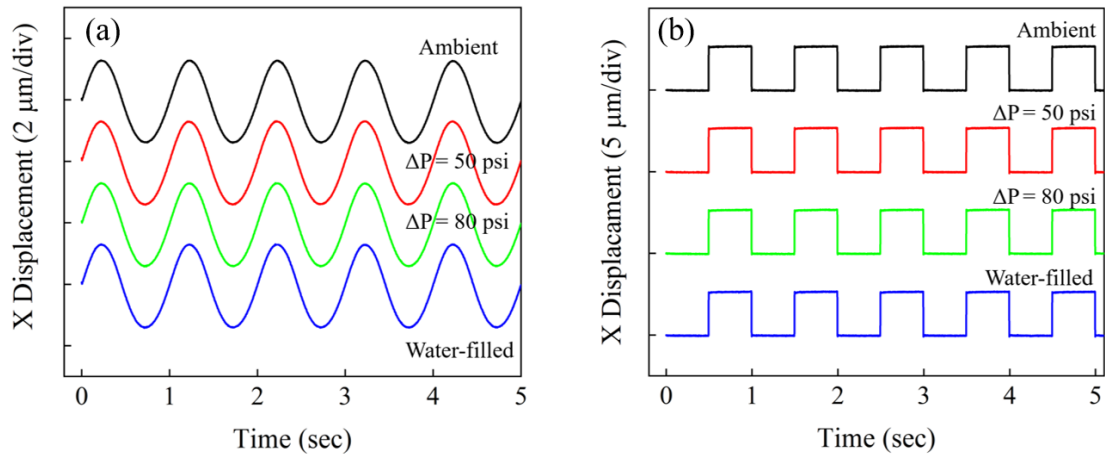
Figure 4.13. Open-loop piezoelectric actuator-driven flexure stage motion according to the media and pressure conditions: (a) 2.5 µm, 1 Hz sine wave input (b) 2.5 µm, 1 Hz binary wave input.

While moving the flexure-based compliant structure (Figure 4.13 (a)), the thermal behaviors at TC_1 (near the piezoelectric actuator) were measured under three different conditions: ambient, ΔP 20 psi, and water flow V 350 mm/s. Similar to the results of Figure 4.9 and 4.10, the temperature increased up to 7 $^{\circ}$C by the heat dissipation of the actuation motor. The compressed air flow and water flow could significantly reduce the temperature increase by approximately 5 $^{\circ}$C and 7 $^{\circ}$C, respectively. Also, the temperature dropped the semi-equilibrium conditions in 6.2 min and 2.6 min for the compressed air and water cases, respectively.
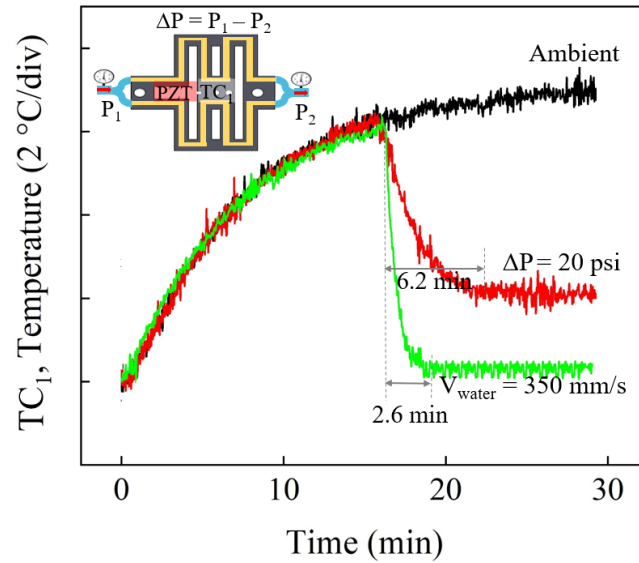
Figure 4.14. Thermal management performance comparison.

The five thermocouples were placed on the compliant structure to measure the temperature variations at different locations. The thermocouples TC_1 and TC_5 near the piezoelectric actuator showed the large temperature increase compared to the other cases

because the piezoelectric actuator dissipated the heat to the frame in contact with the motor. For 30 min observation, the temperature was increased by approximately 7 $^{\circ}$C. The thermocouple TC_5 showed the temperature increase faster than the thermocouple TC_1. However, the decrease in temperature at TC_1, after flowing media in TC_1, showed smaller than TC_5 due to the measured location at TC_1 was not in the direct path of internal channels. In consequence, the compressed air and water flow conditions showed significant temperature decreasing and the water case showed the faster temperature drop.
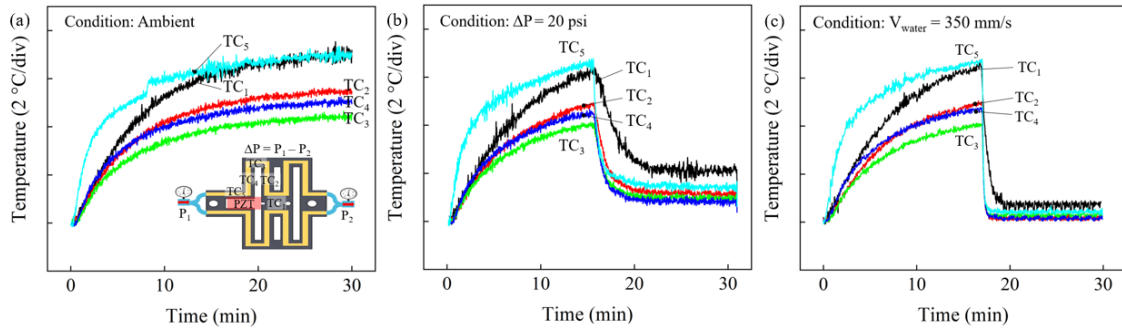
Figure 4.15. Temperature distribution and thermal management performance according to the media and pressure conditions.

4.5. Future Work

This research includes a preliminary FEM analysis and experimental results to validate the proposed thermal management method at the early stage. Because the compliant structure used in this study was additively manufactured, its material properties (density, elastic modulus) could be different from those of bulky material. Moreover, the air voids and surface integrity shown in CT scan results (Figure 4) could be the significant error sources for analysis. In the near future, (1) the material properties of additively

manufactured compliant structure according to printing orientation will be experimentally characterized, (2) static and dynamic behavior of the additively manufactured flexure-based compliant structure will be modeled by FEM, (3) another additive materials will be used to build the flexure mechanisms to enhance the thermal conduction heat transfer performance, and (4) coarse-fine motions by the piezoelectric motor and pneumatic pressure will be tested by constructing feedback positioning control systems.

4.6. Summary

Here the pneumatic motion mechanism with a novel thermal management method was proposed and preliminarily tested under various media and pressure conditions inside of compliant structure fluidic channels to achieve high precision motion quality. The thermal behavior was characterized by measuring the temperature distribution over the flexure-based compliant structure and the thermal displacement under the various compressed air and water flow conditions. As a result, the piezoelectric actuator-induced heat can be conveniently dissipated by applying compressed air flow or water flow through the internal fluidic channels. In addition, the existence of fluidic flows inside of internal channels can increase the damping of the dynamic motion system. Because the temperature variation in precision motion devices negatively affect the positioning accuracy and control in long-term effectiveness, the proposed method can be used in many nanopositioning applications as a proper thermal management method. It is expected that the developed technology can meet the increasing needs for nanometer motion accuracies and meet the efforts to achieve the thermally stable environments in a low-cost, effective, convenient way.

111

4.7. Acknowledgement

4.8. References

[1]   M. Weck, P. McKeown, R. Bonse, U. Herbst, Reduction and compensation of thermal errors in machine tools, CIRP Annals, Vol. 44, Iss. 2, pp. 589-598 (1995).

[2]   Sun-Kyu Lee, Jae-Heung Yoo, Moon-Su Yang, Effect of thermal deformation on machine tool slide guide motion, Tribology International, Vol. 36, Iss. 1, pp. 41-47 (2003).

[3]   Sun-Min Kim, and Sun-Kyu Lee, Prediction of thermos-elastic behavior in a spindle-bearing system considering bearing surroundings, International Journal of Machine Tools and Manufacture, Vol. 41, Iss. 6, pp. 809-831 (2001).

[4]   Brian S. Salmons, Daniel R. Katz, Matthew L. Trawick, Correction of distortion due to thermal drift in canning probe microscopy, Ultramicroscopy, Vol. 110, Iss. 4, pp. 339-349 (2010).

[5]   Jianguo Dai, Jingjing Xia, Cheng Wang and Shanzhen Xu, Thermal analysis of an electromagnetic linear actuator, Advances in Mechanical Engineering, Vol. 9(12), pp. 1-12 (2017).

[6] A. Boglietti, A. Cavagnino, D. Staton, M. Shanel, M. Mueller, and C. Mejuto, Evolution and modern approaches for thermal analysis of electrical machines, Industrial Electronics, IEEE Transactions on, Vol. 56, pp. 871-882 (2009).

[7] Y. Bertin, E. Videcoq, S. Thieblin, and D. Petit, Thermal behavior of an electrical motor through a reduced model, Energy Conversion, IEEE Transactions on, Vol. 15, pp. 129-134 (2000).

[8] Alain C. Diebold, Handbook of Silicon Semiconductor Metrology, CRC Press, 2001.

[9] L. Howell, Compliant mechanisms, John Wiley & Sons Inc, 2001.

[10] S. T. Smith, Flexures, Gordon and Breach Science Publishers, ISBN 90-5699-261-9, 2000.

[11] David J. Guckenberger, Theodorus E. de Groot, Alwin M. D. Wan, David J. Beebe, and Edmond W. K. Young, Micromilling: A method for ultra-rapid prototyping of plastic microfluidic devices, Lab Chip, Vol. 15, No. 11, pp. 2364-2378 (2015).

[12] Heebum Chun, Jaemin Han, Lesley Wright, Alaa Elwany, Herminso Villarraga-Gomez, and ChaBum Lee, Pressure-fed mechanism to compensate for motions and dynamic characteristics of compliant nanopositioning stage, Precision Engineering, Vol. 63, pp. 33-40 (2020).

[13] Jaemin Han and ChaBum Lee, Dynamic and thermal characterization of additively manufactured pressure-fed flexures with internal fluidic channels, Smart Materials and Structures, 28, 105032 (2019).

[14] Herminso Villarraga-Gómez, ChaBum Lee, and Stuart T. Smith, Dimensional metrology with X-ray CT: a comparison with CMM measurements on internal features and compliant structures, Precision Engineering, 51, pp. 291-307 (2018).

[15] ChaBum Lee, Christopher K. Stepanick, Sun-Kyu Lee, and Joshua A. Tarbutton, Cross-coupling effect of large range XY nanopositioning stage fabricated by stereolithography process, Precision Engineering, Vol. 46, pp. 81-87 (2016).

[16] ChaBum Lee, Sun-Kyu Lee and Joshua A Tarbutton, Positioning control effectiveness of optical knife edge displacement sensor-embedded monolithic precision stage, Sens. Actuators A. Vol. 233, pp. 390-396 (2015).

[17] ChaBum Lee and Joshua A Tarbutton, Compliance and control characteristics of an additive manufactured-flexure stage, Rev. Sci. Instrum. 86(4) 045107 (2015).

[18] M. Aliakbari, Additive Manufacturing: State-of-the-Art, Capabilities, and Sample Applications with Cost Analysis, Master of Science Thesis, Department of Industrial Production, KTH, June 2012.

[19] Valmik Bhavar, Prakash Kattire, Vinaykumar Bapuso Patil, S. M. Khot, Kiran Gujar, Rajkumar Raju Singh, A review on power bed fusion technology of metal additive manufacturing, Additive Manufacturing Handbook DOI:10.1201/9781315119105-15 (2017).

[20] S. V. Sreenivasan, Nanoimprint lithography steppers for volume fabrication of leading-edge semiconductor integrated circuits, Microsystems & Nanoengineering, Vol. 3, 17075 (2017).

[21] Byoung Hun Kang, John Ting-Yung Wen, Nicholas G. Dagalakis, Jason J. Gorman, Analysis and design of parallel mechanisms with flexure joints, IEEE Transactions on Robotics, Vol. 21, No. 6 (2005).

[22] Zeyi Wu and Qingsong Xu, Survey on recent designs of compliant micro-/nano positioning stages, Actuators, Vol. 7 (1), 5 (2018).

[23] Tat Joo Teo, Guilin Yang and I-Ming Chen, Compliant Manipulator, Handbook of Manufacturing Engineering and Technology, DOI 10.1007/978-1-4471-4976-7_102-1, Springer-Verlag London 2014.

[24] Xianmin Zhang and Wenfeng Hou, Dynamic analysis of the precision compliant mechanisms considering thermal effect, Vol. 34, Iss. 3, pp. 592-606 (2010).

[25] Lufan Zhang, Xueli Li, Jiwen Fang and Zhili Long, Multi-objective optimization of flexure hinge mechanism considering thermal- coupling deformation and natural frequency, Advances in Mechanical Engineering, Vol. 9 (1), pp. 1-17 (2017).

[26] Irene García-Moreno, Miguel Ángel Caminero, Gloria Patricia Rodríguez, and Juan José López-Cela, Effect of Thermal Ageing on the Impact and Flexural Damage Behavior of Carbon Fibre-Reinforced Epoxy Laminates, Polymers, Vol. 11(1), 80 (2019).

[27] Thanh T-H. Nguyen, Conor M. Mow-Lowry, Bram J. J. Slagmolen, John Miller, Adam J. Mullavey, Stefan Goßler, Paul A. Altin, Daniel A. Shaddock, and David E. McClelland, Frequency dependence of thermal noise in gram-scale cantilever flexures, Phys. Rev. D 92, 112004 (2015).

[28] Shorya Awtar, Synthesis and analysis of parallel kinematic XY flexure mechanism, PhD dissertation at Massachusetts Institute of Technology, 2004

[29]   ChaBum Lee, Jaemin han and Gyu Ha Kim, Additive manufacturing-based adaptive dynamic parameter characterization by using pressure-fed flexure mechanisms, Proceeding of International Manufacturing Science and Engineering Conference 2019 June 10-14, Erie, Pennsylvania, USA.

[30]   Wanli Lu, Ailong Cai, Hanmin Zhang, Lei Li, Linyuan Wnag, and Bin Yan, Fast Fast Feldkamp–Davis–Kress-Type Reconstruction Algorithm in Short Scans for Cone-Beam Computed Tomography via Selective Back-Projection, Journal of Medical Imaging and Health Informatics, Vol. 7, No. 5, pp.1103-1109 (2017)

[31]   L. A. Feldkamp, L. C. Davis, and J. W. Kress, Practical cone-beam algorithm, Journal of the Optical Society of America A, Vol. 1, Iss. 6, pp. 612-619 (1984).

[32]   Herminso Villarraga-Gómez, Ericka L. Herazo, Stuart T. Smith, X-ray computed tomography: from medical imaging to dimensional metrology, Precision Engineering, Vol 60, pp. 544-569 (2019).

5. DAMPING CHARACTERIZATION OF

FLUIDIC PRESSURE-FED MECHANISM (FPFM)[*]

5.1. Overview

This paper represents a novel approach capable of in-process control of the damping parameter of nanopositioning systems by implementing a fluidic pressure-fed mechanism (FPFM). The designed internal structures of nanopositioning stage fabricated by a metal additive manufacturing process can be filled with various fluids such as air, water, and oil under certain various pressure conditions. The damping with respect to fluids and corresponding pressure levels was experimentally characterized through free-vibration tests, hammering test, and sine input sweeping test in open-loop and closed-loop conditions. As a result, the FPFM has the following characteristics: (1) damping may increase when the internal channels filled with fluids and certain pressure level, (2) the dynamic system showed the highest damping when the water exists in internal channels (3) existence of fluids and pressure in the channel does not have a significant influence on the motion quality and positioning control. It is expected that the investigated FPFM method will potentially provide new and efficient approaches to vibration and noise control applications for high precision dynamic systems.

5.2. Preface

The bandwidth and resolution of dynamic systems such as nanofabrication [1], scanning probe microscopy [2-4], aerospace systems [5], and precision optics [6] are limited due to the presence of lightly damped characteristics whether from material properties or designs of systems which are potential causes of resonance vibration. The existence of resonance may significantly degrade the performance of dynamic systems and its control, produces high pitch squealing noise, accelerate the aging of the system, and, in the worst-case scenario, can eventually damage the system that correlates with the safety of operators and system downtime.

Conventional methods for enhancing damping, such as tuned-mass absorbers or viscoelastic damping, are bulky and may not proper for mechanical systems that require compactness. Moreover, those methods do not work well in the low-frequency region. The electromagnetic dampers and shock absorbers are also utilized in many practical applications; however, it requires additional equipment (e.g., pneumatic/hydraulic cylinders, springs, or electromagnetic coils) and periodic maintenance because of wear, friction, or changes in pre-load as it uses over a period of time. Electromagnetic damper, also called regenerative dampers, that use contactless magnetic force, is environmentally friendly since there is no need to use oils, and therefore friction and wear issues can be avoided. Nonetheless, critical issues are still remaining with the ageing of the system, frequency tuning, and reduction of external electromagnetic interferences. The resonance vibration can be significantly reduced or removed by decreasing control loop gains, designing the dynamic system less stiff, and employing the analog/digital low pass filters

(LPF) to the closed-loop control. Yet, those methods will limit the performance and reduce the dynamic system bandwidth. Recently, an active damping control (e.g, positive position feedback [7], polynomial based control [8], shunt control [9-11], resonant control [12], force feedback [13-16], and integral resonance control [17-20], etc.) can be realized by utilizing sensors and feedback control loops for artificially adjusting the damping ratio to desired value of the dynamic systems. Hence, utilizing active damping control is rely on precision feedback sensors and reliable software but the high-performance sensors and software are not only quite expensive but also requires a periodic maintenance. Additionally, damping characteristics of dynamic systems are highly dependent on the design of structure, materials, and system operating conditions. Possessing both high mechanical stiffness and high control loop gains allows the dynamic systems to achieve higher performance while effectively suppressing disturbances. However, in reality, there still exists room for enhancement of technological gap to attain both high system stiffness and high closed-loop loop control gains at the same time while keeping high positioning performance.

Flexure mechanisms are widely used in precision engineering-based systems [21, 22]. However, due to the frictionless bearing structure which acts as pure springs and the presence of light damping in precision positioning systems, it is challenging to design them to have a high bandwidth system and stability. Proportional-integral-derivative (PID) controllers may not work very well for nanopositioning systems [23, 24] because small damping does not suppress the vibration. Although, proportional double integral (PII) [25, 26] controllers are typically used for nanopositioning systems because they can

118

compensate for the tracking error track in a convenient way, it limits the control bandwidth. Many advanced algorithms (e.g,, robust controller (RC) [27], iterative learning controller (ILC) [28], or linear quadratic regulator controller (LQRC) [29]) have been widely introduced to achieve high performance (bandwidth and resolution) of nanopositioning systems. However, in fact, these controllers require high computational effort and time to be implemented.

In this study, flexure-based damping-tunable structures, the fluidic pressure-fed mechanism (FPFM), are monolithically embedded in the linear motion system that can potentially maintain high mechanical stiffness while suppressing the noise and vibration of the dynamic system in an easy, simple, efficient, and low-cost manner. Significance of this study lies to new mechanisms to add damping for achieving high precision motion quality. The proposed FPFM is driven by the pneumatic/hydraulic pressure in the fluidic channels created inside of the compliant mechanism that enables in-situ tune the dynamic characteristics (damping and stiffness) of the dynamic systems to improve the limitation of control bandwidth and positioning performance toward high-speed dynamic systems and control applications.

5.3. Design of Fluidic Pressure-Fed Mechanism (FPFM)

With the advancement of additive manufacturing, complex geometry that could not be obtained by traditional manufacturing methods, now, can now be easily manufactured. AM technology takes advantage of the design flexibility and it can more effectively manage the material distribution (channel shape, size, and placement) in terms of stiffness, damping, and resonance frequency. FPFM can compensate or correct for

119

motion errors and unexpected or undesired dynamic behaviors occurred from manufacturing tolerances or alignment errors by controlling compressed air pressure level inside of internal fluidic channels [30]. Additionally, by flowing fluids into embedded internal channels, the increased heat induced by motors or sensors could significantly be lowered to achieve a thermally stable environment and to have the high precision quality of motion in nanopositioning systems [31, 32].

In the study, the double compound-type flexure mechanism with the internal fluidic channels (2.5 mm × 2.5 mm) was fabricated by AM metal (Stainless Steel) process as shown in Figure 5 (a), The piezoelectric actuator (5 mm × 5 mm × 10 mm) can be placed to cause the linear motion of flexure mechanism, and the created rectangular fluidic channels are bilateral symmetry. Pressure gauge is placed at the inlet of the fluidic channels, so the pressure level in the internal fluidic channels can be monitored.
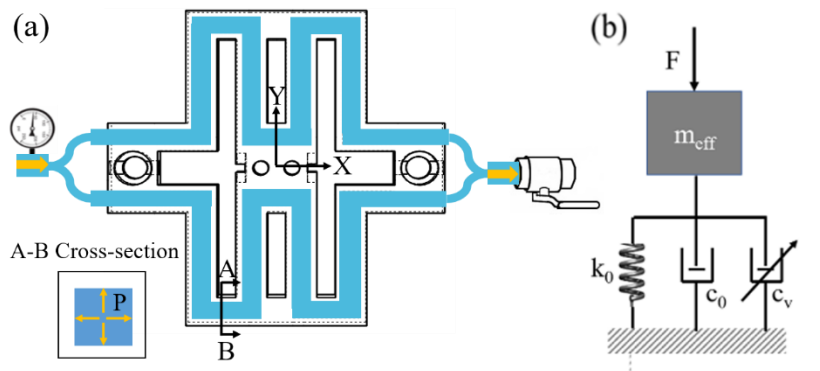
Figure 5.1. Configuration of compliant mechanism with embedded FPFM: (a) cross-section view and (b) dynamic model.

Three different mediums which are air, water, and oil and corresponding pressure levels at 80 psi can be maintained in the internal channels. Considering the geometric effects and pressure-fed medium, the dynamic model of the FPFM can be developed and the developed model will be implemented in the closed-loop control system available for the compliant mechanism as shown in Figure 5.1 (b), where k_0 is the stiffness of the compliant mechanism, the c_0 and c_v are damping parameters of the compliant mechanism and FPFM respectively, and m_{eff} is the effective mass of the system.

5.4. Experiments

The experiment was set up for the damping characterization as shown in Figure 5.2. The piezoelectric (PZT) actuator has placed to cause the linear motion of nanopositioning system and the capacitive sensor (CS, bandwidth of ~10 kHz) was placed to measure the displacement caused by PZT actuation force for free-vibration, frequency responses, and sine input sweeping responses in open-loop and closed-loop controlled conditions according to types of fluids and corresponding pressure levels. Six different cases of fluids conditions (ambient, compressed air pressure at 80 psi, water-filled, hydraulic water pressure at 80 psi, oil-filled, and hydraulic oil pressure at 80 psi conditions) were evaluated and compared to characterize damping affected by FPFM. The outlet of FPFM was blocked so that the media can be filled, and 80 psi of pressure was applied from the inlet of FPFM when media filled in the channels.
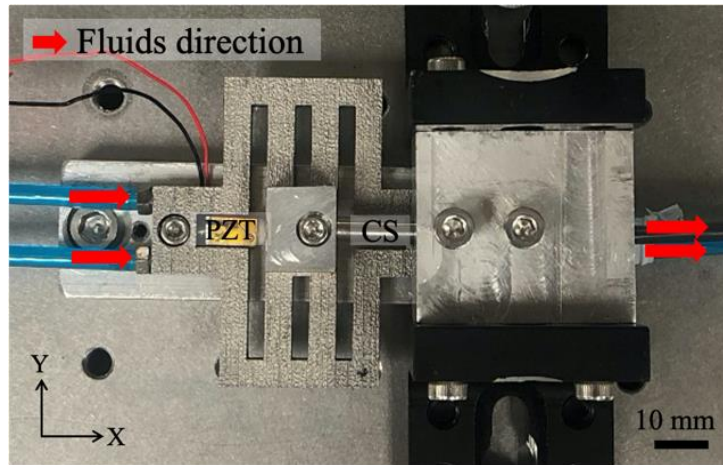
Figure 5.2. Experiment setup for damping characterization.

The stiffness of the fluidic pressure-fed mechanism was experimentally characterized under six different fluidic conditions. The stiffness was measured by CS located at the shuttle part and the displacement data were collected by using the LabVIEW data acquisition device while the shuttle part of the flexure mechanism was forced to cause linear motion of the dynamic system. The result, as shown in Figure 5.3 (a), indicated that the stiffness of the nanopositioning system was measured approximately 7.30 kN/mm. It showed some discrepancy in stiffness measurement with respect to varying media with the maximum difference of 2.6 %. Considering uncertainties involved during the experiment which are the alignment of sensors, force input, and any drift, the result implied there existed no significant difference in stiffness of nanopositioning system as varying media filled inside of fluidic channel. From the finite element analysis as shown in Figure 5.3 (b), the stiffness of the flexures was estimated approximately 7.20 kN/mm for all conditions. These results showed a good agreement with the experimental results.
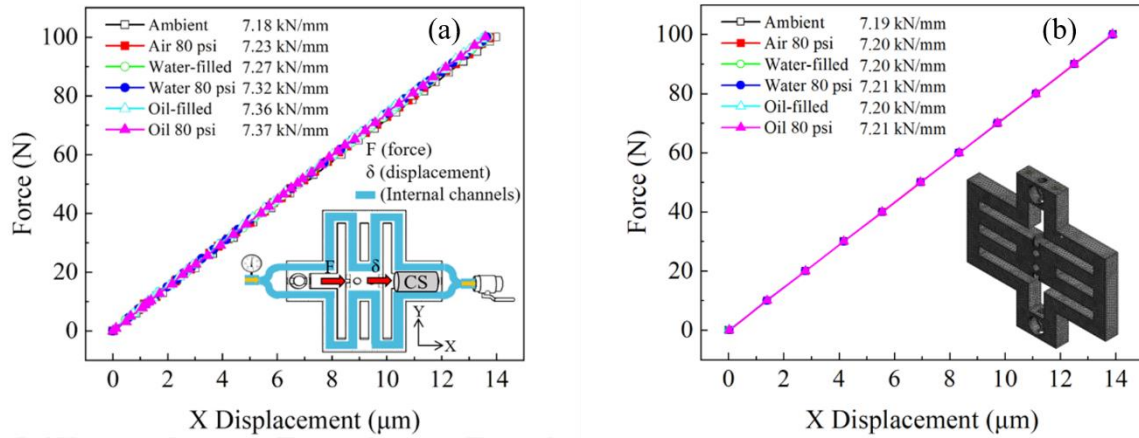
Figure 5.3. Stiffness curves according to the fluid type and corresponding pressure level: (a) experimental results and (b) finite element analysis results.

The frequency responses of FPFM were obtained by impact hammering tests to characterize the damping ratios according to fluid types and corresponding pressure levels. In this experiment, dynamic signal analyzer (DSA, Agilent 35670a) was used to gather displacement by CS sensor and excitation force (PCB 086C03) inputs to plot the frequency response curves as shown in Figure 5.4.

123
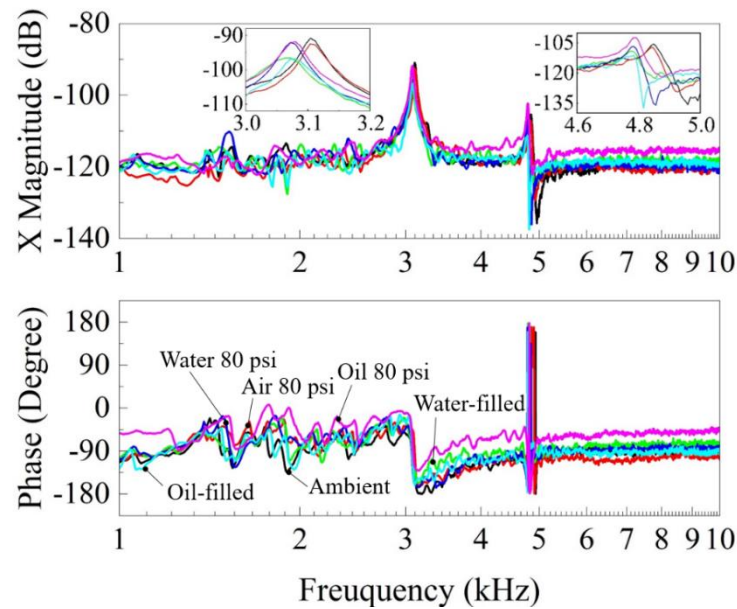
Figure 5.4. Frequency response curve of FPFM with varying media conditions.

The fundamental resonance frequency was estimated to be approximately 3.1 kHz, and the following second mode (torsional vibration) was approximately 4.8 kHz. The result of the frequency response curve showed that the existence of media in the fluidic channels, and according to fluid types and pneumatic/hydraulic pressure condition, the resonance peaks remarkably shifted towards to left which decreased the natural frequency in both cases of the first and second mode of resonance and the amplitude of the peak due to increase in damping. At the second-mode vibration, the difference of amplitude with varying media and pressure conditions may not be precisely present the damping effect since the CS sensor is optimized in measuring the linear but not in the torsional motion. However, it clearly showed that the frequency has shifted toward left. Interestingly, the water-filled case, denoted as a green line in the bode plot, showed the highest damping on

124

FPFM by looking at the amplitude and the stance width at the fundamental resonance frequency.

The quality-factors (Q-factor) were able to acquire which assist to compare the distinction of damping of the dynamic system under varying conditions based on the results in the frequency response curve. As a result, the water-filled case showed the smallest Q-factor as 50.2 which implies the highest damping ratio followed by oil-filled, hydraulic oil pressure (80 psi), hydraulic water pressure (80 psi), compressed air pressure (80 psi), and ambient as shown in Figure 5.5. Hence, it was confirmed that the existence of fluid types and pneumatic/hydraulic pressure inside of fluidic channels can affect the dynamic characteristic of the nanopositioning system and changes the damping parameters.
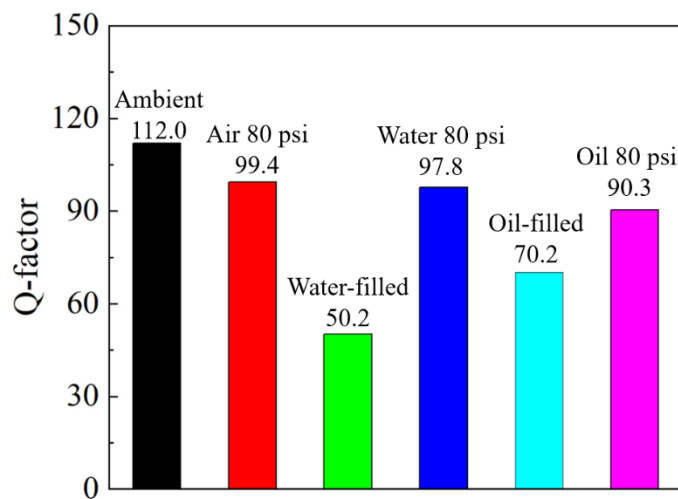
Figure 5.5. Calculated Q-factor based on frequency response curve.

In addition to frequency response tests, free-vibration test was performed to characterize the effects of existing fluid and pressure conditions inside fluidic channels on damping. The CS was used to collect the displacement data while the FPFM was freely excited at the shuttle part and oscillations under varying conditions occurred due to the excitation that conveys the damping characteristics were able to evaluate. Five trials were performed for each different condition to verify the repeatability. Based on the free-vibration test result as shown in Figure 5.6 (a), envelope curves shown in Figure 5.6 (b) were able to draw by using Hilbert transformation to assess the damping ratio. When evaluating the envelope curve, the first 30 milliseconds of oscillation information results were used to show the optimal damping comparison under varying conditions.
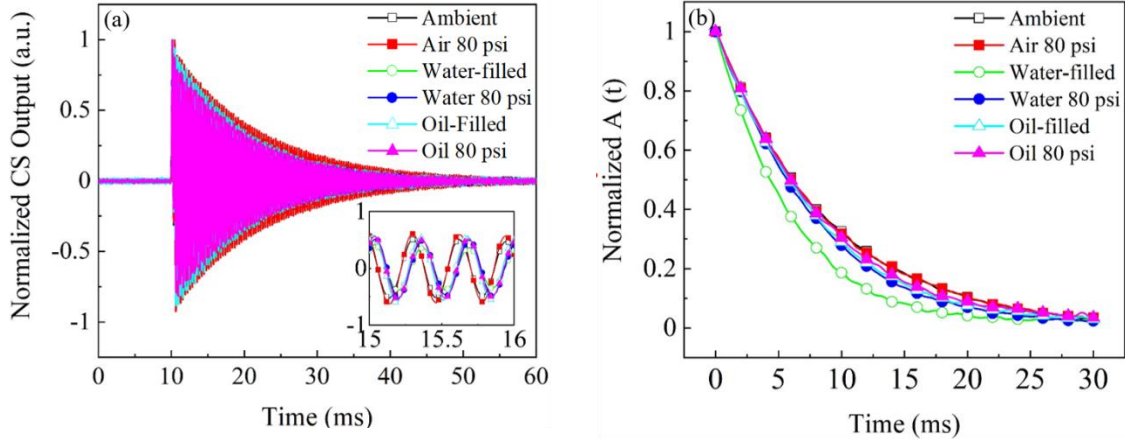
Figure 5.6. Normalized free-vibration results (a) and envelope curves drawn from the free-vibration result (b).

From the envelope curve, as similar in the case of frequency response, the highest damping ratio in water-filled condition can be deduced from the radical exponential

126

decaying tendency. To further examine the effects of varying media conditions on damping, damping coefficients were calculated by taking the coefficient of exponential decaying function from the envelope curve and the natural frequency obtained from frequency responses. The result of the calculated damping coefficient under varying pressure-fed conditions showed the estimated maximum difference of 44.1% of damping coefficient as shown in Figure 5.7. As same to the Q-factor calculation shown in Figure 5.5, the calculated damping coefficient indicated that it is highest when internal channels of FPFM filled with water while it had a comparably smaller effect on damping when the channels filled with oil and applied the pneumatic/hydraulic pressure. The highest damping in water-filled condition was thought due to the higher density of water property. Additionally, although pneumatic/hydraulic pressure applied conditions still showed damping increasing; however, applying pressure rather makes the system to be rather rigid. Therefore, fluidic channels filled with the pressure applied conditions on air, water, and oil had comparably less effect than media filled conditions without pressure, and, as a result, damping was decreased as pressure increasing.
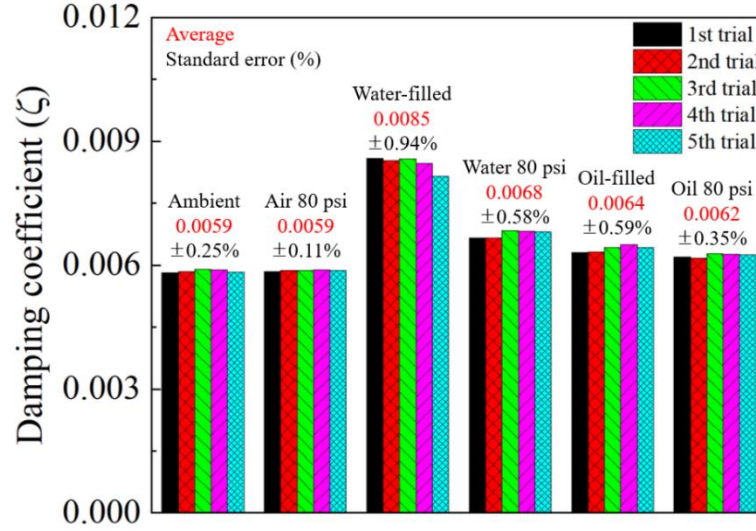
Figure 5.7. Damping coefficients under varying media conditions based on the envelope curve.

The damping parameters of compliant mechanism (c_0) and FPFM (c_v) were able to evaluate with obtained damping coefficient (ζ) from the envelope curve, effective mass (m_{eff}) computed by spring constant (k) from the stiffness curves, and natural frequency (ω_n) from the frequency responses. The damping parameter of FPFM can be found by taking the difference between media filled and ambient conditions since viscous damping connected in parallel in the developed dynamic models. As shown in Table 5.1, the damping parameter of FPFM had the highest effect in water-filled case followed by water 80 psi, oil-filled, oil 80 psi, and air 80 psi condition. When the pneumatic air pressure applied, c_v showed a minimal effect on damping with less than 1 % difference. However, the maximum difference in the case of water-filled condition showed an approximately 47.1 % increase in damping. Therefore, Implementing FPFM on dynamic systems has the

potential for high precision instruments to achieve high bandwidth while maintaining stable performance and high mechanical stiffness by controlling the damping parameters and suppressing noise and vibration.

Table 5.1. Calculated damping parameters (c_0 and c_v) based on the damping ratio.

Condition	Ambient	Air 80 psi	Water-filled	Water 80 psi	Oil-filled	Oil 80 psi
c_0	4.31	4.31	4.31	4.31	4.31	4.31
c_v	~0	0.04	2.03	1.26	0.26	0.12

The motion of FPFM was evaluated by implementing the piezoelectric (PZT) actuator to characterize FPFM dynamic effects while the stage is operating in open- and closed-loop condition. Closed-loop positioning control of FPFM was performed by employing the analog proportional-integral (PI) feedback controller and the control loop gain was tuned on the basis of ambient condition. The sine input responses of the dynamic system showed the damping effects according to six varying conditions. In the open-loop control, as illustrated in Figure 5.8 (a), other than the delayed response time compared with command signal and tracking errors occurred due to the delayed response which estimated to be 100 nm, any difference under six different fluidic conditions was not observed in the system response. On the other hand, when the feedback loop was applied and response of dynamic system well tracked the command input and, as shown in Figure 5.8 (b), the root-mean square (RMS) tracking error was estimated 1.46, 1.44, 1.36, 1.37, 1.42 and 1.44 nm for ambient, air 80 psi, water-filled, water 80 psi, oil filled and oil 80

psi conditions, respectively. The water case showed the smallest tracking error. Again, similar to the results of the open-loop experiments, the dynamic system exhibited no remarkable discrepancy in response with respect to varying media filled inside of fluidic channels because the controller performance is sufficient powerful to compensate for tracking errors. However, the water case showed the smallest tracking error although those tracking errors are similar.
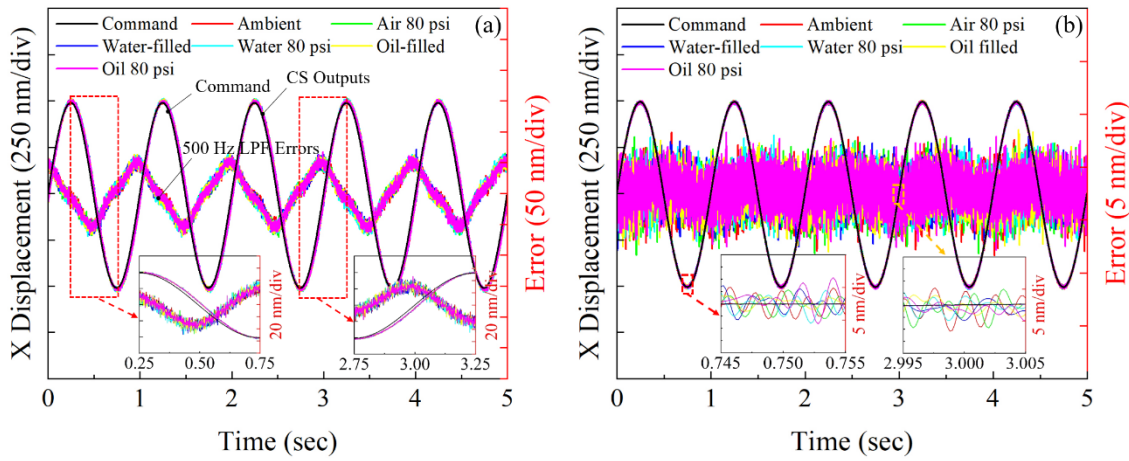
Figure 5.8. Sine motion (1 µm, 1 Hz): (a) open-loop (b) and closed-loop responses.

The step responses were followed to compare the dynamic effects of FPFM when the stage was driving in open- and closed-loop conditions. The result of open-loop responses under varying fluidic conditions showed some steady-state errors as well as delayed response time when rising and falling, and the various vibration modes were found from oscillation with the peak amplitude of more than 700 nm as shown in Figure 5.9 (a). However, it was difficult to evaluate any differences under different fluids and pressure-

fed conditions. When the nanopositioning system was operated under closed-loop control, the response time has improved as well as steady-state errors. Moreover, the various vibration modes were suppressed by applying control loop gains. The closed-loop response showed no significant discrepancy in system response with respect to varying media filled inside of fluidic channels due to the sufficient controller performance for compensating tracking errors.
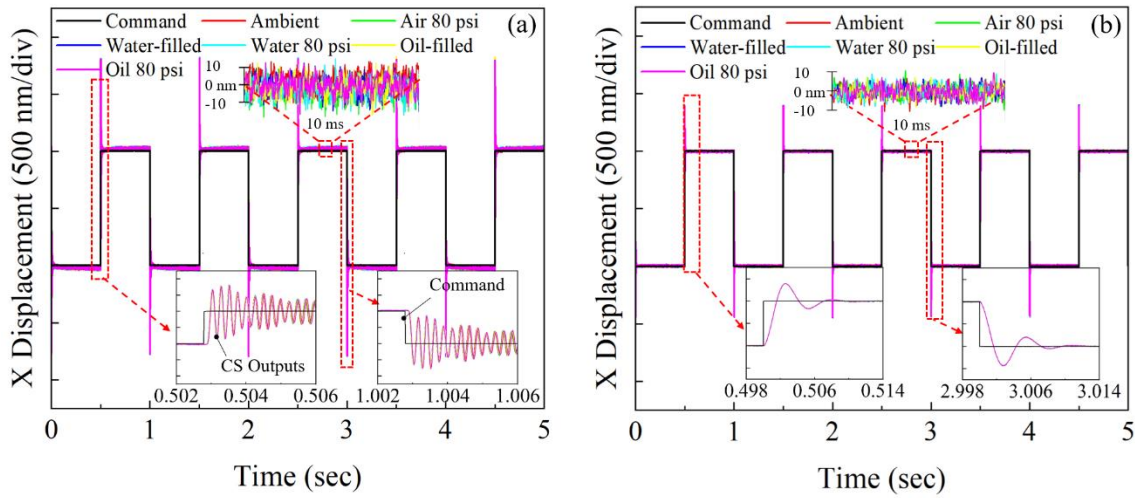
Figure 5.9. Step responses (1 µm amplitude and 1 Hz frequency): (a) open- and (b) closed-loop response.

With the stepwise input (1-sec interval in rising and falling), the response of the system showed the same result as step input. The noise level stayed the same under 15 nm and the overall responses showed the same tendency according to varying fluidic pressure-fed conditions. It was thought that the operating speed of the nanopositioning system was too low which was not in the range of resonance vibration, and hence, the presence of

fluids and pressure on FPFM at low-speed does not have a remarkable influence on motion quality.
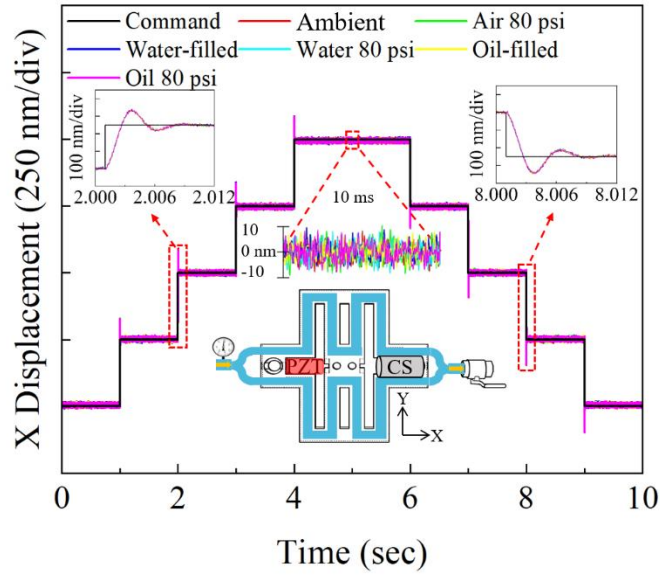
Figure 5.10. Closed loop stepwise motion control results.

To characterize the damping effects according to six different conditions, the sine-sweeping method was performed to discover the damping differences in the higher frequency range, and 0.1 Hz to 10 kHz sine wave inputs were swept. As shown in Figure 5.11 (a), the fundamental resonance frequency was observed around 4.38 kHz and the second mode of vibration (torsional vibration) was estimated at 4.94 kHz. The fundamental resonance vibration had increased compare from the frequency response curve which was around 3.1 kHz because implementing the PZT actuator has connected the spring in parallel and therefore the overall stiffness of FPFM has increased. In a

132

fundamental resonance frequency, it was clearly observed that as media filled in fluidic channels shifting in natural frequency has occurred. Furthermore, the water case showed the lowest magnitude which implies the highest damping. However, in the 2nd mode vibration, the oil-filled cases showed the smallest magnitude but considering the capability of CS limited by measuring linear motion, it was hard to say that the oil-filled case has the highest damping on the torsional mode of vibration. Yet, in both cases of fundamental resonance vibration and torsional mode of vibration, overall damping has increased with respect to varying media conditions since the frequency shifted toward left.

Similar trend showed when the sweeping sine wave was performed under the closed-loop condition. Vibration and resonance of the dynamic system has reduced as media filled into fluidic channels that demonstrated by shfting in frequency and reducing the magnitude as shown in Figure 5.11 (b). Additionally, from the result of open-loop and closed-loop sine sweeping test, the bandwidth of PZT amplifier was observed around 5 kHz.
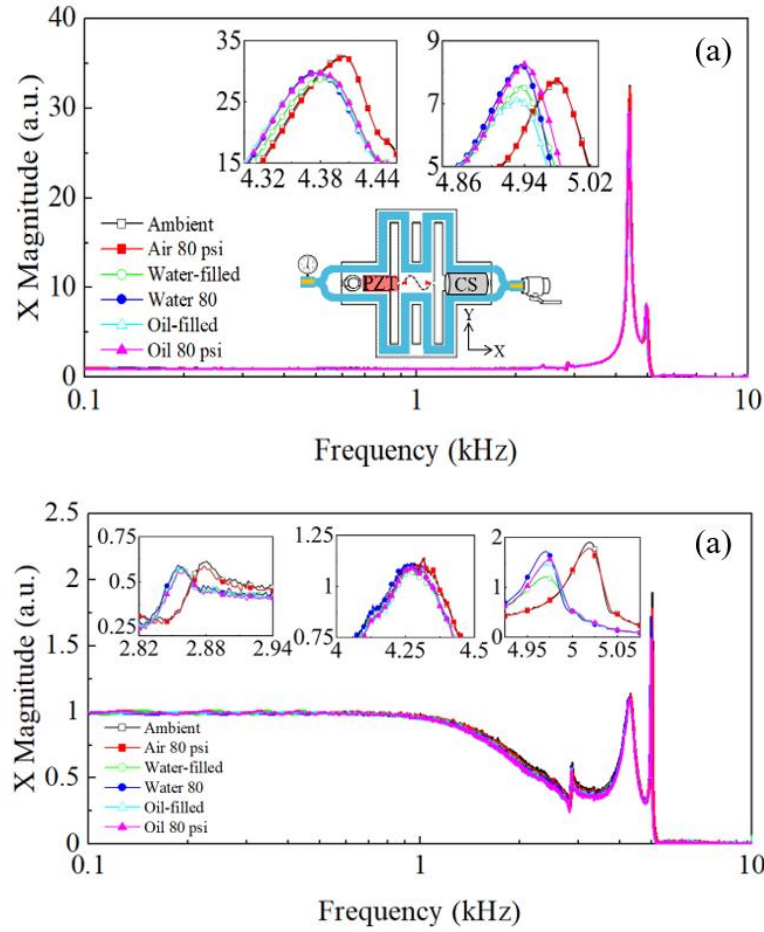
Figure 5.11. Result of sine sweeping test: (a) open and (b) closed-loop responses.

Even though the high stiffness of current flexure system, its damping controllability by FPFM were observed and the medium effects showed the differences in dynamic characteristics of FPFM. It is expected that the FPFM has a significant influence on damping and stiffness for the dynamic systems with low stiffness. The FPFM, therefore, has potentials to effectively control the damping and suppress the vibration by filling media and applying pressure into internal channels and this new approach will ultimately

provide the stable and precise motions of nanopositioining sytem while increasing the limitation of system bandwidth.

5.5. Summary

Here the new approach of in-process control of the damping parameters by the FPFM was proposed and was preliminarily investigated. Damping was characterized by acquiring frequency responses and free-vibration test under open-loop and closed-loop control conditions according to the fluid types and corresponding pneumatic/hydraulic pressure conditions. As a result, the existence of fluids and pressure inside the fluidic channel can increase damping. Furthermore, the motion of FPFM showed a stable response even when the fluids and pressure are filled in the internal channel. Results indicated that the FPFM enables to slightly tune dynamic responses of precision motion system because of its relatively high stiffness. Those effects could become significant as dynamic system becomes compliant. In summary, the FPFM could be implemented in dynamic systems and enhance the motion quality of the nanopositioning system in terms of operating speed, resolution, and stable motion in a low-cost, convenient, and effective way.

5.6. Acknowledgement

135

5.7. References

[1]   A. Ferreira and C. Mavroidis, Virtual reality and haptics for nanorobotics, IEEE Robotics and Automation Magazine, Volume 13, Number 3, pp. 78–92 (2006).

[2]   N. Jalili and K. Laxminarayana, A review of atomic force microscopy imaging systems: application to molecular metrology and biological sciences, Mechatronics, Volume 14, Number 8, pp. 907–945 (2004).

[3]   A. J. Fleming, B. J. Kenton, and K. K. Leang, Bridging the gap between conventional and video-speed scanning probe microscopes, Ultramicroscopy, Volume 110, Number. 9, pp. 1205–1214 (2010).

[4]   K. K. Leang and A. J. Fleming, High-speed serial-kinematic AFM scanner: design and drive considerations, Asian Journal of Control, Volume 11, Number 2, pp. 144–153 (2009).

[5]   V. Giurgiutiu, Review of smart-materials actuation solutions for aeroelastic and vibration control, Journal of Intelligent Material Systems and Structures, Volume 11, pp. 525–544 (2000).

[6]   L. Vaillon and C. Philippe, Passive and active microvibration control for very high pointing accuracy space systems, Smart Materials and Structures, Volume 8, Number 6 (1999).

[7]   J. L. Fanson and T. K. Caughey, Positive position feedback control for large space structures, American Institute of Aeronautics and Astronautics Journal, Volume 28, Number 4, pp. 717–724 (1990).

[8]   S. S. Aphale, B. Bhikkaji, and S. O. R. Moheimani, Minimizing scanning errors in piezoelectric stack-actuated nanopositioning platforms, IEEE Transactions on Nanotechnology, Volume 7, Number 1, pp. 79– 90 (2008).

[9]   A. J. Fleming and S. O. R. Moheimani, Sensorless vibration suppression and scan compensation for piezoelectric tube nanopositioners, IEEE Transactions on Control Systems Technology, Volume 14, Number 1, pp. 33–44 (2006).

[10] A. J. Fleming, S. Behrens, and S. O. R. Moheimani, Optimization and implementation of multi-mode piezoelectric shunt damping systems, IEEE/ASME Transactions on Mechatronics, Volume. 7, Number 1, pp. 87–94 (2002).

[11] A. A. Eielsen and A. J. Fleming, Passive shunt damping of a piezoelectric stack nanopositioner, Proceeding of American Control Conference, pp. 4963–4968, Baltimore, MD, June 2010.

[12] A. Sebastian, A. Pantazi, S. O. R. Moheimani, H. Pozidis, and E. Eleftheriou, A self servo writing scheme for a MEMS storage device with sub-nanometer precision, Proceeding of IFAC World Congress, pp. 9241-9247, Seoul, Korea, July 2008.

[13] A. Preumont, J. P. Dufour, and C. Malekian, Active damping by a local force feedback with piezoelectric actuators, Journal of Guidance, Control, and Dynamics, Volume 15, Number 2, pp. 390-395 (1992).

[14] A. Preumont, Mechatronics, Dynamics of electromechanical and piezoelectric systems. Dordrecht, The Netherlands: Springer, 2006.

[15] A. J. Fleming, Nanopositioning system with force feedback for high performance tracking and vibration control, IEEE Transactions on Mechatronics, Volume 15, Number 3, pp. 433–447 (2010).

[16] A. J. Fleming and K. K. Leang, Integrated strain and force feedback for high performance control of piezoelectric actuators, Sensors and Actuators A, Volume 161, Number 1-2, pp. 256–265 (2010).

[17] S. S. Aphale, A. J. Fleming, and S. O. R. Moheimani, Integral resonant control of collocated smart structures, Smart materials and Structures, Volume 16, Number 2, pp. 439–446, 2007.

[18] B. Bhikkaji and S. O. R. Moheimani, Integral resonant control of a piezoelectric tube actuator for fast nanoscale positioning, IEEE/ASME Transactions on Mechatronics, Volume 13, Number 5, pp. 530–537 (2008).

[19] A. J. Fleming, S. S. Aphale, and S. O. R. Moheimani, A new method for robust damping and tracking control of scanning probe microscope positioning stages, IEEE Transactions on Nanotechnology, Volume 9, Number 4, pp. 438–448 (2010).

[20] I. R. Petersen and A. Lanzon, Feedback control of negative-imaginary systems, IEEE Control Systems, Volume 30, Number 5, pp. 54 –72, (2010).

[21] L. Howell, Compliant mechanisms, John Wiley & Sons Inc, 2001.

[22] S. T. Smith, Flexures, Gordon and Breach Science Publishers, ISBN 90-5699-261-9, 2000.

[23] Y. Chen, C. Hu and K. L. Moore, Relay feedback tuning of robust PID controllers with iso-damping property, Proceeding of 42nd IEEE International Conference on Decision and Control, Volume 3, pp. 2180-2185, Maui, HI, 2003

[24] J. Y. Lee, M. Jin and P. H. Chang, Variable PID Gain Tuning Method Using Backstepping Control With Time-Delay Estimation and Nonlinear Damping, in

IEEE Transactions on Industrial Electronics, Volume 61, Number 12, pp. 6975-6985 (2014).

[25] A. Sebastian and S. M. Salapaka, Design methodologies for robust nano-positioning, in IEEE Transactions on Control Systems Technology, Volume 13, Number 6, pp. 868-876 (2005).

[26] J. Shan, Y. Liu, U. Gabbert, and N. Cui, Control system design for nanopositioning using piezoelectric actuators, Smart Materials and Structures, Volume 25, Number 2 (2016).

[27] Q. Zhao and J. Jiang, Robust controller design for generator excitation systems, IEEE Transactions on Energy Conversion, Volume 10, Number 2, pp. 201-209 (1995).

[28] G. Pinte, B. Stallaert, P. Sas, W. Desmet, and J. Swevers J, A novel design strategy for iterative learning and repetitive controllers of systems with a high modal density: Theoretical background, Mechanical Systems and Signal Processing, Volume 24, Number 5, pp. 432–443 (2010)

[29] P. Misra, LQR design with prescribed damping and degree of stability, Proceedings of Joint Conference on Control Applications Intelligent Control and Computer Aided Control System Design, pp. 28-70, Dearborn, MI, USA (1996).

[30] H. Chun, J. Han, L. Wright, A. Elwany, H. V. Gomez, and C. Lee, Pressure-fed mechanism to compensate for motions and dynamic characteristics of compliant nanopositioning stages, Precision Engineering, Volume 63, pp. 33-40 (2020).

[31] J. Han, and C. Lee, Dynamic and thermal characterization of additively manufactured pressure-fed flexures with internal fluidic channels, Smart Materials and Structures, Volume 28, 105032 (2019).

[32] H. Chun, G. Kim, H. V. Gomez, H. Kim, A. Elwany and C. Lee, Characterization of thermally stable compliant structures with internal fluidic channels, Precision Engineering, Volume 66, pp. 201-208 (2020).

6. A MONOLITHIC LINEAR MOTION PLATFORM DRIVEN BY PIEZOELECTRIC AND FLUIDIC PRESSURE-FED DUAL MECHANISM[*]

6.1. Overview

This research presents a novel dual-mode actuation method capable of generating sub-nanomotion in a monolithic linear motion platform. Unlikely conventional dual-mode stages that utilize piezoelectric and electromagnetic-combined actuation mechanisms consisted of two independent motion axes, the dual-mode actuation, in this study, was developed by combining a piezoelectric actuator for coarse motion and a fluidic pressure-fed actuator for a fine motion, and was implemented in a monolithic flexure stage fabricated by metal additive manufacturing. The fluidic pressure-fed mechanism actuates the flexure stage by pneumatically pressuring the fluidic channels that were created inside the flexure spring structures. Experimental tests were performed to investigate the performance boundary of the fluidic pressure-fed actuation mechanism and a monolithic linear motion platform. A proportional pressure controller was used to generate a fine motion. The piezoelectric actuator showed a sensitivity of 4.73 μm/V found from previous chapter 5, and the fluidic pressure-fed actuator showed the forward sensitivity of 158 pm/psi and 110 pm/psi for backward direction. The proposed dual-mode actuation method enabled to achieve pico-scale resolution motion.

---

[*] This research work will be submitted to the Precision Engineering Journal and it is under preparation.

6.2. Preface

Nanopositioning requiring nanoscale positioning accuracy and precision is a key enabling technology for multidisciplinary research interconnecting nanoscale science and engineering [1-3]. To achieve such high positioning accuracy and precision at high speeds, dual-stage mechanisms combined with robust closed-loop controls are often used in the field of optical recording [4], robotic manipulation [5, 6], wafer fabrication, mask correction, or scanning applications [7, 8].

The dual-stage mechanisms consist of two separate coarse and fine motion axes. The dual-stage adapts merits of both coarse and fine actuation mechanisms to achieve high positioning performance; for example, the fine stage driven by piezoelectric (PZT) actuator, voice coil motors, or micro-electric-mechanical system (MEMS)-based actuators compensates for positioning error resulted from the coarse stage driven by leadscrews or ball screws. Consequently, the feedback positioning control has been also widely studied to look for the master-slave control strategy available for various dual-stage applications [9]. Traditionally, because the fine motion stage is typically placed on the coarse motion stage, dual-stage motion systems adapt two separate motion axes [10, 11]. Although two stages could be built into the same traveling axis, there must be offset distance between two axes along the vertical direction, which could result in an Abbe error. Also, leadscrew- or ball screw-driven mechanisms are not vacuum compatible, and linear motors produce heat generation that degrades the dynamic system performance [12]. Thus, there exist dual-stage system design issues: alignment of two motion axes, an increase in the weight and size of the system, thermal instability between two motion axes, and synchronization

of dual-stage servo systems [9, 12, 13]. Those issues must be taken into account in the dual-stage system and controller design process. However, the design and control approaches to dual-stage systems are more sophisticated than those of a single-axis motion system and require advanced control methods.

Many approaches have been studied to improve the dual-stage positioning performance by innovating the mechanical-electrical system design [14,15] and implementing advanced closed-loop feedback and feedforward control algorithms [16,17]. Also, a few unique displacement feedback sensors were developed to enhance positioning control effectiveness at high speeds [18-21]. Conventionally, piezoelectric, electrostatic, electromagnetic, and magnetomotive force-driven mechanisms are more conveniently used than pneumatic or hydraulic pressure-driven motion mechanisms [22-25]. Moreover, it is considered that piezoelectric actuators are used for fine motion mechanisms in a majority of dual-stage applications. However, pneumatic or hydraulic actuators have advantages such as low heat generation, non-magnetic use, and clean energy source over the other actuators [26]. Tadano *et al.* developed a single axis coarse-fine dual positioning stage by utilizing a pneumatic cylinder with air bearings and a pneumatic bellows-driven actuator [27]. Chiang proposed XY servo pneumatic-PZT hybrid actuators and control methods for long-stroke and high positioning accuracy [28, 29]. Pneumatic or hydraulic actuators used in many previous dual-stage applications had to have air bearing cylinder-type mechanisms in their own linear axes. Therefore, still, there is little study on novel design approaches to pneumatic or hydraulic actuation mechanisms.

In this paper, the fluidic pressure-fed mechanisms (FPFM) driven by pneumatic pressure for a fine motion was combined with the PZT actuator for a coarse motion, and those actuation mechanisms was implemented into a single axis flexure stage. In general, the PZT actuators are used for a fine motion. The FPFM does not have a physical system for actuation, but utilizes the fluidic channels created inside the flexure springs. Pneumatic pressure control enabled to generate a sub-nanoscale motion. In this paper, preliminary study for pneumatic actuation in a monolithic flexure mechanism, hysteresis and nanoscale motion quality of the FPFM including were discussed.

6.3. Dual-Stage Design and Fabrication

The proposed dual-stage mechanism based on the flexure stage includes the PZT actuator for a coarse motion and the FPFM actuator for a fine motion as shown in Figure 6.1. Here m is the mass of flexures, and the k and c indicate the stiffness and damping of body (flexures), FPFM and PZT actuator, respectively. The fine motion can be achieved by pressurizing the fluid (compressed air or oil) filled in the fluidic channels. Conventionally, the pneumatic or hydraulic actuation involves the cylinders and air/oil bearing configuration. However, the FPFM utilizes fluid flow under the corresponding pressure level to actuate the flexure stage for the fine motion. Therefore, the FPFM does not require additional cylinders or air/oil bearing configuration, but can be integrated with the system at ease and low-profile.
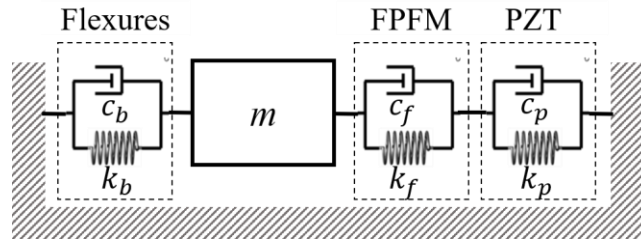
Figure 6.1. Dynamic model of PZT-FPFM dual-stage.

The dual-stage mechanism was implemented with the flexure stage used for the previous studies: thermal stability characterization and dynamic motion characterization [30-32]. This flexure stage was fabricated by Stainless Steel additive manufacturing (AM). Due to the dimensional tolerance of metal AM printer, the minimum wall thickness of the fluidic channels was set to 1.25 mm, fluidic channels were designed 2.5 mm $\times$ 2.5 mm as seen in Figure 6.2. At the early stage, proportional pressure controller (PPC) and pressure sensor (PS), capacitive sensor (CS) are used to characterize the pneumatic pressure driven motion of flexure mechanism. Because the pneumatic pressure-driven motion mechanisms include the hysteresis according to the actuation direction, the bidirectional proportional pressure controller (BPPC) and CS for the feedback will be employed and investigated. PZT actuator will also be feedback controlled to generate dual-mode motion.
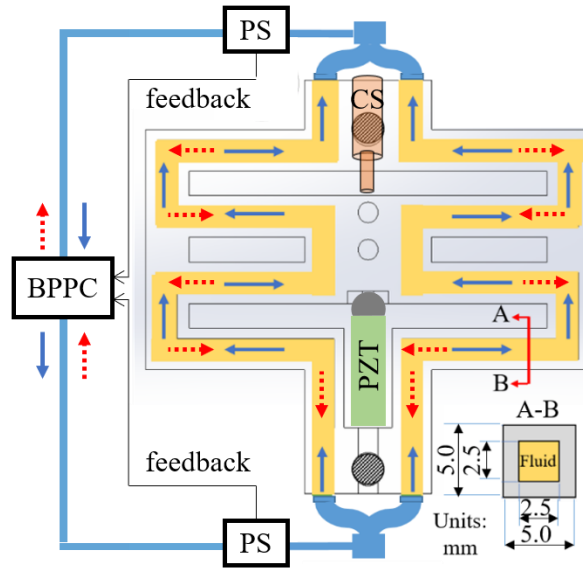
143

Figure 6.2. Concept of PZT-FPFM dual-stage system.

Computational approaches to the motion and dynamic behavior characterization of the FPFM could be attractive to understand its mechanism better. However, it involves the fluid-coupled dynamic analysis, and requires an accurate dynamic modeling capable of analysis of nanometer scale deformation and fluidic pressure distribution over the channel. Thus, in this study, experimental approaches to implementing the FPFM with the dual-stage mechanism for preliminary feasibility tests were mainly focused.

6.4. Experiments and Results

The initial experiment setup is shown in Figure 6.3. To identify and characterize the actuation direction, PPC was placed at the inlet of the fluidic channel, and CS was placed in the opposite direction. PS was utilized at the outlet of pressure to monitor the variations of pneumatic pressure. PZT was also placed since pneumatic actuation will eventually be combined with PZT for a coarse-fine motion.

144
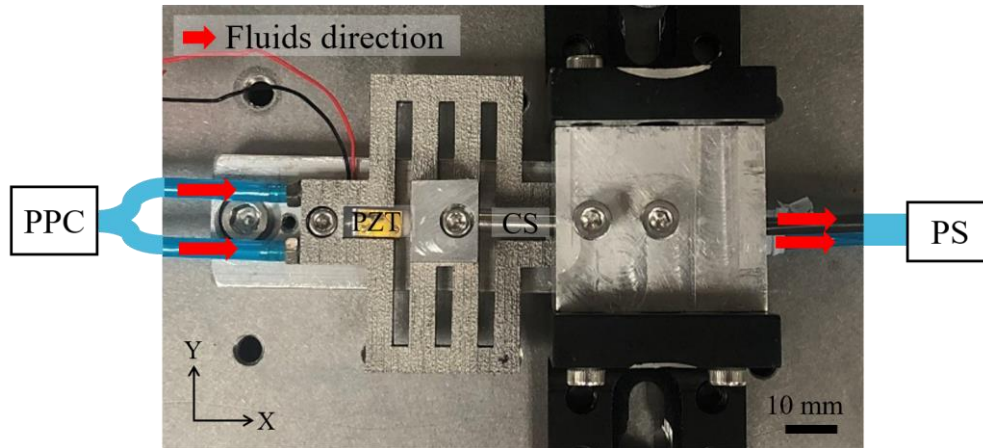
Figure 6.3. Initial dual-stage experiment setup.

The PPC was able to receive analog signals such as sine wave or square wave. Hence, the characterization of FPFM driven motion was performed under various inputs. Figure 6.4 shows the open-loop responses of pneumatic pressure-driven motion. When 1Hz binary input was given to PPC, the maximum response of pressure controller was identified approximately as 2 Hz with some induced vibration from PPC due to the difficulty of controlling pneumatic pressure in the lab scale. The nanopositioning stage was promptly responded and moved up to approximately 11 nm at the maximum 80 psi pneumatic pressure under two different signals (sine and square wave with 1 Hz frequency). Although the actuation direction was correctly found regarding fluid direction, the result showed that springback in the motion did not occur in the open-loop response.

Figure 6.4. Open-loop pneumatic pressure driven motion results: (a) 1 Hz sine wave input and (b) 1 Hz binary input.
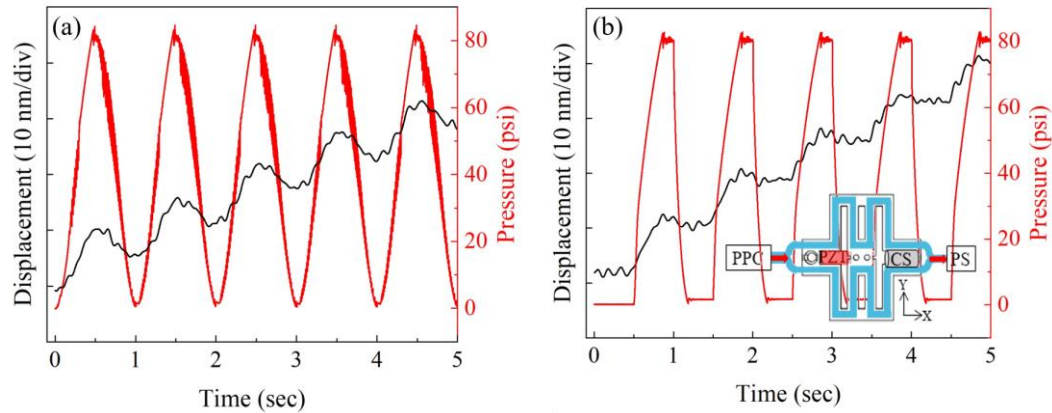
Therefore, the hysteresis, according to the actuation direction, was analyzed based on the obtained open-loop response with five sine wave input. To find a hysteresis loop, the pressure was calibrated into the force with the measured stiffness of the flexure mechanism in the previous chapter 5. Consequently, shown in Figure 6.5, the flexure stage motion with the maximum displacement of 11 nm was in the hysteresis region so that the elastic restoring did not occur. Flexure mechanism generates motion with the nature of elastic bending of the material. However, it was thought that, in the sub-nano scale motion, the spring structure of the flexure mechanism is in between elastic and plastic regions, and thus, the relaxation time takes long for making the nanopositioning stage to move back. Therefore, to mitigate the hysteresis, applying bidirectional pneumatic pressure was concerned to restore the flexure stage back to the starting position.
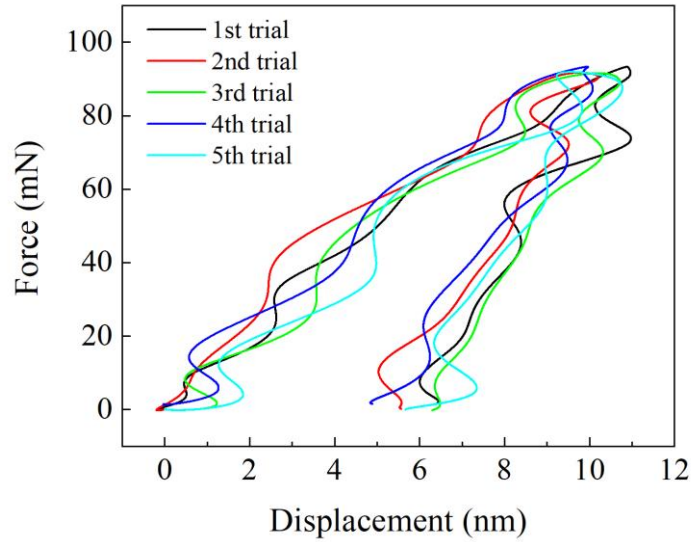
146

Figure 6.5. Hysteresis loop of FPFM driven motion.

After applying bidirectional pressure into fluidic channels, it was able to calibrate the stage motion, and the directional sensitivity of the fluidic pressure-fed actuator was able to obtain. Here, the actuation direction is denoted as the forward direction, while the other direction was defined as the backward direction. As shown in Figure 6.6, although the stepwise motion showed that applying the pneumatic pressure in a backward direction could not move the nanopositioning stage back to the original position, bidirectional pressure was able to mitigate the hysteresis effect and if a proper control method is applied, the motion of the nanopositioning system was thought to be controllable. As a result, when applying pressure into the forward and backward direction, the sensitivity was estimated as 158 nm/psi and 110 pm/psi, respectively. FPFM driven motion showed the feasibility of using as a fine motion, and the FPFM actuated the flexure stage to generate a sub-nano

scale motion. Interestingly, the forward direction response showed some minimum pressure load to move the nanopositioning stage linearly.
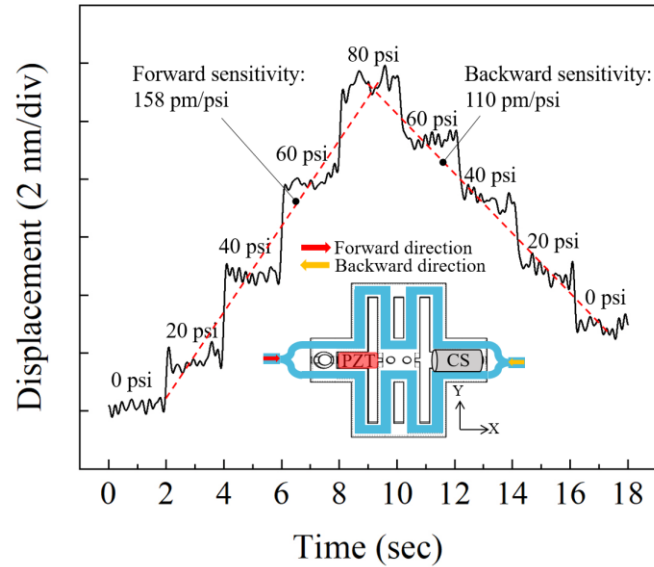
Figure 6.6. FPFM driven motion under bidirectional stepwise input.

Currently, the FPFM driven motion using bidirectional pressure with compressed air and oil is under investigation, as shown in Figure 6.7. Furthermore, soon, BPPC and CS, as shown in Figure 6.2, will be implemented for feedback control to achieve dual-mode motion control. The switching mode or master-slave control loop of air actuation for a fine motion and PZT for a coarse motion will be developed to enable the dual-stage system that provides high precision sub-nanometer motion and high positioning performance. Additionally, the actuation performance with respect to hydraulic (oil) pressure will also be analyzed and compared with compressed air.

Figure 6.7. Experiment set up for bidirectional pneumatic/hydraulic pressure driven actuation.

6.5. Summary

This study showed the feasibility that the FPFM combined with the PZT actuator can be used for a fine motion generation in dual-stage applications. Positioning control eff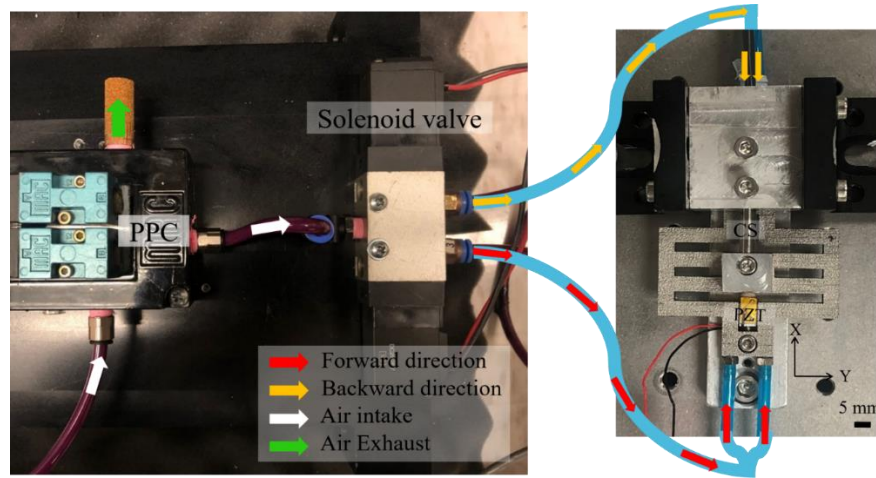ectiveness of the FPFM was experimentally evaluated. The use of the FPFM has advantages such as low heat generation, non-magnetic use, and clean energy source over the other conventional actuators and is vacuum environment-compatible due to no contamination source. Also, the FPFM can be integrated with the linear motion system at ease, low-profile, and low-cost not only for actuation applications but also for vibration and noise control of mechanical systems because it does not require additional cylinders or air/oil bearing configuration. The FPFM contribution to the motion range and dynamic characteristics of the stage can be significantly prominent as the AM technology develops further to fabricate the internal fluidic channels with various shapes or structures more accurately and precisely. For future work, computational approaches to dynamic

characterization of the FPFM will be conducted to establish the FPFM dynamic models

for dynamic system identification and hysteresis compensation.

6.6. References

[1]   E. Eleftheriou, T. Antonakopoulos, G. Binnig, G. Cherubini, M. Despont, A. Dholakia, U. Durig, M. Lantz, H. Pozidis, H. Rothuizen, and P. Vettiger, "Millipede—A MEMS-based scanning-probe data-storage system," IEEE Trans. Magn., vol. 39, no. 2, pp. 938–945 (2003).

[2]   R. A. Oliver, "Advances in AFM for the electrical characterization of semiconductors," Rep. Progr. Phys., vol. 71, no. 7, p. 076501 (2008).

[3]   T. Ando, T. Uchihashi, and T. Fukuma, "High-speed atomic force microscopy for nano-visualization of dynamic biomolecular processes," Prog. Surf. Sci., vol. 83, pp. 337–437 (2008).

[4]   S. G. Stan, The CD-ROM Drive: A Brief System Description. Norwell, MA, USA: Kluwer, 1998.

[5]   S. Kwon, W. K. Chung, and Y. Youm, "On the coarse/fine dual-stage manipulators with robust perturbation compensator," in Proc. IEEE Int. Conf. Robot. Autom., vol. 1, pp. 121–126 (2001).

[6]   J. E. McInroy and S. S. Aphale, "Optimal filters from task velocities to joint velocities including both position and velocity limits, 42nd IEEE International Conference on Decision and Control (IEEE Cat. No.03CH37475), Maui, HI, 2003.

[7]   T. Tuma, W. Haeberle, H. Rothuizen, J. Lygeros, A. Pantazi, and A. Sebastian, "Dual-stage nanopositioning for high-speed scanning probe microscopy," IEEE/ASME Trans. Mechatronics, vol. 19, no. 3, pp. 1035– 1045 (2014).

[8]   C. K. Pang, G. Guo, B. M. Chen, and T. H. Lee, "Self-sensing actuation for nanopositioning and active-mode damping in dual-stage HDDs," IEEE/ASME Trans. Mechatronics, vol. 11, no. 3, pp. 328–338 (2006).

[9]   H. Zhu, C. K. Pang, T. J. Teo, "Integrated servo-mechanical design of a fine stage for a coarse/fine dual-stage positioning system," IEEE/ASME Trans. Mechatronics, vol. 21, no. 2, pp. 329–338 (2006).

[10]   Y. T. Liu, R. F. Fung, and C. C. Wang, "Precision position control using combined piezo-VCM actuators," Precision Eng., vol. 29, pp. 411–422 (2005).

[11] Y. Song, J. Wang, K. Yang, W. Yin, and Y. Zhu, "A dual-stage control system for high-speed, ultra-precise linear motion," Int. J. Adv. Manuf. Technol., vol. 48, no. 5–8, pp. 633–643 (2010).

[12] Guanqiao Shan, Yingzi Li, Liwen Zhang, Zhenyu Wang, Yingxu Zhang and Jianquiang Qian, Contributed review: Application of voice coil motors in high-precision positioning stages with large travel ranges, Review of Scientific Instruments, 86, 101501 (2015).

[13] Z. P. Wu and X. L Chen, "Design of coarse-fine combined synchronization control system for lithography based on cross-coupled sliding mode control," Advanced Materials Research, 383-390, pp. 2126-2131 (2011).

[14] J. H. Kindt, G. E. Fantner, J. A. Cutroni, and P. K. Hansma, "Rigid design of fast scanning probe microscopes using finite element analysis," Ultramicroscopy, vol. 100, pp. 259–265 (2004).

[15] Y. K. Yong, S. S. Aphale, and S. O. R. Moheimani, "Design, identification, and control of a flexure-based XY stage for fast nanoscale positioning," IEEE Trans. Nanotechnol., vol. 8, no. 1, pp. 46–54 (2009).

[16] A. Sebastian and S. M. Salapaka, "Design methodologies for robust nanopositioning," IEEE Trans. Control Syst. Tech., vol. 13, no. 6, pp. 868–876 (2005).

[17] A. J. Fleming and S. O. R. Moheimani, "Sensorless vibration suppression and scan compensation for piezoelectric tube nanopositioners," IEEE Trans. Control Syst. Tech., vol. 14, no. 1, pp. 33–44 (2006).

[18] ChaBum Lee, Sun-Kyu Lee and Joshua A. Tarbutton, "Novel design and sensitivity analysis of displacement measurement system utilizing knife edge diffraction for nanopositioning stages," Rev. Sci. Instrum. Vol. 85, 095113 (2014).

[19] ChaBum Lee, Sun-Kyu Lee and Joshua A Tarbutton, "Positioning control effectiveness of optical knife edge displacement sensor-embedded monolithic precision stage," Sens. Actuators A. Vol. 233, pp. 390-396 (2015).

[20] Abolfazl Zolfaghari, Seongkyul Jeon, Christopher K. Stepanick, and ChaBum Lee, A novel sensor for two degree-of-freedom motion measurement of linear nanopositioning stage using knife edge displacement sensing technique, Review of Scientific Instruments, Vol. 88, Iss. 6, 065110 (2017).

[21] ChaBum Lee, Seongkyul Jeon, Christopher K. Stepanick, Abolfazl Zolfaghari, and Joshua A. Tarbutton, Investigation of optical knife edge sensor for low cost, large-

range and dual-axis nanopositioning stages, Measurement, Vol. 103, pp. 157-164 (2017).

[22] A. Maghareh, C. E. Silva, and S. J. Dyke, "Servo-hydraulic actuator in controllable canonical form: Identification and experimental validation," Mechanical Systems and Signal Processing, vol. 100, pp. 398–414 (2018).

[23] E. Acome, S. K. Mitchell, T. G. Morrissey et al., "Hydraulically amplified self-healing electrostatic actuators with muscle-like performance," Science, vol. 359, no. 6371, pp. 61–65 (2018).

[24] J. Krause and P. Bhounsule, "A 3D printed linear pneumatic actuator for position, force and impedance control," Actuators, vol. 7, p. 24 (2018).

[25] Christian L. Nall 1 and Pranav A. Bhounsule, A Miniature 3D Printed On-Off Linear Pneumatic Actuator and Its Demonstration into a Cartoon Character of a Hopping Lamp, Actuator, Vol. 8, No. 72 (2019).

[26] Kawashima K., Fujita T., "Precise Position Stages Using Pneumatically Driven Bellows Actuator and Cylinder Equipped with Air Bearings", In: Higuchi T., Suzumori K., Tadokoro S. (eds) Next-Generation Actuators Leading Breakthroughs. Springer, London (2020).

[27] Kenji Kawashima, Takeshi Arai, Kotaro Tadano, Toshinori Fujita, and Toshiharu Kagawa, Development of coarse/fine dual stage using pneumatically driven bellow actuator and cylinder with air bearings, Precision Engineering, vol. 34, Iss. 3, pp. 526-533 (2010).

[28] Mao-Hsiung Chiang, Development of X-Y Servo Pneumatic-Piezoelectric Hybrid Actuators for Position Control with High Response, Large Stroke and Nanometer Accuracy, Sensors, vol. 4, No. 4, pp. 2675-2693 (2010).

[29] Chiang M.H., Chen C.C., Chow D.N. High precision pneumatic-piezoelectric hybrid positioning control using adaptive discrete variable structure control. Mechatronics. Vol. 15, pp. 523–545 (2005).

[30] Heebum Chun, Jaemin Han, Lesley Wright, Alaa Elwany, Herminso Villarraga-Gomez, and ChaBum Lee, Pressure-fed mechanism to compensate for motions and dynamic characteristics of compliant nanopositioning stages, Precision Engineering, 63, pp. 33-40 (2020).

[31] Jaemin Han, and ChaBum Lee, Dynamic and thermal characterization of additively manufactured pressure-fed flexures with internal fluidic channels, Smart Materials and Structures, 28, 105032 (2019).

[32] Heebum Chun, Gyu Ha Kim, Herminso Villarraga-Gomez, Hyo-Young Kim, Alaa Elwany and ChaBum Lee, Characterization of thermally stable compliant structures with internal fluidic channels, Precision Engineering, Vol. 66, pp. 201-208 (2020).

7. CONCLUSIONS

7.1. Conclusion

The research works presented in this thesis includes characterizing and investigating the novel FPFM for addressing current challenges and limitations in precision mechanical systems such as angular motion errors, limited bandwidth, vibrations, low thermal stability, resolution, and positioning performance. As a result, FPFM can correct up to 0.8 µrad angular (yaw) motion errors when 80 psi of pneumatic pressure is applied, and it can improve the thermal stability approximately 90% with flowing fluids into internal channels under certain flowrate and pressure when the nanopositioning stage is in operating. Moreover, the FPFM affects the dynamic characteristics of the flexure mechanism. Consequently, the damping of the dynamic system increased by 44%, which enables in-situ control of the damping parameters. Lastly, FPFM driven motion can provide sub-nanometer level motion that can be used for a monolithic FPFM dual-mode stage for precision applications along with increasing the system performance in bandwidth, resolution, thermal stability while reducing the motion error and vibrations. Therefore, FPFM can be applied in high performance engineered devices, and it is expected to meet the requirement for achieving high precision in a simple, low-cost, convenient, and effective way.

7.2. Future Works

The designed metal flexure mechanism for the characterization has high stiffness. However, if the FPFM is applied in a more compliant structure, the effect of FPFM is presumably significant for increasing the stability and operating speed of dynamic

systems. Furthermore, bidirectional FPFM driven fine motion using proportional pressure controllers with a solenoid valve is currently in the investigation stage. After investigating the FPFM driven motion, the monolithic FPFM dual-mode stage (FPFM for a fine motion and PZT for a coarse motion) will be developed by constructing an advanced control method for a switching mode dual-stage control.